2017

Data-Driven Adaptive Reynolds-Averaged Navier-Stokes k - ω Models for Turbulent Flow-Field Simulations

Zhiyong Li

University of Kentucky, beifang5560@gmail.com

Author ORCID Identifier:

https://orcid.org/0000-0003-4763-2139

Digital Object Identifier: https://doi.org/10.13023/ETD.2017.280

Click here to let us know how access to this document benefits you.

Recommended Citation

STUDENT AGREEMENT:

I represent that my thesis or dissertation and abstract are my original work. Proper attribution has been given to all outside sources. I understand that I am solely responsible for obtaining any needed copyright permissions. I have obtained needed written permission statement(s) from the owner(s) of each third-party copyrighted matter to be included in my work, allowing electronic distribution (if such use is not permitted by the fair use doctrine) which will be submitted to UKnowledge as Additional File.

I hereby grant to The University of Kentucky and its agents the irrevocable, non-exclusive, and royalty-free license to archive and make accessible my work in whole or in part in all forms of media, now or hereafter known. I agree that the document mentioned above may be made available immediately for worldwide access unless an embargo applies.

I retain all other ownership rights to the copyright of my work. I also retain the right to use in future works (such as articles or books) all or part of my work. I understand that I am free to register the copyright to my work.

REVIEW, APPROVAL AND ACCEPTANCE

The document mentioned above has been reviewed and accepted by the student's advisor, on behalf of the advisory committee, and by the Director of Graduate Studies (DGS), on behalf of the program; we verify that this is the final, approved version of the student's thesis including all changes required by the advisory committee. The undersigned agree to abide by the statements above.

Zhiyong Li, Student

Dr. Sean Bailey, Major Professor

Dr. Haluk Karaca, Director of Graduate Studies

Data-Driven Adaptive Reynolds-Averaged Navier-Stokes k-ω Models for Turbulent
Flow-Field Simulations

DISSERTATION

A dissertation submitted in partial
fulfillment of the requirements for
the degree of Doctor of Philosophy
in the College of Engineering at the
University of Kentucky

By
Zhiyong Li
Lexington, Kentucky

Co-Directors: Dr. Sean Bailey,   Professor of Mechanical Engineering
      and Dr. Jesse Hoagg,   Professor of Mechanical Engineering
      and Dr. Alexandre Martin,   Professor of Mechanical Engineering

Lexington, Kentucky 2017

ABSTRACT OF DISSERTATION

Data-Driven Adaptive Reynolds-Averaged Navier-Stokes k-ω Models for Turbulent Flow-Field Simulations

The data-driven adaptive algorithms are explored as a means of increasing the accuracy of Reynolds-averaged turbulence models. This dissertation presents two new data-driven adaptive computational models for simulating turbulent flow, where partial-but-incomplete measurement data is available. These models automatically adjust (i.e., adapts) the closure coefficients of the Reynolds-averaged Navier-Stokes (RANS) k-ω turbulence equations to improve agreement between the simulated flow and a set of prescribed measurement data.

The first approach is the data-driven adaptive RANS k-ω (D-DARK) model. It is validated with three canonical flow geometries: pipe flow, the backward-facing step, and flow around an airfoil. For all 3 test cases, the D-DARK model improves agreement with experimental data in comparison to the results from a non-adaptive RANS k-ω model that uses standard values of the closure coefficients.

The second approach is the Retrospective Cost Adaptation (RCA) k-ω model. The key enabling technology is that of retrospective cost adaptation, which was developed for real-time adaptive control technology, but is used in this work for data-driven model adaptation. The algorithm conducts an optimization, which seeks to minimize the surrogate performance, and by extension the real flow-field error. The advantage of the RCA approach over the D-DARK approach is that it is capable of adapting to unsteady measurements. The RCA-RANS k-ω model is verified with a statistically steady test case (pipe flow) as well as two unsteady test cases: vortex shedding from a surface-mounted cube and flow around a square cylinder. The RCA-RANS k-ω model effectively adapts to both averaged steady and unsteady measurement data.

KEYWORDS: RANS, turbulence, adaptive, data-driven, retrospective

Author's signature:_____ Zhiyong Li

Date:_____ July 19, 2017

Data-Driven Adaptive Reynolds-Averaged Navier-Stokes k-ω Models for Turbulent
Flow-Field Simulations

By
Zhiyong Li

<div style="text-align:right">

Sean Bailey
Co-Director of Dissertation

Jesse Hoagg
Co-Director of Dissertation

Alexandre Martin
Co-Director of Dissertation

Haluk Karaca
Director of Graduate Studies

July 19, 2017
Date

</div>

This dissertation is dedicated to the advancement of science.
I would also like to dedicate this work to my dear family.

ACKNOWLEDGMENTS

TABLE OF CONTENTS

LIST OF TABLES

LIST OF FIGURES

Nomenclature

A face area (m^2)

$C_{i,j}$ cross stress

D_k dissipation of k equation

D_ω dissipation of ω equation

E stagnation energy $(\mathrm{J/kg})$

$\boldsymbol{F}_{dn}$ diffusive flux at face-normal direction

$\boldsymbol{\mathcal{F}}$ matrix of convective term

$\boldsymbol{\mathcal{F}}_d$ matrix of diffusion term

G dimensionless velocity gradient

G_l l-direction term of gradient vector

G_m m-direction term of gradient vector

G_n n-direction term of gradient vector

G_x x-direction term of gradient vector

G_y y-direction term of gradient vector

G_z z-direction term of gradient vector

G_{st} dimensionless velocity gradient threshold of segmentation

H height of the step of backward facing step case

H_i impulse response coefficients at i points

I_t turbulent intensity

$\boldsymbol{I}$ identity matrix

J cost of simulation result

K projection of face area A along $\boldsymbol{l}_r$, divide by length of $\boldsymbol{l}_r$.

$L_{i,j}$ Leonard stress

$L(n)$ control matrix of RCA method at time step n

$\boldsymbol{M}$ coefficients matrix of diffusive flux

$M(n)$ control matrix of RCA method at time step n

N measured points number

$N(n)$ control matrix of RCA method at time step n

$\boldsymbol{P}$ primitive variables vector

$\boldsymbol{P}_L$ primitive variable vectors on left side of the face

$\boldsymbol{P}_R$ primitive variable vectors on right side of the face

P_k production of k equation

$P(n)$ control matrix of RCA method at time step n

P_ω production of ω equation

Pr Prandtl number

Pr_t turbulent Prandtl number, usually 0.9

$\triangle\boldsymbol{P}$ increments of primitive variables vector

$\boldsymbol{Q}$ conservative variables

$Q(n)$ control matrix of RCA method at time step n

R radius of the pipe

$\boldsymbol{R}$ Reynolds stress tensor

$\mathcal{R}$ right side term of discretization form equation

$\mathcal{R}$ ideal gas constant $(\frac{\mathrm{J}}{\mathrm{molK}})$

$\boldsymbol{R}_G$ rotation matrix

$\boldsymbol{R}_{xn}$ rotation matrix

$\boldsymbol{S}$ trace-less viscous strain-rate

$\widetilde{\boldsymbol{S}}_{11}, \cdots, \widetilde{\boldsymbol{S}}_{33}$ element of trace-less viscous strain-rate

$\boldsymbol{S}_v$ vector of source term

S_k source term of k equation

S_ω source term of ω equation

T temperature (K)

T_t total temperature (K)

U_x speed on x direction (m/s) at Chapter 4 and 5

U_y speed on y direction (m/s) at Chapter 4 and 5

U_z speed on z direction (m/s) at Chapter 4 and 5

U_m measured velocity

U_{ref} reference velocity

U_s simulated velocity

V volume of cell

$\boldsymbol{V}$ rotating $\boldsymbol{V}_n$ into the old coordinates

$\boldsymbol{V}_n$ property vector after rotating into face norm coordinate system

$\boldsymbol{V}_{nL}$ transport properties on left side of the face

$\boldsymbol{V}_{nR}$ transport properties on right side of the face

$\mathcal{W}_i$ weighting matrix of ith measurement

$a_f(t)$ Fourier coefficient

c_p specific heat capacity at constant pressure (J/k)

c_v specific heat capacity at constant volume (J/k)

d distance from points to the wall

e internal energy (J)

$f(n)$ feedback of a system at time step n

f_c Cutoff wave number

n_c positive integer

n_r number of how many impulse response

G_s filter kernel

$\triangle h$ wall roughness

h cube height and square length at chapter 5

h_a enthalpy

k turbulent kinetic energy (J/kg)

$\boldsymbol{l}$ tangential face vector

l_x, l_y, l_z elements of tangential face vector

$\boldsymbol{l}_r$ vector from left cell center to right cell center

$\boldsymbol{m}$ tangential face vector

$\dot{m}$ mass through face (kg)

m_x, m_y, m_z elements of tangential face vector

Δn normal distance

ν_{sgs} Eddy viscosity from subgrid scale dissipation

n iteration steps

n_x, n_y, n_z elements of normal vector of face

$\boldsymbol{n}$ normal vector of face

p pressure (Pa)

p_t total pressure (Pa)

p_{ref} reference pressure

$\boldsymbol{q}$ heat flux (J/kg)

$q(n)$ vectorize form of $Q(n)$

r distance from the point to the center of circle

τ_{sgs} Subgrid scale stress tensor

t time (s)

tr trace norm

$\boldsymbol{u}$ velocity vector (m/s)

$\boldsymbol{u}'$ fluctuate velocity vector (m/s)

$\bar{\boldsymbol{u}}$ Reynolds average mean velocity vector (m/s)

$\widetilde{\boldsymbol{u}}$ Resolved velocity vector (m/s) in Section 2.3; Favre-average velocity vector (m/s) outside Section 2.3

u speed on x direction (m/s) at Chapter 1,2 and 3

u_τ shear velocity

u_l $\boldsymbol{l}$ direction velocity under $(\boldsymbol{n}, \boldsymbol{l}, \boldsymbol{m})$ coordinates

u_m $\boldsymbol{m}$ direction velocity under $(\boldsymbol{n}, \boldsymbol{l}, \boldsymbol{m})$ coordinates

u_n $\boldsymbol{n}$ direction velocity under ($\boldsymbol{n}$,$\boldsymbol{l}$,$\boldsymbol{m}$) coordinates

v speed on y direction (m/s) at Chapter 1,2 and 3

w speed on z direction (m/s) at Chapter 1,2 and 3

w_i weight of ith measurement

w_{max} maximum weight

w_{min} minimum weight

$\boldsymbol{x}$ Cartesian coordinate (m)

x x direction coordinate (m)

Δy distance from point to wall

y y direction coordinate (m)

z z direction coordinate (m)

α coefficient in front of production of ω equation

β coefficient in front of dissipation of ω equation

β^* coefficient in front of dissipation of k equation

$\boldsymbol{\ell}$ turbulence length scale

$\boldsymbol{\tau}$ deviatoric stress tensor

$\boldsymbol{\Gamma(\theta)}$ approximate gradient of closure coefficients

$\boldsymbol{\phi_i(\theta_0)}$ initial simulation results at i point

$\boldsymbol{\phi_m}$ measured results at i point

$\boldsymbol{\theta}$ vector of closure coefficients for k-ω equation

$\delta\boldsymbol{\theta}$ increment of closure coefficients

ℓ selected characteristic length

ℓ_θ number of closure coefficients

ϵ_0 small value

ϵ_1 small number for convergence threshold

ϵ_2 small number for convergence threshold

η_n step size control parameter

γ ratio of specific heats

γ_n smallest nonnegative integer for step size

μ dynamic viscosity $(\text{Pa} \cdot \text{s})$

μ_t eddy viscosity

ν kinetic viscosity (m^2/s)

ν_t turbulence kinetic viscosity (m^2/s)

ω rate of dissipation of energy in unit volume and time

$\Omega(n)$ control matrix of RCA method at time step n

ω_{max} maximum bound of ω

$\phi_m(n)$ measured value at n steps

$\phi_s(n)$ simulated value at n steps

Ψ control matrix of RCA method

$\psi(n)$ control matrix of RCA method at time step n

ρ density (kg/m^3)

σ_ω coefficient of eddy viscosity of ω equation

σ_k coefficient of eddy viscosity of k equation

τ_w shear stress

ε dissipation of turbulent kinetic energy per unit mass

$\varphi_f(x)$ a complete (in L^2), orthogonal basis

ξ coefficient of numerical gradient method

ξ_n step size

$\xi_{*,n}$ maximum allowable step size

$\xi_{\text{opt},n}$ optimal step size

$\zeta'_\text{r}(n)$ modified retrospective performance of a system at time step n

$\zeta(n)$ performance of a system at time step n

$\zeta_\text{r}(n)$ retrospective performance of a system at time step n

k_R non-dimensional roughness

Chapter 1 Introduction

1.1 Overview of turbulence simulation

Turbulence, which remains one of the greatest unsolved problems in physics, is a natural phenomenon that appears within solutions of the Navier-Stokes equations, the governing equations of fluid motion. Although analytically investigated for centuries, the uniqueness of solutions in three dimensions has yet to be proven. Despite these mathematical curiosities, the Navier-Stokes equations have proven to be of immense practical use and numerical solutions, in the form of computational fluid dynamics (CFD), have allowed simulation of a wide range of fluid behavior, including turbulence.

The simulation of turbulence has progressed considerably over the last few decades with three approaches gaining prominence: direct numerical simulation (DNS), large eddy simulation (LES), and closure of the Reynolds-averaged Navier-Stokes (RANS) equations through phenomenological models. DNS has proven to provide accurate solutions but requires that the computational grid is resolved down to the Kolmogorov dissipation scale at which scale the linear viscous dissipation force overwhelms the nonlinear inertial force. At the other end of the spectrum, the simulations must also resolve the largest coherent structures within the turbulence, reflected in the integral scale. The ratio between these disparate scales is $\mathcal{O}(Re^{3/4})$ where Re is the Reynolds number which, for this problem, is formed from the integral scale, a velocity scale proportional to the square root of the kinetic energy of the turbulence, and the kinematic viscosity of the fluid. Three-dimensional DNS of turbulence therefore requires $\mathcal{O}(Re^{9/4})$ grid points to resolve from the integral scale down to the Kolmogorov scale. In addition, for time accurate simulation cases, the time step size should be small

enough for the Courant-Friedrichs-Lewy (CFL) condition to be smaller than or equal to 1. Thus, the time step size is proportional to the grid size. Thus, a critical drawback of DNS is the computational cost, as it is still intractable for many practical flows of interest, where $Re > \mathcal{O}(10^5)$. Hence, DNS for high Re is beyond the capability of even the most advanced supercomputers.

In contrast to DNS, LES and RANS do not try to resolve all details of the turbulence but instead use mathematical models to incorporate the effects of turbulence on the large-scale flow features. LES filters the high-frequency and high-wave-number fluctuations and replaces them with a closure model to incorporate the effect of dissipated kinetic energy from the subgrid scale motions. LES requires modeling part of the inertial subrange and into the beginning of the dissipation scales, and the total number of flops is a function of Re^2. Although LES is higher fidelity than RANS approach, the computational cost of LES is still high when compared to RANS.

RANS models the influence of the turbulent fluctuations on the mean flow. This is done through the Reynolds-averaging procedure, which introduces additional unknowns into the equations of motion, creating what is referred to as the *'closure problem'*. Thus, closure models are introduced to capture the impact of the turbulent fluctuations on the mean flow, which is reflected through the so-called *Reynolds stress*. The closure models include non-universal coefficients referred to as *'closure coefficients'*, and modelers often have to calibrate these closure coefficients using either known solutions to the Navier-Stokes equations or empirical results. The impact of the closure coefficients is a reduction in accuracy of the simulations. However, because RANS requires fewer computational resources, It is commonly used to solve applied problems.

1.2 Motivation of the present work

Turbulence commonly appears in transport systems, ranging from the flow through pipes to jet engines and vehicle aerodynamics. One turbulent flow which can impact public safety is through the role of turbulence in the transport of the chemical, biological, radiological, or nuclear material generated by modern industries. For example, thousands of lives could be threatened, in the event of an unplanned leakage, which could appear in the form of toxic smoke from a warehouse fire or gaseous chemicals released during a transportation accident. The ability to forecast or predict the dispersion of toxic gases in order to provide safe evacuation routes is important for disaster mitigation. In these instances, dispersion of these toxic gases from the Earth's surface to the atmosphere is driven by the turbulence within the atmospheric boundary layer. Useful forecasting of this dispersion must be accurate, but obtaining accurate forecasts is hampered by the rapid change in turbulent behavior which can arise due to changing meteorological conditions, or due to the complex influences of terrain topology.

Using measurements to produce a sufficiently detailed flow map for predicting toxic material dispersion in turbulence is challenging due to the multi-scale nature of turbulence. It would require a prohibitively dense spatial resolution of sensors. Dispersion predictions based on empirical correlations and limited measurements are possible. However, these correlation approaches become increasingly inaccurate as the complexity of the surroundings increase. A numerical simulation could provide more details, but obtaining accurate simulations requires knowledge of appropriate turbulence model coefficients and boundary conditions, which in an evolving atmospheric turbulent flow over complex terrain can be a significant hurdle.

Therefore there is a potential benefit in adapting computational flow-field simulations to match limited measurement information in order to provide a real-time flow-field estimation for predicting airborne pollutant dispersion. By adapting com-

putational simulations to match limited measurements, the simulations become more accurate, and their detail provides improved prediction of the dispersion of a toxic plume: its direction, how fast it will go, how large of a range it will cover, what the concentrations are, and whether it will threaten people's health.

A long-term objective of this research is to develop a flow-field estimation method, which utilizes turbulence measurements to novel update an adaptive computational flow-field model. The proposed data-driven adaptive RANS model is shown schematically in Fig. 1.1. In this model, flow-field measurements are used to update the boundary conditions and closure coefficients used by the RANS model. There are two primary parts in this flow-field estimation system, namely, a cyber system and a physical system. The physical system is the flow field of interest where some measurements are made [6, 7, 8, 9]. The cyber system consists of a computational turbulence model, and a data-driven model aptation algorithm.
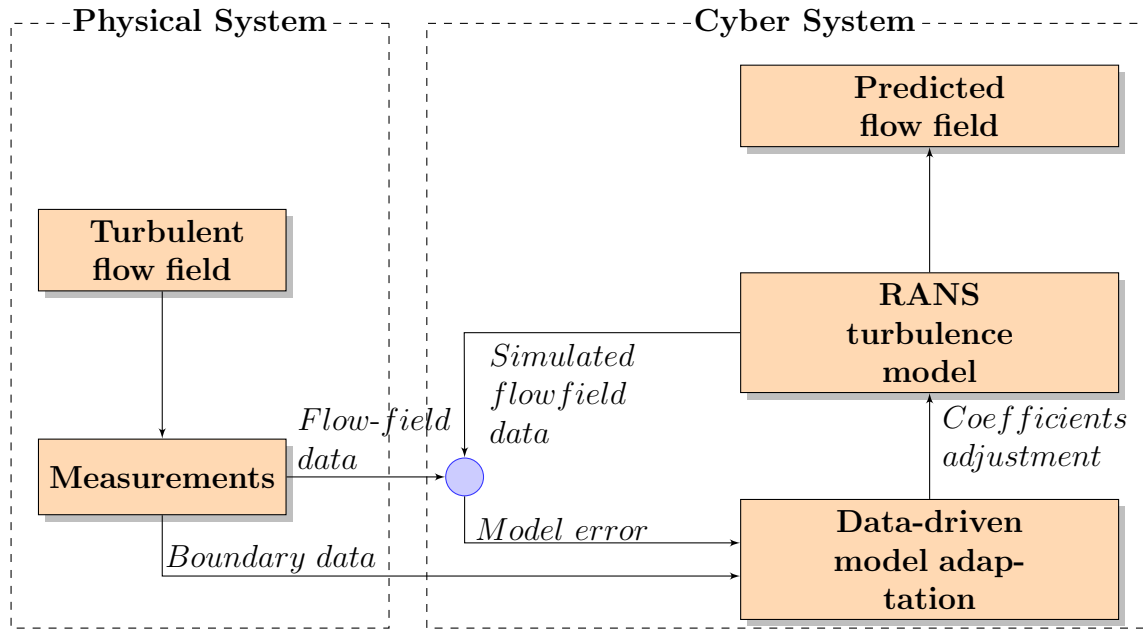
Figure 1.1: Prediction of turbulent flow field using simulation and measurements.

This dissertation provides a first step in producing such a cyber system by developing and implementing two different model adaptation approaches within a numer-

ical simulation. As the objective is to eventually achieve near real-time simulations, these adaptation approaches are implemented using RANS k-ω turbulence model. However, the data-driven model adaptation approaches in this dissertation used in conjunction with other RANS models provided that the model has parameters that need to be tuned. The data-driven model adaptation algorithms automatically adjust or *adapts* model parameters, specifically here the k-ω closure coefficients, to improve agreement between the simulated flow field and measured data, which are at spatially separated locations in the flow field.

The first approach developed is termed the data-driven adaptive RANS k-ω (D-DARK) and is implemented in combination within a compressible CFD solver. The second approach is called a retrospective cost adaptive RANS (RCA-RANS) k-ω approach and is implemented in combination with an incompressible CFD solver. For both approaches verification and validation results are presented using several canonical flow-field geometries. The validation results demonstrate that the adaptation improves agreement with experimental data, at least in comparison to the results from a non-adaptive RANS k-ω model using the standard values of the k-ω closure coefficients [10].

Chapter 2 presents mathematical fundamentals for turbulence modelling. Chapter 3 describes the CFD solvers being used for the simulations. Chapter 4 presents and validates the D-DARK approach with the RCA-RANS k-ω approach presented and validated in Chapter 5. The final summary, conclusions, and future work are provided in Chapter 6.

Original contributions The primary original contributions of this dissertation are the D-DARK model in Chapter 4 and the RCA-RANS k-ω model in Chapter 5.

Chapter 4 presents a new data-driven adaptive computational model for simulating turbulent flow, where partial-but-incomplete measurement data is available. The model automatically adjusts the closure coefficients of the Reynolds-averaged Navier-

Stokes (RANS) k-ω turbulence equations to improve agreement between the simulated flow and the measurements. This data-driven adaptive RANS k-ω (D-DARK) model is validated with three canonical flow geometries: pipe flow, backward-facing step, and flow around an airfoil. For all test cases, the D-DARK model improves agreement with experimental data in comparison to the results from a non-adaptive RANS k-ω model that uses standard values of the closure coefficients. For the pipe flow, adaptation is driven by mean stream-wise velocity data from 42 measurement locations along the pipe radius, and the D-DARK model reduces the average error from 5.2% to 1.1%. For the 2-dimensional backward-facing step, adaptation is driven by mean stream-wise velocity data from 100 measurement locations at four cross-sections of the flow. In this case, D-DARK reduces the average error from 40% to 12%. For the NACA 0012 airfoil, adaptation is driven by surface-pressure data at 25 measurement locations. The D-DARK model reduces the average error in surface-pressure coefficients from 45% to 12%.

In Chapter 5, A real-time adaptive control technology, called retrospective cost adaptation (RCA), is applied to automatically adjust the closure coefficients of the unsteady Reynolds-averaged Navier-Stokes (URANS) k-ω turbulence equations. RCA approach has been successfully validated on numerous control applications that have significant transient behavior, which suggests that RCA is well suited for adaptation with unsteady flows. The RCA-URANS k-ω model is verified by a statistically steady test case (pipe flow) as well as two unsteady test cases: vortex shedding from a surface-mounted cube and flow around a square cylinder. The results of all cases demonstrate that the k-ω closure coefficients can be updated to match the measurement data. Specifically, the periodicity in the simulated unsteady flow is in good agreement with the phase-averaged experimental data. It is therefore concluded that the RCA-URANS k-ω model is able to improve the original k-ω model results by adapting to measurement data for both averaged steady and unsteady turbulent flows.

Chapter 2 Theoretical Fundamentals of Turbulence Modelling

In this chapter, the governing equations for the fluid motion are introduced. These include the mass, momentum, and energy conservation equation for both compressible and incompressible flow conditions. RANS, LES, and DNS approaches to solve these governing equations are also reviewed along with a description of the RANS k-ω model, which is used throughout this dissertation.

2.1 Governing equations

Except in very few situations, such as the atmosphere at very high altitude, fluid obeys the continuum hypothesis, and we assume that it is a continuous field of fluid properties and treat its behavior at the molecular scale in an average sense. In addition, most fluids can also be treated as Newtonian, and we can assume that there is a linear relationship between stress and rate of strain. Finally, it is common practice to discriminate between compressible flow, where density is a variable and treated as an unknown, and incompressible flow, where density is a known constant, and pressure is treated as the unknown.

The governing equations of the fluid motion are formed from the requirement that they conserve mass, obey a momentum balance, and conserve energy. The partial differential equations governing transport for compressible Newtonian flow are

$$\frac{\partial \rho}{\partial t} + \nabla \cdot (\rho \boldsymbol{u}) = 0, \tag{2.1}$$

$$\frac{\partial (\rho \boldsymbol{u})}{\partial t} + \nabla \cdot (\rho \boldsymbol{u}\boldsymbol{u}) = -\nabla p + \nabla \cdot \boldsymbol{\tau}, \tag{2.2}$$

$$\frac{\partial (\rho E)}{\partial t} + \nabla \cdot (\rho E \boldsymbol{u}) = -\nabla \cdot (p\boldsymbol{u}) + \nabla \cdot (\boldsymbol{u} \cdot \boldsymbol{\tau}) - \nabla \cdot \boldsymbol{q}, \tag{2.3}$$

where Eq. (2.1) is conservation of mass, and Eqs. (2.2) and (2.3) are the momentum balance and conservation of energy. Note that body forces (e.g., gravity) have been neglected but can easily be included. The symbol $\cdot$ indicates an inner product, and $\boldsymbol{uu}$ is an outer product. Vectors and tensors are indicated in bold, with tensors generally denoted using capital letters or Greek symbols, although this convention is used loosely.

The vector $\boldsymbol{x}$ indicates the position in Cartesian coordinates. In addition, t is time, $\boldsymbol{u}(\boldsymbol{x}, t)$ is the velocity vector, $p(\boldsymbol{x}, t) \in \mathbb{R}$ is the pressure, $\boldsymbol{q}(\boldsymbol{x}, t)$ is the heat flux vector, and $\boldsymbol{\tau}(\boldsymbol{x}, t)$ is deviatoric stress tensor. For Newtonian fluids, the deviatoric stress tensor is given by

$$\boldsymbol{\tau} \triangleq 2\mu \boldsymbol{S}, \tag{2.4}$$

where $\mu(\boldsymbol{x}, t) \in \mathbb{R}$ is the dynamic viscosity, and $\boldsymbol{S}(\boldsymbol{x}, t)$ is the rate of the strain tensor, which is given by

$$\boldsymbol{S} \triangleq -\frac{1}{3}(\nabla \cdot \boldsymbol{u})\boldsymbol{I} + \frac{1}{2}(\nabla \boldsymbol{u} + (\nabla \boldsymbol{u})^{\mathrm{T}}). \tag{2.5}$$

The superscript T indicates the transpose operator, and $\boldsymbol{I}$ is the identity tensor. The stagnation energy per unit mass is $E(\boldsymbol{x}, t) \in \mathbb{R}$, which is

$$E = e + \frac{1}{2}\boldsymbol{u} \cdot \boldsymbol{u}, \tag{2.6}$$

where $e(\boldsymbol{x}, t) \in \mathbb{R}$ is the internal energy per unit mass.

For gaseous flow at very low speed or liquid flows having low compressibility, density is nearly constant and can be treated as being incompressible. The governing equations used to describe the incompressible flow are different from those used for compressible fluids. For incompressible flow without a body force applied, the energy conservation equation (2.3) is not necessary. The time term derivative $\partial e / \partial t$ of the mass conservation equation (2.1) is equal to zero, and the mass conservation equation is simplified to the divergence-free equation. The governing equations without body

forces for viscous incompressible flow are

$$\nabla \cdot \boldsymbol{u} = 0, \tag{2.7}$$

$$\frac{\partial \boldsymbol{u}}{\partial t} + \nabla \cdot (\boldsymbol{u}\boldsymbol{u}) = \frac{1}{\rho}(-\nabla p + \nabla \cdot \boldsymbol{\tau}). \tag{2.8}$$

For incompressible flow, since there is the divergence-free condition, the rate of the strain tensor is

$$\boldsymbol{S} \triangleq \frac{1}{2}(\nabla \boldsymbol{u} + (\nabla \boldsymbol{u})^{\mathrm{T}}). \tag{2.9}$$

2.2 Turbulence and its length scales

Simulation of turbulent flows remains an important problem in modern fluid dynamics. The Navier-Stokes equations are nonlinear partial differential equations with the Reynolds number (Re) as the bifurcation parameter. The Reynolds number is the ratio of inertial force to viscous force, and if it is small (i.e., $Re << 1$), then the Navier-Stokes equations display linear behavior because the nonlinear advective term becomes small relative to the viscous terms. At slightly higher Re, inertial forces become increasingly important, but there is still sufficient viscosity to damp out nonlinear instabilities of the governing equations. For even larger Re, inertial forces exceed the viscous forces and dominate fluid motion, producing chaotic behavior and instabilities. This chaotic behavior appearing through the formation of short-lived coherent motions within the fluid is commonly referred to as eddies. These eddies lack formal definition, but turbulence follows a cascade process where larger eddies break into successively smaller eddies, decreasing in length scale and kinetic energy as they do so. When eddies reach sufficiently small scale, their inertia is unable to overcome the stabilizing effect of viscosity, and their kinetic energy dissipates into internal energy. Note that this description of the cascade process is not wholly accurate. For example, it has been demonstrated that there also exists backscatter of energy from small eddies towards the larger eddies [11]. Regardless, nonlinearities

9

and chaotic behaviors cause the simulation of turbulence to be more challenging than laminar flow.

From observation, we know the turbulence is a multi-scale flow [12]. In general, there are four main scales, which are used to describe turbulence:

1. the largest scales, sometimes described as permanent eddies, typically on the order of the domain;

2. the large energy containing motions, often described through the integral-length scale or ℓ, typically on the order of the largest geometrical features in the domain;

3. the Taylor micro-scale, which is an intermediate scale, that has been connected to the largest dimension of the dissipative eddies;

4. the Kolmogorov scale, which describes the smallest dynamically important eddies, and describes the scale of motions at which kinetic energy dissipates to internal energy.

Thus, to accurately simulate turbulent flow, a simulation must resolve from the largest scales to the smallest scales at a temporal resolution capable of fully capturing their chaotic evolution. This is the approach taken in direct numerical simulation (DNS) which, as a result, requires very fine computational grids that are resolved down to the Kolmogorov dissipation scale. If we use a Reynolds number defined by the integral scale and the typical velocity of the turbulent motions, then the ratio of the Kolmogorov scale to the integral scale is $\mathcal{O}(Re^{3/4})$. Thus, a three-dimensional grid resolving all turbulent scales requires as many as $\mathcal{O}(Re^{9/4})$ grid points. The computational costs associated with this resolution causes DNS to be impractical for the Re associated with most engineering flows. Being a balance between fidelity and efficiency, large-eddy simulation is, therefore, a valuable approach.

2.3 Large-eddy simulation

Large eddy simulation (LES) is still a focus of development [13, 14, 15]. In particular, several new models have recently been proposed to introduce spatial and time dependence into the model coefficients. These developments include the dynamic Smagrinsky model [16, 17], and mixed models [18]. Other LES subgrid-scale models include Deardorff's model [19] and Vreman's model [20]. However, it was Smagorinsky [21] who was the first to propose LES in 1963 with Deardorff [22] advancing it further in 1970.

$$\boldsymbol{u}(\boldsymbol{x},t) = \widetilde{\boldsymbol{u}}(\boldsymbol{x},t) + \boldsymbol{u}'(\boldsymbol{x},t) \ , \tag{2.10}$$

where $\boldsymbol{u}(\boldsymbol{x},t) \in L^2(\Omega) \times C^1(0,t_f)$, $\boldsymbol{u}'(\boldsymbol{x},t)$ is called the subgrid-scale part, and $\widetilde{\boldsymbol{u}}$ is the large-scale, or resolved, part. Symbol $\widetilde{\ }$ means the large scale of the original variable after filtering. The large scale part is defined as

$$\widetilde{\boldsymbol{u}}(\boldsymbol{x},t) \triangleq \int_{\Omega_i} G_s(\boldsymbol{x}|\xi)\boldsymbol{u}(\xi,t)d\xi \ , \tag{2.11}$$

where $G_s(\boldsymbol{x}|\xi)$ is the filter kernel [23]. Common filters include Gaussian or Pade filters. The filter width is chosen to be a few multiples of the discretized length; Ω_i is a subdomain of the solution domain Ω.

The LES decomposition can also be represented in the Hilbert space by Fourier representation,

$$\boldsymbol{u}(x,t) = \sum_{\substack{f_c \\ |f|>0}} a_f(t)\varphi_f(x) + \sum_{\substack{\infty \\ |f|=f_c+1}} a_f(t)\varphi_f(x) \ , \tag{2.12}$$

where, f_c is the cutoff wavenumber caused by discretization of the governing equations, $a_f(t)$ is the Fourier coefficient, and $\varphi_f(x)$ is being a complete (in L^2), orthogonal basis. This demonstrates the reason high-wavenumber parts of the solution need to be modeled. LES modeling of the high wavenumber range relies on Kolmogorov's universal equilibrium theory, which assumes that the high wavenumber component of tur-

bulence obeys universal behavior and can be divided into an inertial subrange, where viscosity is unimportant, and the dissipation range described by the Kolmogorov scale where viscosity is transferring kinetic energy to internal energy. Typically LES models are designed to model wavenumbers above an f_c in the inertial subrange. The computations of LES is around $\mathcal{O}(Re^2)$ and it is thus more efficient than DNS, which requires directly resolving close to the Kolmogorov scale and requires computations of $\mathcal{O}(Re^3)$.

If (2.10) is substituted into the governing equation and the properties $\widetilde{\widetilde{\boldsymbol{u}}} \neq \widetilde{\boldsymbol{u}}$ and $\widetilde{\boldsymbol{u}'} \neq 0$ are applied, then we obtain the classical and well-known LES form

$$\nabla \cdot \widetilde{\boldsymbol{u}} = 0 \ , \tag{2.13a}$$

$$\widetilde{\boldsymbol{u}}_t + \nabla \cdot (\widetilde{\boldsymbol{u}}\widetilde{\boldsymbol{u}}) = -\nabla \widetilde{p} + \nu \Delta \widetilde{\boldsymbol{u}} - \nabla \cdot \boldsymbol{\tau}_{sgs} \ , \tag{2.13b}$$

with

$$\boldsymbol{\tau}_{sgs} = \widetilde{\boldsymbol{u}\boldsymbol{u}} - \widetilde{\boldsymbol{u}}\widetilde{\boldsymbol{u}} = L_{i,j} + C_{i,j} + R_{i,j} \ , \tag{2.14}$$

$$L_{i,j} \triangleq \widetilde{\widetilde{\boldsymbol{u}}_i \widetilde{\boldsymbol{u}}_j} - \boldsymbol{u}_i \boldsymbol{u}_j, \qquad C_{i,j} \triangleq \widetilde{\widetilde{\boldsymbol{u}}_i \boldsymbol{u}'_j} + \widetilde{\widetilde{\boldsymbol{u}}_j \boldsymbol{u}'_i}, \qquad R_{i,j} \triangleq \widetilde{\boldsymbol{u}'_i \boldsymbol{u}'_j} \ , \tag{2.15}$$

where $L_{i,j}$ is the Leonard stress, $C_{i,j}$ is the cross stress, $R_{i,j}$ is the Reynolds stress. The subgrid-stress (SGS) is a Galilean invariant with the sum of $L_{i,j}$ or $C_{i,j}$ is a Galilean invariant, although neither $L_{i,j}$ or $C_{i,j}$ is a Galilean invariant. If $\boldsymbol{\tau}_{sgs} \to 0$ as $h \to 0$ (or $f_c \to \infty$), it is clear that (2.13) converges to the Navier-Stokes equations and LES is equivalent to DNS. Actually, the term τ_{sgs} is similar to the artificial dissipation widely employed for shock capturing in compressible flow simulations.

The traditional way of modeling the subgrid-scale stress τ_{sgs} falls into three categories [24]: eddy-viscosity models, similarity models, and so-called mixed models. Eddy-viscosity models are based on the Boussinesq hypothesis, which is also extensively applied in RANS models, and is given

$$\boldsymbol{\tau}_{sgs} = -2\nu_{sgs}\widetilde{\boldsymbol{S}} \ , \tag{2.16}$$

where $\widetilde{\boldsymbol{S}}$ is the large-scale strain-rate tensor; ν_{sgs} is an eddy viscosity; and $\boldsymbol{\tau}_{sgs}$ is the subgrid-scale stress tensor. In the eddy-viscosity category, the Smagorinsky model [21] is the most widely used model. The eddy viscosity is constructed from the multiplication of the filter width, "Smagorinsky" constant and $\widetilde{\boldsymbol{S}}$, which is analogous to the mixing length formulation of the earliest turbulence modeling approaches. The Smagorinsky model and its various forms can estimate small-scale dissipation and perform well for flow far from solid boundaries. However, the problem is that this kind of model only accounts for the energy transferring from large scales to small scales; the phenomena of "backscatter" of energy from small to large scales is not considered. There are models that consider backscatter, such as the dynamical model [25] derived from the Germano identity [26]. However, the negative viscosities make the governing equation mathematically ill-posed, and they allow aliasing to supply the backscatter. It is worth noting that eddy-viscosity LES models are widely used in some commercial software [27].

Similarity models calculate backscatter in a more natural way [28, 29]. The scale similarity method treats the behavior of the lowest wavenumbers of the unresolved part similar to that of the highest wavenumbers of the resolved part. It approximates the subgrid-scale stress tensor with the stress tensor obtained from the resolved field by filtering the originally resolved field with the filter width equal to or larger than discretization length. However, the characteristic length scales do not match with the exact subgrid stress fields. Also, the subgrid stress dissipation is under-estimated by the model of Bardina et al. [28], which leads to its unreliability of simulating mean and root-mean-squared quantities of the turbulent flow field.

Mixed models [30] combine eddy viscosity and similarity expressions. In this case, the hope is to achieve the good dissipative features of eddy-viscosity models and the good predictive capabilities of similarity models for correlations. However, the accuracy is not highly improved, and the dependence of the models on a filter introduces

an additional complication. Hence, mixed models are not widely accepted [11].

In addition to the more traditional methods mentioned above, additional approaches to LES have also been developed. For example, the "implicit" LES approach proposed by Fureby and Grinstein [31]. It directly solves the governing equation and introduces numerical dissipation to replace physical dissipation. In this method, the filter is the computational grid together with the low-pass characteristics of the discrete difference operators. Another alternative approach to LES was proposed by Stolz and Adams [32]. This approximate deconvolution model approximates a non-filtered field through a truncated series expansion of the inverse-filter operator. Deconvolution has been found to be more stable than the scale-similarity method. Other approaches directly estimate the subgrid-scale variables [33, 34], such as the linear-eddy models and one-dimensional turbulence models [35, 36]. The linear eddy model combines a one-dimensional heat equation with a stochastic mixing process to simulates the subgrid-scale dissipation. It estimates both dissipation and nonlinear interactions and is a kind of synthetic-velocity model which has improved numerical stability due to its dissipation. Other models that estimate the subgrid-scale fluctuation directly are [37, 38], and these can produce good results. Structure models evaluate eddy viscosity or subgrid-scale stress directly according to flow structures, such as through deconvolution methods and synthetic velocity methods [39, 40, 41]. Zeng, et al. [42, 43] developed a low-order subgrid-scale model for modeling turbulent combustion in the context of LES, which improved computational efficiency, however, it also decreased solution accuracy at a center extent since the low-order model was implemented.

2.4   Favre- and Reynolds-averaged equations for turbulent flows

The earliest, and most computationally efficient, approaches to simulations are usually based on Reynolds averaging for incompressible flows, or Favre averaging for

compressible flows. Compared with LES and DNS, the Reynolds-Averaged Navier-Stokes (RANS) method, which is based on Reynolds decomposition, is widely used in the simulation of turbulence in industrial problems. As RANS approaches rely heavily on modeling the impact of turbulence on the mean flow, rather than resolving the turbulence directly, it is much less computationally expensive than DNS and LES.

2.4.1 Favre- and Reynolds-averaging

A formal approach to the statistical analysis of turbulence was first developed by Osborne Reynolds in 1894 [44] and is thus referred to as Reynolds decomposition and Reynolds averaging. Reynolds' work subsequently led to some of the earliest attempts at turbulence modeling in the form of the Boussinesq hypothesis and Prandtl's mixing length theory [45, 46]. For compressible flow, this approach was extended in a process referred to as Favre decomposition and averaging. To review these processes, we let $f : \mathbb{R}^3 \times [0, \infty) \to \mathbb{R}^n$ be a fluid property exhibiting turbulent behavior.

The time average of the turbulent variables is given as

$$\overline{f}(\boldsymbol{x}) \triangleq \frac{1}{t_0} \int_0^{t_0} f(\boldsymbol{x}, t) dt. \tag{2.17}$$

Note that $\overline{f}(\boldsymbol{x})$ is independent of time. Next, $f'(\boldsymbol{x}, t)$ is defined as

$$f'(\boldsymbol{x}, t) \triangleq f(\boldsymbol{x}, t) - \overline{f}(\boldsymbol{x}), \tag{2.18}$$

and note that $f(\boldsymbol{x}, t) = \overline{f}(\boldsymbol{x}) + f'(\boldsymbol{x}, t)$ is referred to as the Reynolds decomposition of $f(\boldsymbol{x}, t)$, where $\overline{f}(\boldsymbol{x})$ and $f'(\boldsymbol{x}, t)$ represent the time-averaged and time-varying components of f, respectively.

In compressible flow, the Reynolds average of some variables, such as momentum, is related to fluctuations in density as well. Let $\rho : \mathbb{R}^3 \times [0, \infty) \to \mathbb{R}^n$ be density, and define the density-weighted small-scale time-averaged value of f by

$$\widetilde{f}(\boldsymbol{x}) \triangleq \frac{\overline{\rho(\boldsymbol{x}, t) f(\boldsymbol{x}, t)}}{\overline{\rho}(\boldsymbol{x})}. \tag{2.19}$$

From this point forward, the symbol ~ will be used to represent the density-weighted time average, rather than the large-scale part of LES decomposition as used previously. Next, $f''(\boldsymbol{x}, t)$ is defined as

$$f''(\boldsymbol{x}, t) \triangleq f(\boldsymbol{x}, t) - \widetilde{f}(\boldsymbol{x}), \tag{2.20}$$

and note that $\widetilde{f}(\boldsymbol{x}) + f''(\boldsymbol{x}, t)$ is the Favre decomposition of $f(\boldsymbol{x}, t)$, where $\widetilde{f}(\boldsymbol{x})$ and $f''(\boldsymbol{x}, t)$ represent the density-weighted time-averaged and time-varying components of f, respectively. Note that the following identities are given in [47]

$$\overline{\rho \widetilde{f}} = \overline{\rho} \widetilde{f} = \overline{\rho f}, \tag{2.21}$$

$$\overline{f} = \widetilde{f} + \overline{f''} = \overline{\widetilde{f}} + \overline{f''}, \tag{2.22}$$

$$\overline{f''} = f'' - f', \tag{2.23}$$

$$\overline{\rho f''} = \overline{\rho} \widetilde{f''} = 0, \tag{2.24}$$

$$\overline{f'} = \widetilde{f''} = 0, \tag{2.25}$$

$$\overline{f''} = -\frac{\overline{\rho' f'}}{\overline{\rho}} = -\frac{\overline{\rho' f''}}{\overline{\rho}} = -\widetilde{f'}. \tag{2.26}$$

However, $\widetilde{f'}$ and $\overline{f''}$ are not necessarily zero. In the compressible case, mean streamlines are tangent to density weighted average velocity vector, but not to the Reynolds-averaged velocity vector [48].

2.5 Favre- and Reynolds-averaged governing equations

To use these concepts to develop governing equations for turbulent flow, the Reynolds- and Favre-averaging processes are applied to the Navier-Stokes equations.

2.5.1 Favre-averaged governing equations for compressible flow

Starting first with the more general case of compressible fluid flow, and taking the density-weighted time-average of the mass conservation equation (2.1) and using $\rho =$

$\bar{\rho} + \rho''$ yields

$$\overline{\frac{\partial \bar{\rho}}{\partial t}} + \overline{\frac{\partial \rho''}{\partial t}} + \nabla \cdot (\overline{\rho \boldsymbol{u}}) = 0, \tag{2.27}$$

where the derivative of time-average density is zero. The time-varying component of the primitive variables fluctuates around the average value. Thus, the density-weighted average and the time derivative are commutative. Using identities Eqs. (2.21) and (2.25) yields

$$\nabla \cdot (\overline{\rho} \widetilde{\boldsymbol{u}}) = 0. \tag{2.28}$$

Taking the density-weighted average of momentum and energy equation and using identities Eq. (2.21) and (2.25), it can be shown that the time terms of momentum and energy equation are equal to zero. Thus, the momentum equation (2.2) yields, on a term-by-term basis,

$$\nabla \cdot (\overline{\rho \boldsymbol{u} \boldsymbol{u}}) = -\nabla \bar{p} + \nabla \cdot \overline{\boldsymbol{\tau}}. \tag{2.29}$$

Using $\boldsymbol{u} = \widetilde{\boldsymbol{u}} + \boldsymbol{u}''$, Eqs. (2.21) and (2.25) yields

$$\nabla \cdot (\overline{\rho \boldsymbol{u} \boldsymbol{u}}) = \nabla \cdot (\overline{\rho(\widetilde{\boldsymbol{u}} + \boldsymbol{u}'')(\widetilde{\boldsymbol{u}} + \boldsymbol{u}'')}) \tag{2.30}$$

$$= \nabla \cdot (\overline{\rho \widetilde{\boldsymbol{u}} \widetilde{\boldsymbol{u}} + 2\rho \widetilde{\boldsymbol{u}} \boldsymbol{u}'' + \rho \boldsymbol{u}'' \boldsymbol{u}''}) \tag{2.31}$$

$$= \nabla \cdot (\overline{\rho \widetilde{\boldsymbol{u}} \widetilde{\boldsymbol{u}}}) + 2\nabla \cdot (\overline{\rho \widetilde{\boldsymbol{u}} \boldsymbol{u}''}) + \nabla \cdot (\overline{\rho \boldsymbol{u}'' \boldsymbol{u}''}) \tag{2.32}$$

$$= \nabla \cdot (\overline{\rho \widetilde{\boldsymbol{u}} \widetilde{\boldsymbol{u}}}) + 2\nabla \cdot (\overline{\rho \widetilde{\boldsymbol{u}} \boldsymbol{u}''}) + \nabla \cdot (\overline{\rho \boldsymbol{u}'' \boldsymbol{u}''}) \tag{2.33}$$

$$= \nabla \cdot (\overline{\rho} \widetilde{\widetilde{\boldsymbol{u}} \widetilde{\boldsymbol{u}}}) + 2\nabla \cdot (\overline{\rho} \widetilde{\widetilde{\boldsymbol{u}} \boldsymbol{u}''}) + \nabla \cdot (\overline{\rho} \widetilde{\boldsymbol{u}'' \boldsymbol{u}''}) \tag{2.34}$$

$$= \nabla \cdot (\overline{\rho} \widetilde{\boldsymbol{u}} \widetilde{\boldsymbol{u}}) + 2\nabla \cdot (\overline{\rho} \widetilde{\boldsymbol{u}} \widetilde{\boldsymbol{u}''}) + \nabla \cdot (\overline{\rho} \widetilde{\boldsymbol{u}'' \boldsymbol{u}''}) \tag{2.35}$$

$$= \nabla \cdot (\overline{\rho} \widetilde{\boldsymbol{u}} \widetilde{\boldsymbol{u}}) - \nabla \cdot \boldsymbol{R}, \tag{2.36}$$

where $\boldsymbol{R}(\boldsymbol{x})$ is the Reynolds stress tensor, which is given by

$$\boldsymbol{R} \triangleq -\overline{\rho} \widetilde{\boldsymbol{u}'' \boldsymbol{u}''}. \tag{2.37}$$

Through substitution of Eq. (2.36) into Eq. (2.29), Eq. (2.29) can be rewritten as

$$\nabla \cdot (\overline{\rho} \widetilde{\boldsymbol{u}} \widetilde{\boldsymbol{u}}) = -\nabla \bar{p} + \nabla \cdot (\overline{\boldsymbol{\tau}} + \boldsymbol{R}). \tag{2.38}$$

17

By applying the density-weighted average, the energy equation (2.3) becomes

$$\nabla \cdot (\overline{\rho E \boldsymbol{u}}) = -\nabla \cdot (\overline{p \boldsymbol{u}}) + \nabla \cdot (\overline{\boldsymbol{u} \cdot \boldsymbol{\tau}}) - \nabla \cdot \overline{\boldsymbol{q}}, \tag{2.39}$$

Substituting $p = \widetilde{p} + p''$ and $\boldsymbol{u} = \widetilde{\boldsymbol{u}} + \boldsymbol{u}''$ into $\overline{\rho E \boldsymbol{u}} + \overline{p \boldsymbol{u}}$, and using Eq. (2.21) yields

$$\overline{\rho E \boldsymbol{u}} + \overline{p \boldsymbol{u}} = \overline{\rho E \boldsymbol{u}} + \overline{p \boldsymbol{u}} \tag{2.40}$$

$$= \overline{\rho}(\widetilde{\widetilde{E} + E''})(\widetilde{\boldsymbol{u}} + \boldsymbol{u}'') + \overline{(\widetilde{\boldsymbol{u}} + \boldsymbol{u}'')p} \tag{2.41}$$

$$= \overline{\rho}(\widetilde{\widetilde{E}\widetilde{\boldsymbol{u}} + \widetilde{E}\boldsymbol{u}'' + E''\widetilde{\boldsymbol{u}} + E''\boldsymbol{u}''}) + \overline{p\widetilde{\boldsymbol{u}}} + \overline{\boldsymbol{u}''p} \tag{2.42}$$

$$= \overline{\rho}(\widetilde{E}\widetilde{\boldsymbol{u}} + \widetilde{E''\boldsymbol{u}''}) + \overline{p}\widetilde{\boldsymbol{u}} + \overline{\boldsymbol{u}''p}. \tag{2.43}$$

Substituting Eq. (2.43) into Eq. (2.39), and using Eqs. (2.21) and (2.22) yields

$$\nabla \cdot (\overline{\rho}\widetilde{E}\widetilde{\boldsymbol{u}}) + \nabla \cdot (\overline{p}\widetilde{\boldsymbol{u}}) = \nabla \cdot (\overline{\boldsymbol{u}\boldsymbol{\tau}}) - \nabla \overline{\boldsymbol{q}} - \nabla \cdot (\overline{\rho}\widetilde{E''\boldsymbol{u}''}) - \nabla \cdot (\overline{p\boldsymbol{u}''}), \tag{2.44}$$

where

$$\widetilde{E} = \widetilde{e} + \frac{\widetilde{\boldsymbol{u}} \cdot \widetilde{\boldsymbol{u}}}{2} + \frac{\widetilde{\boldsymbol{u}'' \cdot \boldsymbol{u}''}}{2}. \tag{2.45}$$

The turbulent kinetic energy $k(\boldsymbol{x}) \in \mathbb{R}$ can be defined as

$$k \triangleq \frac{\widetilde{\boldsymbol{u}'' \cdot \boldsymbol{u}''}}{2}. \tag{2.46}$$

After applying Favre averaging, the fluid governing equations are no longer closed. The following assumptions are used to simplify the Favre decomposition:

(A1) The fluid is an ideal gas is its temperature. Thus,

$$E + \frac{p}{\rho} = c_p T. \tag{2.47}$$

where $T(\boldsymbol{x}, t) \in \mathbb{R}$.

(A2) $\|\widetilde{\boldsymbol{\tau}}\|_{L_2} >> \|\overline{\boldsymbol{\tau}''}\|_{L_2} >$, where $\| \cdot \|_{L_2} >$ is L^2 norm.

(A3) $\|\nabla \widetilde{T}\|_{L_2} >> \|\nabla \overline{T''}\|_{L_2} >$.

(A4) Boussinesq [49] postulated that the turbulent transfer of momentum by eddies occurs in a gradient-transport manner analogous to the action of molecular viscosity in laminar flow. Based on the Boussinesq hypothesis, the Reynolds stress tensor, is a function of the mean rate of strain tensor $\widetilde{\boldsymbol{S}}$, and can be written as

$$\boldsymbol{R} = 2\mu_t\widetilde{\boldsymbol{S}} - \frac{2}{3}\overline{\rho}k\boldsymbol{I}, \tag{2.48}$$

where μ_t is the turbulent eddy viscosity tensor. It's common practice for eddy viscosity to be assumed to be isotropic and simplified to a scalar, $\mu_t(\boldsymbol{x}, t) \in \mathbb{R}$.

(A5) Turbulent transport of heat $c_p\overline{\rho\boldsymbol{u}''T}$ is modeled by a gradient approximation for the turbulent heat-flux.

(A6) $\frac{\overline{\rho\boldsymbol{u}''\boldsymbol{u}''\cdot\boldsymbol{u}''}}{2} - \overline{\boldsymbol{u}''\cdot\boldsymbol{\tau}}$, which relates to turbulent transport and molecular diffusion of turbulent kinetic energy, is approximated by the turbulent kinetic energy gradient as

$$\frac{\overline{\rho\boldsymbol{u}''\boldsymbol{u}''\cdot\boldsymbol{u}''}}{2} - \overline{\boldsymbol{u}''\cdot\boldsymbol{\tau}} = -\left(\mu + \mu_t\sigma_k\right)\nabla k, \tag{2.49}$$

where σ_k is a model constant.

(A7) The turbulent kinetic energy is much less than the average internal energy, that is, $k << c_p\widetilde{T}$.

Using (A1), Eq. (2.45), and Eqs. (2.21) – (2.25), it follows that

$$\overline{\rho\boldsymbol{u}''\widetilde{E''}} + \overline{p\boldsymbol{u}''} = \overline{\rho\boldsymbol{u}''(\frac{p}{\rho} + E'')} \tag{2.50}$$

$$= \overline{\rho\boldsymbol{u}''(\frac{p}{\rho} + E - \widetilde{E})} \tag{2.51}$$

$$= \overline{\rho\boldsymbol{u}''(c_pT + \frac{\boldsymbol{u}\cdot u}{2} - \widetilde{e} - \frac{\widetilde{\boldsymbol{u}}\cdot\widetilde{\boldsymbol{u}}}{2} - k)} \tag{2.52}$$

$$= \overline{\rho\boldsymbol{u}''(c_pT + \frac{(\widetilde{\boldsymbol{u}} + \boldsymbol{u}'')\cdot(\widetilde{\boldsymbol{u}} + \boldsymbol{u}'')}{2} - c_v\widetilde{T} - \frac{\widetilde{\boldsymbol{u}}\cdot\widetilde{\boldsymbol{u}}}{2} - k)} \tag{2.53}$$

$$= \overline{\rho\boldsymbol{u}''(c_pT + \boldsymbol{u}''\cdot\widetilde{\boldsymbol{u}} + \frac{\boldsymbol{u}''\cdot\boldsymbol{u}''}{2} + \frac{\widetilde{\boldsymbol{u}}\cdot\widetilde{\boldsymbol{u}}}{2} - c_v\widetilde{T} - \frac{\widetilde{\boldsymbol{u}}\cdot\widetilde{\boldsymbol{u}}}{2} - k)} \tag{2.54}$$

19

$$= \overline{\rho \boldsymbol{u}'' c_p T} + \overline{\rho \boldsymbol{u}'' (\boldsymbol{u}'' \cdot \widetilde{\boldsymbol{u}})} + \overline{\rho \boldsymbol{u}'' \frac{\boldsymbol{u}'' \cdot \boldsymbol{u}''}{2}} - \overline{\rho \boldsymbol{u}'' c_v \widetilde{\widetilde{T}}} - \overline{\rho \boldsymbol{u}'' k} \qquad (2.55)$$

$$= c_p \overline{\rho \boldsymbol{u}'' T} + \widetilde{\boldsymbol{u}} \cdot \overline{(\rho \boldsymbol{u}'' \boldsymbol{u}'')} + \frac{\overline{\rho \boldsymbol{u}'' \boldsymbol{u}'' \cdot \boldsymbol{u}''}}{2} \qquad (2.56)$$

$$= c_p \overline{\rho \boldsymbol{u}'' T} + \widetilde{\boldsymbol{u}} \cdot \boldsymbol{R} + \frac{\overline{\rho \boldsymbol{u}'' \boldsymbol{u}'' \cdot \boldsymbol{u}''}}{2}. \qquad (2.57)$$

Using (A2), Eq. (2.21), and Eq. (2.25), it follows that

$$\overline{\boldsymbol{\tau}} = \widetilde{\boldsymbol{\tau}}, \qquad (2.58)$$

and

$$\overline{\boldsymbol{u} \cdot \boldsymbol{\tau}} = \overline{(\widetilde{\boldsymbol{u}} + \boldsymbol{u}'') \cdot \boldsymbol{\tau}} \qquad (2.59)$$

$$= \overline{\widetilde{\boldsymbol{u}} \cdot (\widetilde{\boldsymbol{\tau}} + \boldsymbol{\tau}'')} + \overline{\boldsymbol{u}'' \cdot \boldsymbol{\tau}} \qquad (2.60)$$

$$= \widetilde{\boldsymbol{u}} \cdot \widetilde{\boldsymbol{\tau}} + \overline{\boldsymbol{u}'' \cdot \boldsymbol{\tau}}. \qquad (2.61)$$

Using (A3), $\overline{\boldsymbol{q}}$ can be rewritten as

$$\overline{\boldsymbol{q}} = -c_p \frac{\mu}{Pr} \nabla \widetilde{T} - c_p \frac{\mu}{Pr} \nabla \overline{T''} \qquad (2.62)$$

$$= -c_p \frac{\mu}{Pr} \nabla \widetilde{T}, \qquad (2.63)$$

where Prandtl number Pr is a fluid property constant. Using (A5), $c_p \overline{\rho \boldsymbol{u}'' T}$ can be

rewritten as

$$c_p \overline{\rho \boldsymbol{u}'' T} = -c_p \frac{\mu_t}{Pr_t} \nabla \widetilde{T}, \qquad (2.64)$$

where Pr_t is the turbulent Prandtl number, usually equal to 0.9. From (A6), the turbulent transport and molecular diffusion of turbulent kinetic energy terms $\overline{\rho \boldsymbol{u}'' \boldsymbol{u}'' \cdot \boldsymbol{u}''}/2 - \overline{\boldsymbol{u}'' \boldsymbol{\tau}}$ can be rewritten using the gradient of the turbulent kinetic energy. This term is small when compared to the diffusive energy and convective energy, as demonstrated in DNS simulations [50]. Therefore, it is neglected in the energy equation with the assumption as

$$\frac{\overline{\rho \boldsymbol{u}'' \boldsymbol{u}'' \cdot \boldsymbol{u}''}}{2} - \overline{\boldsymbol{u}'' \boldsymbol{\tau}} = 0. \qquad (2.65)$$

Thus substituting Eqs. (2.48) and (2.58) into Eq. (2.38), and substituting Eqs. (2.48), (2.57), (2.58), (2.61), (2.63), (2.64) and (2.65) into Eq. (2.44), we obtain the steady-state Favre-averaged governing equations, which are

$$\nabla \cdot (\overline{\rho}\widetilde{\boldsymbol{u}}) = 0, \tag{2.66}$$

$$\nabla \cdot (\overline{\rho}\widetilde{\boldsymbol{u}}\widetilde{\boldsymbol{u}}) = -\nabla\overline{p} + \nabla \cdot (\boldsymbol{R} + \widetilde{\boldsymbol{\tau}}), \tag{2.67}$$

$$\nabla \cdot (\overline{\rho}\widetilde{E}\widetilde{\boldsymbol{u}}) = -\nabla \cdot (\overline{p}\widetilde{\boldsymbol{u}}) + \nabla \cdot [\widetilde{\boldsymbol{u}} \cdot (\boldsymbol{R} + \widetilde{\boldsymbol{\tau}})] - \nabla \cdot \left[c_p \nabla \widetilde{T}(\frac{\mu}{Pr} + \frac{\mu_t}{Pr_t}) \right], \tag{2.68}$$

where

$$\boldsymbol{R} + \widetilde{\boldsymbol{\tau}} = 2(\mu + \mu_t)\widetilde{\boldsymbol{S}} - \frac{2}{3}\overline{\rho}k\boldsymbol{I}. \tag{2.69}$$

To add time-dependence back into the equations, we can assume that turbulent fluctuations occur at a small time scale, t_1. Applying time-averaging over a time scale t_1 yields a set of steady-state governing equations. However, on a longer time scale t_2, where $t_2 \gg t_1$, the fluid flow may still be unsteady (for example, as in the case of large-scale vortex shedding). The scales are illustrated in Fig. 2.1,
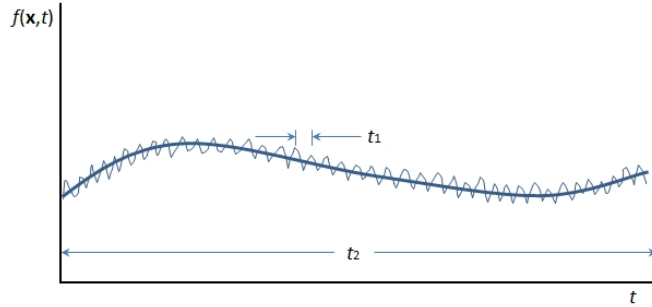
Figure 2.1: Turbulence time scale t_1 compare with average time scale t_2.

For a condition where $t_2 \gg t_1$, Favre-averaging is assumed to statistically converge at time scale t_1, but over time scales t_2, the flow field is changing only gradually, thus the time-derivative can be re-introduced into the equation to allow for some form of unsteadiness. In this case, the unsteady Favre-averaged governing equations be-

come

$$\frac{\partial \overline{\rho}}{\partial t} + \nabla \cdot (\overline{\rho}\widetilde{\boldsymbol{u}}) = 0, \tag{2.70}$$

$$\frac{\partial (\overline{\rho}\widetilde{\boldsymbol{u}})}{\partial t} + \nabla \cdot (\overline{\rho}\widetilde{\boldsymbol{u}}\widetilde{\boldsymbol{u}}) = -\nabla \overline{p} + \nabla \cdot (\boldsymbol{R} + \widetilde{\boldsymbol{\tau}}), \tag{2.71}$$

$$\frac{\partial (\overline{\rho}\widetilde{E})}{\partial t} + \nabla \cdot (\overline{\rho}\widetilde{E}\widetilde{\boldsymbol{u}}) = -\nabla \cdot (\overline{p}\widetilde{\boldsymbol{u}}) + \nabla \cdot [\widetilde{\boldsymbol{u}} \cdot (\boldsymbol{R} + \widetilde{\boldsymbol{\tau}})] - \nabla \cdot \left[c_p \nabla \widetilde{T}(\frac{\mu}{Pr} + \frac{\mu_t}{Pr_t}) \right], \tag{2.72}$$

where

$$\widetilde{E} = c_v \widetilde{T} + \frac{\widetilde{\boldsymbol{u}} \cdot \widetilde{\boldsymbol{u}}}{2} + k = c_p \widetilde{T} + \frac{\widetilde{\boldsymbol{u}} \cdot \widetilde{\boldsymbol{u}}}{2} + k - \frac{p}{\rho}, \tag{2.73}$$

$$\widetilde{\boldsymbol{S}} = -\frac{1}{3}\nabla \cdot \widetilde{\boldsymbol{u}}\boldsymbol{I} + \frac{1}{2}(\nabla \widetilde{\boldsymbol{u}} + (\nabla \widetilde{\boldsymbol{u}})^{rmT}), \tag{2.74}$$

$$\boldsymbol{R} = 2\mu_t \widetilde{\boldsymbol{S}} - \frac{2}{3}\overline{\rho}k\boldsymbol{I}, \tag{2.75}$$

$$\widetilde{\boldsymbol{\tau}} = 2\mu\widetilde{\boldsymbol{S}}. \tag{2.76}$$

In these equations, assuming that μ_t is provided by some form of the model, there are five variables, which are average velocity $\widetilde{\boldsymbol{u}}$, average pressure $\overline{p}$, and average temperature $\widetilde{T}$.

2.5.2 Reynolds-averaged governing equations for incompressible flow

For incompressible flow, the density gradients over time and space are both zero. For convenience, the continuity and momentum equations of incompressible flow are

$$\nabla \cdot \boldsymbol{u} = 0, \tag{2.77}$$

$$\frac{\partial \boldsymbol{u}}{\partial t} + \nabla \cdot (\boldsymbol{u}\boldsymbol{u}) = -\frac{\nabla p}{\rho} + \frac{1}{\rho}\nabla \cdot (\boldsymbol{\tau}). \tag{2.78}$$

Reynolds decomposing $\boldsymbol{u}$ into a time-averaged part $\bar{\boldsymbol{u}}$ and time-varying part $\boldsymbol{u}'$, and then time-averaging the divergence-free equation (2.77) yields

$$\nabla \cdot \bar{\boldsymbol{u}} = 0. \tag{2.79}$$

turbulence kinetic viscosity (m^2/s) The same process can be followed for the momentum equation (2.78). However, unlike for the divergence free equation, and like the compressible flow equation, Reynolds decomposing and averaging the nonlinear convective term produces the Reynolds stress tensor

$$\nabla \cdot (\overline{\boldsymbol{uu}}) = \nabla \cdot (\bar{\boldsymbol{u}}\bar{\boldsymbol{u}}) - \frac{1}{\rho}\nabla \cdot \boldsymbol{R}. \tag{2.80}$$

Thus, following Reynolds decomposition and averaging Eq. (2.78) yields

$$\nabla \cdot (\bar{\boldsymbol{u}}\bar{\boldsymbol{u}}) = -\frac{\nabla \bar{p}}{\rho} + \frac{1}{\rho}\nabla \cdot (\bar{\boldsymbol{\tau}} + \boldsymbol{R}). \tag{2.81}$$

As with the Favre-averaged form, for slowly evolving unsteady flows, the time dependent terms can be retained. Thus, the governing equations in Reynolds-averaged form are

$$\nabla \cdot \bar{\boldsymbol{u}} = 0, \tag{2.82}$$

$$\frac{\partial \bar{\boldsymbol{u}}}{\partial t} + \nabla \cdot (\bar{\boldsymbol{u}}\bar{\boldsymbol{u}}) = -\frac{\nabla \bar{p}}{\rho} + \frac{1}{\rho}\nabla \cdot (\bar{\boldsymbol{\tau}} + \boldsymbol{R}), \tag{2.83}$$

$$\boldsymbol{R} = 2\mu_t \bar{\boldsymbol{S}} - \frac{2}{3}\rho k \boldsymbol{I}, \tag{2.84}$$

$$\bar{\boldsymbol{\tau}} = 2\mu \bar{\boldsymbol{S}}, \tag{2.85}$$

$$\bar{\boldsymbol{S}} = \frac{1}{2}(\nabla \bar{\boldsymbol{u}} + (\nabla \bar{\boldsymbol{u}})^{\mathrm{T}}). \tag{2.86}$$

Note that here the first term on the right hand side of the $\bar{\boldsymbol{S}}$ equation is retained for consistency with the Favre-averaged equations, even though it is zero due to the divergence-free condition. Also, note that for incompressible flows, the turbulent kinetic energy is defined as

$$k \triangleq \frac{\overline{\boldsymbol{u}' \cdot \boldsymbol{u}'}}{2}. \tag{2.87}$$

In these equations, assuming that μ_t is provided by some form of model, there are four variables, which are average velocity $\bar{\boldsymbol{u}}$ and average pressure $\bar{p}$.

23

2.5.3 Derivation of the k-ω model equations

RANS models are required to model the Reynolds stress, typically by finding an expression for μ_t. Among these models, the k-ω model has become a mature and reliable RANS eddy-viscosity model. Here, the derivation is presented for the compressible form of the model, but the primary difference between compressible and incompressible forms is simply through whether Favre- or Reynolds-averaging is employed. To derive the k-ω turbulence model, the following assumptions are needed:

(A8) The trace of Reynolds stress tensor is proportional to the turbulent kinetic energy per unit volume, that is

$$\text{tr}(\boldsymbol{R}) = -2\rho k, \tag{2.88}$$

where tr is the trace.

(A9) $\text{tr}\left(\frac{1}{2}\overline{\rho \boldsymbol{u}''\boldsymbol{u}''\boldsymbol{u}''} + \widetilde{\boldsymbol{u}''p''\boldsymbol{I}}\right) = -\mu_t \sigma_k \nabla k.$

(A10) Dissipation rate $\varepsilon(\boldsymbol{x}, t) \in \mathbb{R}$ is a function of turbulent kinetic energy and turbulent length scale $\ell \in \mathbb{R}$ [51], expressed by $\varepsilon = \beta^* k^{3/2}/\ell$, where β^* is a model constant.

(A11) For subsonic flow and incompressible flow,

$$\text{tr}\left(\overline{\frac{1}{3}\boldsymbol{u}''\nabla \cdot \mu(\nabla \cdot \boldsymbol{u}''\boldsymbol{I})} - \overline{p''\nabla \boldsymbol{u}''}\right) = 0. \tag{2.89}$$

The momentum equations(2.2) times $\boldsymbol{u}''$ yields

$$\overline{\boldsymbol{u}''(\frac{\partial \rho \boldsymbol{u}}{\partial t} + \nabla \cdot (\rho \boldsymbol{u}\boldsymbol{u}) + \nabla p - \nabla \cdot \boldsymbol{\tau})} = 0, \tag{2.90}$$

which is rearranged as

$$\overline{\boldsymbol{u}''\frac{\partial \rho \boldsymbol{u}}{\partial t}} + \overline{\boldsymbol{u}''\nabla \cdot (\rho \boldsymbol{u}\boldsymbol{u})} + \overline{\boldsymbol{u}''\nabla p} - \overline{\boldsymbol{u}''\nabla \cdot \boldsymbol{\tau}} = 0. \tag{2.91}$$

Using $\boldsymbol{u} = \widetilde{\boldsymbol{u}} + \boldsymbol{u}''$ and Eqs. (2.21)–(2.25), the unsteady term in Eq. (2.91) can be expressed as

$$\overline{\boldsymbol{u}''\frac{\partial\rho\boldsymbol{u}}{\partial t}} = \overline{\boldsymbol{u}''\frac{\partial\rho(\widetilde{\boldsymbol{u}}+\boldsymbol{u}'')}{\partial t}} \tag{2.92}$$

$$= \overline{\boldsymbol{u}''\frac{\partial\rho\widetilde{\boldsymbol{u}}+\rho\boldsymbol{u}''}{\partial t}} \tag{2.93}$$

$$= \widetilde{\boldsymbol{u}''}\frac{\partial\overline{\rho}\widetilde{\boldsymbol{u}}}{\partial t} + \overline{\boldsymbol{u}''\frac{\partial\rho\boldsymbol{u}''}{\partial t}} \tag{2.94}$$

$$= \overline{\boldsymbol{u}''\frac{\partial\rho\boldsymbol{u}''}{\partial t}} \tag{2.95}$$

$$= \frac{1}{2}\frac{\partial\overline{\rho\boldsymbol{u}''\boldsymbol{u}''}}{\partial t} \tag{2.96}$$

$$= -\frac{1}{2}\frac{\partial\boldsymbol{R}}{\partial t}. \tag{2.97}$$

The convective term in Eq. (2.91) can be expressed as

$$\overline{\boldsymbol{u}''\nabla\cdot(\rho\boldsymbol{u}\boldsymbol{u})} = \overline{\boldsymbol{u}''\nabla\cdot[\rho(\widetilde{\boldsymbol{u}}+\boldsymbol{u}'')(\widetilde{\boldsymbol{u}}+\boldsymbol{u}'')]} \tag{2.98}$$

$$= \overline{\boldsymbol{u}''\nabla\cdot(\rho\widetilde{\boldsymbol{u}}\widetilde{\boldsymbol{u}}+\boldsymbol{u}''\widetilde{\boldsymbol{u}}+\widetilde{\boldsymbol{u}}\boldsymbol{u}''+\boldsymbol{u}''\boldsymbol{u}'')} \tag{2.99}$$

$$= \overline{\boldsymbol{u}''\nabla\cdot(\rho\widetilde{\boldsymbol{u}}\widetilde{\boldsymbol{u}})} + \overline{\boldsymbol{u}''\nabla\cdot(\rho\boldsymbol{u}''\widetilde{\boldsymbol{u}})} + \overline{\boldsymbol{u}''\nabla\cdot(\rho\widetilde{\boldsymbol{u}}\boldsymbol{u}'')} + \overline{\boldsymbol{u}''\nabla\cdot(\rho\boldsymbol{u}''\boldsymbol{u}'')} \tag{2.100}$$

$$= 0 + \overline{\boldsymbol{u}''\nabla\cdot(\rho\boldsymbol{u}''\widetilde{\boldsymbol{u}})} + \overline{\boldsymbol{u}''((\rho\boldsymbol{u}''\cdot\nabla)\widetilde{\boldsymbol{u}}+\widetilde{\boldsymbol{u}}(\nabla\cdot\rho\boldsymbol{u}''))} + \overline{\boldsymbol{u}''\nabla\cdot(\rho\boldsymbol{u}''\boldsymbol{u}'')} \tag{2.101}$$

$$= \frac{1}{2}\overline{\nabla\cdot(\rho\boldsymbol{u}''\boldsymbol{u}''\widetilde{\boldsymbol{u}})} + \overline{\boldsymbol{u}''(\rho\boldsymbol{u}''\cdot\nabla)\widetilde{\boldsymbol{u}}} + \frac{1}{2}\overline{\nabla\cdot(\rho\boldsymbol{u}''\boldsymbol{u}''\boldsymbol{u}'')} \tag{2.102}$$

$$= -\frac{1}{2}\nabla\cdot(\boldsymbol{R}\widetilde{\boldsymbol{u}}) - (\boldsymbol{R}\cdot\nabla)\widetilde{\boldsymbol{u}} + \frac{1}{2}\nabla\cdot(\overline{\rho\boldsymbol{u}''\boldsymbol{u}''\boldsymbol{u}''}). \tag{2.103}$$

The pressure gradient term in Eq. (2.91) can be expressed as

$$\overline{\boldsymbol{u}''\nabla p} = \overline{\boldsymbol{u}''\nabla(\widetilde{p}+p'')} \tag{2.104}$$

$$= \overline{\boldsymbol{u}''\nabla p''} \tag{2.105}$$

$$= \nabla\cdot\overline{(p''\boldsymbol{u}''\boldsymbol{I})} - \overline{p''\nabla\boldsymbol{u}''}. \tag{2.106}$$

The viscous term in Eq. (2.91) can be expressed as

$$\overline{\boldsymbol{u}''\nabla\cdot\boldsymbol{\tau}} = \overline{\boldsymbol{u}''\nabla\cdot\mu\left[-\frac{2}{3}\nabla\cdot\boldsymbol{u}\boldsymbol{I}+\nabla\boldsymbol{u}+(\nabla\boldsymbol{u})^{\mathrm{T}}\right]} \tag{2.107}$$

25

$$=\overline{\boldsymbol{u}''\nabla\cdot\mu\left[-\frac{2}{3}\nabla\cdot(\widetilde{\boldsymbol{u}}+\boldsymbol{u}'')\boldsymbol{I}+\nabla(\widetilde{\boldsymbol{u}}+\boldsymbol{u}'')+(\nabla(\widetilde{\boldsymbol{u}}+\boldsymbol{u}''))^{\mathrm{T}}\right]} \quad (2.108)$$

$$=-\overline{\frac{2}{3}\boldsymbol{u}''\nabla\cdot\mu(\nabla\cdot\boldsymbol{u}''\boldsymbol{I})}+\overline{\boldsymbol{u}''\nabla\cdot(\mu\nabla\boldsymbol{u}'')}+\overline{\boldsymbol{u}''\nabla\cdot\mu(\nabla\boldsymbol{u}'')^{\mathrm{T}}} \quad (2.109)$$

$$=\overline{\frac{1}{3}\boldsymbol{u}''\nabla\cdot\mu(\nabla\cdot\boldsymbol{u}''\boldsymbol{I})}+\overline{\boldsymbol{u}''\nabla\cdot(\mu\nabla\boldsymbol{u}'')} \quad (2.110)$$

$$=\overline{\frac{1}{3}\boldsymbol{u}''\nabla\cdot\mu(\nabla\cdot\boldsymbol{u}''\boldsymbol{I})}+\overline{\nabla\cdot\mu(\boldsymbol{u}''\nabla\boldsymbol{u}'')}-\overline{(\mu\nabla\boldsymbol{u}''\cdot\nabla)\boldsymbol{u}''} \quad (2.111)$$

$$=\overline{\frac{1}{3}\boldsymbol{u}''\nabla\cdot\mu(\nabla\cdot\boldsymbol{u}''\boldsymbol{I})}+\frac{1}{2}\nu\triangle(\rho\boldsymbol{u}''\boldsymbol{u}'')-\overline{(\mu\nabla\boldsymbol{u}''\cdot\nabla)\boldsymbol{u}''} \quad (2.112)$$

$$=\overline{\frac{1}{3}\boldsymbol{u}''\nabla\cdot\mu(\nabla\cdot\boldsymbol{u}''\boldsymbol{I})}-\frac{\nu\triangle\boldsymbol{R}}{2}-\overline{(\mu\nabla\boldsymbol{u}''\cdot\nabla)\boldsymbol{u}''}, \quad (2.113)$$

where $\nu(T)\in\mathbb{R}$ is the kinematic viscosity equal to μ/ρ, and the symbol $\triangle$ means $\nabla\cdot\nabla$. Thus, substituting Eqs. (2.97)–(2.113) into Eq. (2.91) yields

$$-\frac{1}{2}\frac{\partial\boldsymbol{R}}{\partial t}-\frac{1}{2}\nabla\cdot(\boldsymbol{R}\widetilde{\boldsymbol{u}})-(\boldsymbol{R}\cdot\nabla)\widetilde{\boldsymbol{u}}+\frac{1}{2}\nabla\cdot(\overline{\rho\boldsymbol{u}''\boldsymbol{u}''\boldsymbol{u}''})+\nabla\cdot(\overline{\boldsymbol{u}''p''\boldsymbol{I}})-\overline{\frac{1}{3}\boldsymbol{u}''\nabla\cdot\mu(\nabla\cdot\boldsymbol{u}''\boldsymbol{I})}$$
$$(2.114)$$

$$-\overline{p''\nabla\boldsymbol{u}''}+\frac{1}{2}\nu\triangle\boldsymbol{R}+\overline{(\mu\nabla\boldsymbol{u}''\cdot\nabla)\boldsymbol{u}''}=0. \quad (2.115)$$

Using (A8) and rearrangement, Eq. (2.115) yields

$$\frac{\partial\rho k}{\partial t}+\nabla\cdot(\rho k\widetilde{\boldsymbol{u}})=\boldsymbol{R}\cdot\nabla\widetilde{\boldsymbol{u}}-\overline{\mu(\nabla\boldsymbol{u}'')\cdot(\nabla\boldsymbol{u}'')}+\nabla\cdot(\mu\nabla k-tr(\frac{1}{2}\overline{\rho\boldsymbol{u}''\boldsymbol{u}''\boldsymbol{u}''}+\widetilde{\boldsymbol{u}''p''\boldsymbol{I}}))$$
$$(2.116)$$

$$+tr(\overline{\frac{1}{3}\boldsymbol{u}''\nabla\cdot\mu(\nabla\cdot\boldsymbol{u}''\boldsymbol{I})}-\overline{p''\nabla\boldsymbol{u}''}). \quad (2.117)$$

Using (A9), Eq. (2.117) can be rewritten as:

$$\frac{\partial\rho k}{\partial t}+\nabla\cdot(\rho k\widetilde{\boldsymbol{u}})=\boldsymbol{R}\cdot\nabla\widetilde{\boldsymbol{u}}-\overline{\mu(\nabla\boldsymbol{u}'')\cdot(\nabla\boldsymbol{u}'')}+\nabla\cdot((\mu+\mu_t\sigma_k)\nabla k) \quad (2.118)$$

$$+tr(\overline{\frac{1}{3}\boldsymbol{u}''\nabla\cdot\mu(\nabla\cdot\boldsymbol{u}''\boldsymbol{I})}-\overline{p''\nabla\boldsymbol{u}''}). \quad (2.119)$$

The term $\overline{\mu(\nabla\boldsymbol{u}'')\cdot(\nabla\boldsymbol{u}'')}$ is the rate of dissipation of turbulent kinetic energy per unit mass, $\varepsilon(\boldsymbol{x},t)$. Within the k-ω model a new variable $\omega(\boldsymbol{x},t)\in\mathbb{R}$ is introduced,

referred to as the specific dissipation rate, which has a dimension of $1/t$. Using (A10), the dissipation term can be rewritten as

$$\overline{\mu(\nabla \boldsymbol{u}'') \cdot (\nabla \boldsymbol{u}'')} = \rho\varepsilon = \rho\beta^* k\omega. \tag{2.120}$$

Using (A10), Eq. (2.119) can be written into turbulent kinetic energy equation as

$$\frac{\partial(\rho k)}{\partial t} + \nabla \cdot (\rho k \widetilde{\boldsymbol{u}}) = \nabla \cdot ((\mu + \mu_t \sigma_k)\nabla k) + S_k, \tag{2.121}$$

where

$$S_k = P_k - D_k, \tag{2.122}$$

$$P_k = \boldsymbol{R} \cdot \nabla \widetilde{\boldsymbol{u}}, \tag{2.123}$$

$$D_k = \rho\beta^* \omega k. \tag{2.124}$$

In order to close this turbulent model, an equation describing specific dissipation rate ω must be established. Unlike k, there is no formal governing equation which can be derived for ω, so it is assumed it follows similar transport behavior as k. Following the form of turbulent kinetic energy equation, the ω equation should also have an unsteady term, a convective term, a viscous term and a source term. Kolmogorov [52] first presented a simple form of such a transport equation for ω. After much improvement [51], the ω equation has evolved to

$$\frac{\partial(\rho\omega)}{\partial t} + \nabla \cdot (\rho\omega \widetilde{\boldsymbol{u}}) = \nabla \cdot ((\mu + \mu_t \sigma_\omega)\nabla \omega) + S_\omega, \tag{2.125}$$

where α, β, and σ_ω are constants, and

$$S_\omega = P_\omega - D_\omega, \tag{2.126}$$

$$P_\omega = \alpha\frac{\omega}{k}P_k, \tag{2.127}$$

$$D_\omega = \beta\rho\omega^2. \tag{2.128}$$

Assuming that eddy viscosity can be expressed by turbulent kinetic energy k and turbulent length scale, ℓ, then it is assumed

$$\mu_t = \rho k^{1/2}\ell. \tag{2.129}$$

According to the dimensions of ω, this implies that the eddy viscosity should take the form

$$\mu_t = \rho \frac{k}{\omega} \tag{2.130}$$

which allows for determination of the eddy viscosity from k and ω, which themselves are found through simultaneous solution of their respective transport equations with the RANS equation.

Thus, the Favre-averaged compressible governing equations including the k-ω turbulence model are

$$\frac{\partial \overline{\rho}}{\partial t} + \nabla \cdot (\overline{\rho}\widetilde{\boldsymbol{u}}) = 0, \tag{2.131}$$

$$\frac{\partial (\overline{\rho}\widetilde{\boldsymbol{u}})}{\partial t} + \nabla \cdot (\overline{\rho}\widetilde{\boldsymbol{u}}\widetilde{\boldsymbol{u}}) = -\nabla \overline{p} + \nabla \cdot (\boldsymbol{R} + \widetilde{\boldsymbol{\tau}}), \tag{2.132}$$

$$\frac{\partial (\overline{\rho}\widetilde{E})}{\partial t} + \nabla \cdot (\overline{\rho}\widetilde{E}\widetilde{\boldsymbol{u}}) = -\nabla \cdot (\overline{p}\widetilde{\boldsymbol{u}}) + \nabla \cdot [\widetilde{\boldsymbol{u}} \cdot (\boldsymbol{R} + \widetilde{\boldsymbol{\tau}})] - \nabla \cdot \left[c_p \nabla \widetilde{T}(\frac{\mu}{Pr} + \frac{\mu_t}{Pr_t}) \right], \tag{2.133}$$

$$\frac{\partial (\rho k)}{\partial t} + \nabla \cdot (\rho k \widetilde{\boldsymbol{u}}) = \nabla \cdot ((\mu + \mu_t \sigma_k)\nabla k) + S_k, \tag{2.134}$$

$$\frac{\partial (\rho \omega)}{\partial t} + \nabla \cdot (\rho \omega \widetilde{\boldsymbol{u}}) = \nabla \cdot ((\mu + \mu_t \sigma_\omega)\nabla \omega) + S_\omega, \tag{2.135}$$

$$\mu_t = \rho \frac{k}{\omega}, \tag{2.136}$$

where

$$\widetilde{E} = c_v \widetilde{T} + \frac{\widetilde{\boldsymbol{u}} \cdot \widetilde{\boldsymbol{u}}}{2} + k = c_p \widetilde{T} + \frac{\widetilde{\boldsymbol{u}} \cdot \widetilde{\boldsymbol{u}}}{2} + k - \frac{p}{\rho}, \tag{2.137}$$

$$\widetilde{\boldsymbol{S}} = -\frac{1}{3}\nabla \cdot \widetilde{\boldsymbol{u}}\boldsymbol{I} + \frac{1}{2}(\nabla \widetilde{\boldsymbol{u}} + (\nabla \widetilde{\boldsymbol{u}})^{\mathrm{T}}), \tag{2.138}$$

$$\boldsymbol{R} = 2\mu_t \widetilde{\boldsymbol{S}} - \frac{2}{3}\overline{\rho}k\boldsymbol{I}, \tag{2.139}$$

$$\widetilde{\boldsymbol{\tau}} = 2\mu \widetilde{\boldsymbol{S}}, \tag{2.140}$$

$$S_k = P_k - D_k, \tag{2.141}$$

$$P_k = \boldsymbol{R} \cdot \nabla \widetilde{\boldsymbol{u}}, \tag{2.142}$$

$$D_k = \rho \beta^* \omega k, \tag{2.143}$$

$$S_\omega = P_\omega - D_\omega, \tag{2.144}$$

$$P_\omega = \alpha \frac{\omega}{k} P_k, \tag{2.145}$$

$$D_\omega = \beta \rho \omega^2. \tag{2.146}$$

The turbulence model given by Eqs. (2.131)–(2.136) has 5 closure coefficients, which are σ_k, σ_ω, β^*, β, and α.

2.6   Adaptation methods currently applied in turbulence simulation

The concept of *adaptation* has been employed in a variety of ways to improve the accuracy of turbulent flow simulations. Most commonly, adaptation of the solution mesh is used to improve solution accuracy and reduce computational cost. This is done by dividing or merging cells to better resolve areas of complex flow and reduce resolution in regions of near uniformity (e.g., [53, 54]). However, in some cases, the turbulence models themselves also include some form of adaptation. Several adaptive RANS approaches have been proposed. Larsson, et al. [55] proposed an algorithm using a hybrid LES/RANS method through feedback to find the appropriate forcing amplitude which could greatly increase the accuracy of the solution and reduce the calculation cost at the same time. Knopp, et al. [56] used a grid and flow adaptive wall-function method on the Spalart-Allmaras and SST k-ω RANS models to improve the accuracy of turbulence simulation. Menter, et al. [57, 58] introduced an adjustable length-scale into the turbulence scale equation. By adjusting length-scale, unsteady RANS could get a better unsteady solutions. Menter and his colleagues [59, 60] also applied this method to the SST model and RANS/LES hybrid methods. Magagnato and Gabi [61] split the turbulent kinetic energy and dissipation rate of RANS k-ϵ model into resolved and unresolved subgrid parts and evaluated the subgrid part by a new k-τ equation. This new model produced good results for rotating machinery. Medic et al. [62] applied adaptive wall functions developed for the flow over a flat

plate and got good accuracy on coarse grids. Wakers and colleagues [63] applied an adaptive grid refinement method in a RANS model to investigate forces on the surface of the ship. Based on the coarse grid solution, the grid refinement procedure can adaptively refine regions where velocity gradients change dramatically. Ralf, et al. [64] did similar grid-refinement on the $k\text{-}\omega$ model. Winkler, et al. [65] applied a scale adaptive simulation turbulence model based on the SST turbulence model by adding a source term into the dissipation rate equation. This source term accounts for unsteadiness in the flow. Results were similar to the delayed detached-eddy simulation method in isotropic turbulence as well as predicted aerodynamic metrics. Orkun Temel, et al. [66, 67] propose several sets of adapted value of closure coefficients of RANS turbulence model based on the Monin–Obukhov similarity theory, which could improve the accuracy of atmospheric boundary layer in numerical weather weather prediction. Gauthier, et al. [68] applied a scale-adaptive turbulence modeling on oscillating-foil turbines and compared the result with Spalart-Allmaras model. It was shown that in 3-D the two models do not have a big difference. However, the scale adaptive simulation model obtains finer wake structures.

The above adaptive approaches are often implemented with RANS models and use the current iteration of the simulated flow for adaptation. Conversely, data assimilation has long been implemented with non-RANS models to improve flow-field reconstruction or prediction (e.g., [69, 70, 71]). The most common application is meteorology, although it is also used in other areas such as training simple fluid models to produce realistic-looking computer generated scenes in real time [72]. In meteorological modeling, measurement data can be incorporated in a computational fluid dynamics model using approaches ranging from simple interpolation to direct incorporation in the governing equations [73]. For example, V. Perez-Munnuzuri, et al. [74] uses a nonlinear forecasting method, which is based on the reconstruction of a chaotic strange attractor, to predict the behavior of cloud coverage based on data

30

from previous years. As another example, Y. Lee, et al. [75] apply a multi-scale data assimilation method, which is based on stochastic superparameterization, to forecast the turbulent signals at different levels of scale.

An adjoint method [76, 77, 78, 79, 80] is also applied for optimizing the parameters that exists inside mechanical or aerodynmic designs, and energy transportation systems. Instead of using complex differentiation [81], an automatic differentiation procedure [82] is applied together with the adjoint method. However, due to the computational cost of the adjoint method, this approach is unsuitable for turbulence modeling [83, 84].

Recently, data-driven and data-assimilation approaches have begun to be used with RANS models. For example, [85] uses machine learning tools, such as artificial neural networks and Gaussian process regression, to produce a model for an intermittency parameter introduced into the $k\text{-}\omega$ equations to better predict bypass transition in boundary layers. [86] uses high-fidelity simulation and experimental data with a new machine learning method, multiscale Gaussian process regression, to develop more accurate turbulence model closure. The result highlight the potential of machine learning method as a data-driven modeling tool. They also apply this new data-driven method to transitional modeling [87]. Foures et al. [88] do not employ a closure model but instead replace the Reynolds stress term in the RANS equation with a forcing function and adapt that function.

In the case where some measurement information is available, data-driven approaches can be used to calibrate closure coefficients. For example, [89] uses a database of high-fidelity LES to calibrate a mixing-length turbulence model to reduce the computational cost of simulating the flow in wind farms.

Chapter 3 KATS Solver

The KATS [90, 91, 92, 93, 94] computing framework is used to implement the CFD governing equations. KATS uses the CGNS format of computational grid and takes advantage of parallel computing through domain decomposition through ParMETIS [95] and OpenMPI [96]. It also utilizes the PETSc library [97, 98, 99], which uses flexible generalized minimal residual method (FGMRES) to solve large and sparse linear systems.

KATS, uses a finite-volume approach to solve governing equations. These equations are cast in a conservative form

$$\frac{\partial \boldsymbol{Q}}{\partial t} + \nabla \cdot (\boldsymbol{\mathcal{F}} - \boldsymbol{\mathcal{F}}_d) = \boldsymbol{S}_v, \tag{3.1}$$

where $\boldsymbol{Q}$ represent the conservative quantities, $\boldsymbol{\mathcal{F}}$ the advective flux, $\boldsymbol{\mathcal{F}}_d$ the diffusive flux, and $\boldsymbol{S}_v$ the source terms. This equation is then integrated over each cell volume V of the mesh to give

$$\int_V \frac{\partial \boldsymbol{Q}}{\partial t} \, dV = \int_V \nabla \cdot (\boldsymbol{\mathcal{F}}_d - \boldsymbol{\mathcal{F}}) \, dV + \int_V \boldsymbol{S}_v \, dV. \tag{3.2}$$

The divergence theorem can be applied to the second term of this equation to yield

$$\int_V \frac{\partial \boldsymbol{Q}}{\partial t} \, dV = \int_A (\boldsymbol{\mathcal{F}}_d - \boldsymbol{\mathcal{F}}) \cdot \boldsymbol{n} \, dA + \int_V \boldsymbol{S}_v \, dV, \tag{3.3}$$

where $\boldsymbol{n} = (n_x, n_y, n_z)$ represents normal vector of the boundary face A. Assuming that all quantities are constant over cell V, and over the the boundaries of the cell, the integral form equation becomes

$$V \frac{\partial \boldsymbol{Q}}{\partial t} = \sum_{\text{face}} (\boldsymbol{\mathcal{F}}_d - \boldsymbol{\mathcal{F}}) \cdot \boldsymbol{n} A + \boldsymbol{S}_v V. \tag{3.4}$$

To facilitate and optimize the evaluation of flow properties, KATS uses primitive variables in the numerical scheme. In order to do so while preserving the conservative

form of the equations, the vector of primitive variable $\boldsymbol{P}$, is introduced. First, vector $\boldsymbol{\mathcal{R}}$ is defined

$$\boldsymbol{\mathcal{R}} \triangleq \sum_{\text{face}} (\boldsymbol{\mathcal{F}}_d - \boldsymbol{\mathcal{F}}) \cdot \boldsymbol{n} A + \boldsymbol{S}_v V, \tag{3.5}$$

and the Jacobian $\partial \boldsymbol{Q}/\partial \boldsymbol{P}$ is introduce. Equation (3.3) can thus be written as

$$V \frac{\partial \boldsymbol{Q}}{\partial \boldsymbol{P}} \frac{\partial \boldsymbol{P}}{\partial t} = \boldsymbol{\mathcal{R}}. \tag{3.6}$$

This approach also enables preconditioning by only modifying specific terms in Jacobian $\partial \boldsymbol{Q}/\partial \boldsymbol{P}$. Discretizing Eq. (3.6) in time using first order implicit Euler formulation, yields

$$\frac{(\boldsymbol{P}^{n+1} - \boldsymbol{P}^n)}{\Delta t} \left(\frac{\partial \boldsymbol{Q}}{\partial \boldsymbol{P}} \right)^n V = \boldsymbol{R}^{n+1}. \tag{3.7}$$

The right hand side $\boldsymbol{\mathcal{R}}^{n+1}$ can be linearised using first order Taylor expansion

$$\frac{(\boldsymbol{P}^{n+1} - \boldsymbol{P}^n)}{\Delta t} \left(\frac{\partial \boldsymbol{Q}}{\partial \boldsymbol{P}} \right)^n V = \boldsymbol{\mathcal{R}}^n + \left(\frac{\partial \boldsymbol{\mathcal{R}}}{\partial \boldsymbol{P}} \right)^n \left(\boldsymbol{P}^{n+1} - \boldsymbol{P}^n \right). \tag{3.8}$$

By defining

$$\Delta \boldsymbol{P} \triangleq \boldsymbol{P}^{n+1} - \boldsymbol{P}^n, \tag{3.9}$$

and rearranging Eq. (3.8), we obtain an expression for $\Delta \boldsymbol{P}$

$$\left[\frac{V}{\Delta t} \left(\frac{\partial \boldsymbol{Q}}{\partial \boldsymbol{P}} \right)^n - \left(\frac{\partial \boldsymbol{R}}{\partial \boldsymbol{P}} \right)^n \right] \Delta \boldsymbol{P} = \boldsymbol{\mathcal{R}}^n. \tag{3.10}$$

Therefore, the primitive varaibles at time $n + 1$ are obtained by simply applying

$$\boldsymbol{P}^{n+1} = \boldsymbol{P}^n + \Delta \boldsymbol{P}. \tag{3.11}$$

In the following sections, the discretization process necessary to incorporate the governing equations in the KATS framework is carried out both for compressible solver and incompressible solver. Then, the boundary conditions, the computation of the numerical gradient for non-uniform structured grid and the domain decomposition and parallelization procesesses are described.

3.1 Discretization of compressible governing equation

In the current approach, the compressible governing equations, Eq. (2.131) to (2.135), are split into two groups, and each group is solved independently and sequentially. The first group contains the flow field equations, which are the conservation of mass, momentum and energy, respectively Eqs. (2.131), (2.132) and (2.133). The second group contains the RANS equations, which are the equation for the transport of k and ω, respectively Eq. (2.134) and (2.135). Both groups of equations can be cast under the general conservative form used by KATS, Eq.(3.1), and thus can be discretized according to Eq.(3.10).

3.1.1 Discretization of mass, momentum and energy equation

The flow field conservation equations were derived in the previous section using Favre averaging. The primitive variables like $\widetilde{u}$, $\bar{p}$, $\widetilde{T}$ are thus time-averaged values. In order to simplified the notation, the time-averaging notation is dropped, and u, p, T is used to represent $\widetilde{u}$, $\bar{p}$, $\widetilde{T}$ respectively. Also, the velocity vector u can be expressed by (u, v, w), where $u(\boldsymbol{x}, t) \in \mathbb{R}$, $v(\boldsymbol{x}, t) \in \mathbb{R}$, $w(\boldsymbol{x}, t) \in \mathbb{R}$ are the speed in the x, y, z directions of Cartesian coordinates.

For the flow-field governing equations, the vector of primitive variables $\boldsymbol{P}$, conservative variables $\boldsymbol{Q}$, source term $\boldsymbol{S}_v$, advective flux $\boldsymbol{\mathcal{F}}$, and diffusive flux $\boldsymbol{\mathcal{F}}_d$ are thus

$$\boldsymbol{P} = \begin{pmatrix} p \\ u \\ v \\ w \\ T \end{pmatrix}. \qquad \boldsymbol{Q} = \begin{pmatrix} \rho \\ \rho u \\ \rho v \\ \rho w \\ \rho \widetilde{E} \end{pmatrix}, \qquad \boldsymbol{S}_v = \begin{pmatrix} 0 \\ 0 \\ 0 \\ 0 \\ 0 \end{pmatrix},$$

$$\mathcal{F} = \begin{pmatrix} \rho u & \rho v & \rho w \\ \rho u^2 + p & \rho u v & \rho u w \\ \rho v u & \rho v^2 + p & \rho v w \\ \rho w u & \rho w v & \rho w^2 + p \\ (\rho\widetilde{E} + p)u & (\rho\widetilde{E} + p)v & (\rho\widetilde{E} + p)w \end{pmatrix},$$

$$\mathcal{F}_d = \begin{pmatrix} 0 & 0 & 0 \\ 2(\mu + \mu_t)\widetilde{\boldsymbol{S}}_{11} - \frac{2}{3}\rho k & 2(\mu + \mu_t)\widetilde{\boldsymbol{S}}_{12} & 2(\mu + \mu_t)\widetilde{\boldsymbol{S}}_{13} \\ 2(\mu + \mu_t)\widetilde{\boldsymbol{S}}_{21} & 2(\mu + \mu_t)\widetilde{\boldsymbol{S}}_{22} - \frac{2}{3}\rho k & 2(\mu + \mu_t)\widetilde{\boldsymbol{S}}_{23} \\ 2(\mu + \mu_t)\widetilde{\boldsymbol{S}}_{31} & 2(\mu + \mu_t)\widetilde{\boldsymbol{S}}_{32} & 2(\mu + \mu_t)\widetilde{\boldsymbol{S}}_{33} - \frac{2}{3}\rho k \\ \zeta_1 & \zeta_2 & \zeta_3 \end{pmatrix},$$

$$\zeta_1 = (\mu + \mu_t)(\widetilde{\boldsymbol{S}}_{11}u + \widetilde{\boldsymbol{S}}_{12}v + \widetilde{\boldsymbol{S}}_{13}w) - \frac{2}{3}\rho k u - c_p\frac{\partial T}{\partial x}\left(\frac{\mu}{\mathrm{Pr}} + \frac{\mu_t}{\mathrm{Pr}_t}\right), \qquad (3.12)$$

$$\zeta_2 = (\mu + \mu_t)(\widetilde{\boldsymbol{S}}_{21}u + \widetilde{\boldsymbol{S}}_{22}v + \widetilde{\boldsymbol{S}}_{23}w) - \frac{2}{3}\rho k v - c_p\frac{\partial T}{\partial y}\left(\frac{\mu}{\mathrm{Pr}} + \frac{\mu_t}{\mathrm{Pr}_t}\right), \qquad (3.13)$$

$$\zeta_3 = (\mu + \mu_t)(\widetilde{\boldsymbol{S}}_{31}u + \widetilde{\boldsymbol{S}}_{32}v + \widetilde{\boldsymbol{S}}_{33}w) - \frac{2}{3}\rho k w - c_p\frac{\partial T}{\partial z}\left(\frac{\mu}{\mathrm{Pr}} + \frac{\mu_t}{\mathrm{Pr}_t}\right), \qquad (3.14)$$

where

$$\widetilde{\boldsymbol{S}} = \begin{pmatrix} \widetilde{\boldsymbol{S}}_{11} & \widetilde{\boldsymbol{S}}_{12} & \widetilde{\boldsymbol{S}}_{13} \\ \widetilde{\boldsymbol{S}}_{21} & \widetilde{\boldsymbol{S}}_{22} & \widetilde{\boldsymbol{S}}_{23} \\ \widetilde{\boldsymbol{S}}_{31} & \widetilde{\boldsymbol{S}}_{32} & \widetilde{\boldsymbol{S}}_{33} \end{pmatrix} = \frac{1}{2}\begin{pmatrix} 2\frac{\partial u}{\partial x} - \frac{2}{3}\nabla \cdot \boldsymbol{u} & \frac{\partial u}{\partial y} + \frac{\partial v}{\partial x} & \frac{\partial u}{\partial z} + \frac{\partial w}{\partial x} \\ \frac{\partial v}{\partial x} + \frac{\partial u}{\partial y} & 2\frac{\partial v}{\partial y} - \frac{2}{3}\nabla \cdot \boldsymbol{u} & \frac{\partial v}{\partial z} + \frac{\partial w}{\partial y} \\ \frac{\partial w}{\partial x} + \frac{\partial u}{\partial z} & \frac{\partial w}{\partial y} + \frac{\partial v}{\partial z} & 2\frac{\partial w}{\partial z} - \frac{2}{3}\nabla \cdot \boldsymbol{u} \end{pmatrix}.$$

In the mass, momentum, and energy conservation equations, the Jacobian of the conservative variable $\boldsymbol{Q}$ with respect to primitive variable $\boldsymbol{P}$ is

$$\frac{\partial \boldsymbol{Q}}{\partial \boldsymbol{P}} = \begin{pmatrix} \dfrac{\partial \rho}{\partial p} & 0 & 0 & 0 & \dfrac{\partial \rho}{\partial T} \\ u\dfrac{\partial \rho}{\partial p} & \rho & 0 & 0 & u\dfrac{\partial \rho}{\partial T} \\ v\dfrac{\partial \rho}{\partial p} & 0 & \rho & 0 & v\dfrac{\partial \rho}{\partial T} \\ w\dfrac{\partial \rho}{\partial p} & 0 & 0 & \rho & w\dfrac{\partial \rho}{\partial T} \\ h\dfrac{\partial \rho}{\partial p} - 1 & \rho u & \rho v & \rho w & h_a\dfrac{\partial \rho}{\partial T} + \rho c_p \end{pmatrix},$$

where

$$h_a = c_p T + \frac{\boldsymbol{u} \cdot \boldsymbol{u}}{2} + k. \tag{3.15}$$

To evaluate the term $\partial \boldsymbol{\mathcal{R}}/\partial \boldsymbol{P}$ in Eq. (3.10), it is necessary to calculate $\partial(\boldsymbol{\mathcal{F}} \cdot \boldsymbol{n})/\partial \boldsymbol{P}$ and $\partial(\boldsymbol{\mathcal{F}}_d \cdot \boldsymbol{n})/\partial \boldsymbol{P}$. Advective fluxes through face $\boldsymbol{\mathcal{F}} \cdot \boldsymbol{n}$ are calculated according to the flux vector splitting method AUSM$^+$-up [100]. The Jacobian of the advective flux through the normal of the face, which are $\boldsymbol{\mathcal{F}} \cdot \boldsymbol{n}$, with respect to the component of vector $\boldsymbol{P}$ are

$$\frac{\partial(\boldsymbol{\mathcal{F}} \cdot \boldsymbol{n})}{\partial p} = \begin{pmatrix} (n_x u + n_y v + n_z w)\dfrac{\partial \rho}{\partial p} \\[6pt] n_x + (n_x u^2 + n_y uv + n_z uw)\dfrac{\partial \rho}{\partial p} \\[6pt] n_y + (n_x vu + n_y v^2 + n_z vw)\dfrac{\partial \rho}{\partial p} \\[6pt] n_z + (n_x wu + n_y wv + n_z w^2)\dfrac{\partial \rho}{\partial p} \\[6pt] (n_x uH + n_y vH + n_z wH)\dfrac{\partial \rho}{\partial p} \end{pmatrix}.$$

$$\frac{\partial(\boldsymbol{\mathcal{F}} \cdot \boldsymbol{n})}{\partial u} = \begin{pmatrix} \rho n_x \\[6pt] 2\rho u n_x + \rho v n_y + \rho w n_z \\[6pt] \rho v n_x \\[6pt] \rho w n_x \\[6pt] (\rho h + \rho uu)n_x + \rho uv n_y + \rho uw n_z \end{pmatrix}.$$

$$\frac{\partial(\boldsymbol{\mathcal{F}} \cdot \boldsymbol{n})}{\partial v} = \begin{pmatrix} \rho n_y \\[6pt] \rho u n_y \\[6pt] \rho u n_x + 2\rho v n_y + \rho w n_y \\[6pt] \rho w n_y \\[6pt] \rho vu n_x + (\rho h + \rho vv)n_y + \rho vw n_y \end{pmatrix}.$$

$$\frac{\partial(\boldsymbol{\mathcal{F}} \cdot \boldsymbol{n})}{\partial w} = \begin{pmatrix} \rho n_z \\ \rho u n_z \\ \rho v n_z \\ \rho u n_x + \rho v n_y + 2\rho w n_z \\ \rho w u n_x + \rho w v n_y + (\rho h + \rho w w) n_z \end{pmatrix}.$$

$$\frac{\partial(\boldsymbol{\mathcal{F}} \cdot \boldsymbol{n})}{\partial T} = \begin{pmatrix} (n_x u + n_y v + n_z w)\frac{\partial \rho}{\partial T} \\ (n_x u^2 + n_y uv + n_z uw)\frac{\partial \rho}{\partial T} \\ (n_x vu + n_y v^2 + n_z vw)\frac{\partial \rho}{\partial T} \\ (n_x wu + n_y wv + n_z w^2)\frac{\partial \rho}{\partial T} \\ (n_x u + n_y v + n_z w)c_p\frac{\partial \rho}{\partial T} \end{pmatrix}.$$

The diffusive flux are simpler to evaluate since they are not subjected to a flux splitting methodology. This is achieve by using a system of coordinates based on the face-normal direction $\boldsymbol{n}$, and the tangential face directions $\boldsymbol{l} = (l_x, l_y, l_z)$ and $\boldsymbol{m} = (m_x, m_y, m_z)$, which redefines the velocity vector as (u_n, u_l, u_m). The diffusive flux in the face-normal direction using the new coordinates becomes

$$\boldsymbol{F}_{dn} \triangleq \boldsymbol{\mathcal{F}}_d \cdot \boldsymbol{n} = \begin{pmatrix} 0 \\ (\mu + \mu_t)\frac{4}{3}\frac{\partial u_n}{\partial n} \\ (\mu + \mu_t)\frac{\partial u_l}{\partial n} \\ (\mu + \mu_t)\frac{\partial u_m}{\partial n} \\ (\mu + \mu_t)(\frac{4}{3}\frac{\partial u_n}{\partial n}u_n + \frac{\partial u_l}{\partial n}u_l + \frac{\partial u_m}{\partial n}u_m) - c_p\frac{\partial T}{\partial n}(\frac{\mu}{Pr} + \frac{\mu_t}{Pr_t}) \end{pmatrix}.$$

In this expression the turbulent kinetic energy and the tangential direction derivatives are neglected. This expresion can be further simplified by defining a property matrix

$\boldsymbol{M}$ and the variable vector $\boldsymbol{V}_n$

$$\boldsymbol{M} = \begin{pmatrix} 0 & 0 & 0 & 0 & 0 \\ 0 & \frac{4}{3}(\mu + \mu_t) & 0 & 0 & 0 \\ 0 & 0 & (\mu + \mu_t) & 0 & 0 \\ 0 & 0 & 0 & (\mu + \mu_t) & 0 \\ 0 & \frac{4}{3}(\mu + \mu_t)u & (\mu + \mu_t)v & (\mu + \mu_t)w & c_p(\frac{\mu}{Pr} + \frac{\mu_t}{Pr_t}) \end{pmatrix},$$

$$\boldsymbol{V}_n = \begin{pmatrix} \rho \\ u_n \\ u_l \\ u_m \\ T \end{pmatrix},$$

which leads to the the following expression for the normal diffusive flux

$$\boldsymbol{F}_{dn} = \boldsymbol{M}\frac{\partial \boldsymbol{V}_n}{\partial n} = \boldsymbol{M}\frac{\boldsymbol{V}_{nR} - \boldsymbol{V}_{nL}}{\Delta n}, \tag{3.16}$$

where $\boldsymbol{V}_{nR}$ and $\boldsymbol{V}_{nL}$ represent transport properties on right and left side of the face, and Δn is the normal distance. A rotation matrix $\boldsymbol{R}_x$ can be used to map the original coordinates to face-normal coordinates, defined as

$$\boldsymbol{R}_{xn} = \begin{pmatrix} 1 & 0 & 0 & 0 & 0 \\ 0 & n_x & n_y & n_z & 0 \\ 0 & l_x & l_y & l_z & 0 \\ 0 & m_x & m_y & m_z & 0 \\ 0 & 0 & 0 & 0 & 1 \end{pmatrix}, \boldsymbol{R}_{xn}^{-1} = \begin{pmatrix} 1 & 0 & 0 & 0 & 0 \\ 0 & n_x & l_x & m_x & 0 \\ 0 & n_y & l_y & m_y & 0 \\ 0 & n_z & l_z & m_z & 0 \\ 0 & 0 & 0 & 0 & 1 \end{pmatrix}.$$

Therefore, the face-normal diffusive fluxes becomes

$$\boldsymbol{F}_{dn} = \frac{\boldsymbol{M}}{\Delta n}\boldsymbol{R}_{xn}(\boldsymbol{V}_R - \boldsymbol{V}_L) = \frac{\boldsymbol{M}}{\Delta n}\boldsymbol{R}_{xn}\frac{\partial \boldsymbol{V}}{\partial \boldsymbol{P}}(\boldsymbol{P}_R - \boldsymbol{P}_L), \tag{3.17}$$

where $\boldsymbol{P}_R$ and $\boldsymbol{P}_L$ represents the primitive variable vectors on the right and left side of the face, $\boldsymbol{V}$ is vector $\boldsymbol{V}_n$ rotated back into the original coordinates system

$$
\boldsymbol{V} = \begin{pmatrix} \rho \\ u \\ v \\ w \\ T \end{pmatrix}.
$$

Therefore, $\partial \boldsymbol{V}/\partial \boldsymbol{P}$ is defined as

$$
\frac{\partial \boldsymbol{V}}{\partial \boldsymbol{P}} = \begin{pmatrix} \frac{\partial \rho}{\partial p} & 0 & 0 & 0 & \frac{\partial \rho}{\partial T} \\ 0 & 1 & 0 & 0 & 0 \\ 0 & 0 & 1 & 0 & 0 \\ 0 & 0 & 0 & 1 & 0 \\ 0 & 0 & 0 & 0 & 1 \end{pmatrix},
$$

and $\boldsymbol{\mathcal{F}}_d$ becomes

$$
\boldsymbol{\mathcal{F}}_d = \boldsymbol{R}_{xn}^{-1} \boldsymbol{F}_{dn} = \boldsymbol{R}_{xn}^{-1} \frac{\boldsymbol{M}}{\Delta n} \boldsymbol{R}_{xn} \frac{\partial \boldsymbol{V}}{\partial \boldsymbol{P}} (\boldsymbol{P}_R - \boldsymbol{P}_L), \tag{3.18}
$$

The Jacobian matrix of diffusive flux also need to be defined

$$
\frac{\partial \boldsymbol{\mathcal{F}}_d}{\partial \boldsymbol{P}_R} = \boldsymbol{R}_{xn}^{-1} \frac{\boldsymbol{M}}{\Delta n} \boldsymbol{R}_{xn} \frac{\partial \boldsymbol{V}}{\partial \boldsymbol{P}}, \tag{3.19}
$$

$$
\frac{\partial \boldsymbol{\mathcal{F}}_d}{\partial \boldsymbol{P}_L} = -\boldsymbol{R}_{xn}^{-1} \frac{\boldsymbol{M}}{\Delta n} \boldsymbol{R}_{xn} \frac{\partial \boldsymbol{V}}{\partial \boldsymbol{P}}. \tag{3.20}
$$

Including all of these definition, Eq. (3.10) can be rewritten as

$$
\left(\frac{V}{\Delta t} \frac{\partial \boldsymbol{Q}}{\partial \boldsymbol{P}} - \sum_{\text{face}} \left(\frac{\partial \boldsymbol{\mathcal{F}}_d}{\partial \boldsymbol{P}_R} K - \frac{\partial \boldsymbol{\mathcal{F}}_d}{\partial \boldsymbol{P}_L} K \right) + \sum_{\text{face}} \frac{\partial (\boldsymbol{\mathcal{F}} \cdot \boldsymbol{n})}{\partial \boldsymbol{P}} A - \frac{\partial \boldsymbol{S}_v}{\partial \boldsymbol{P}} V \right) \triangle \boldsymbol{P} = \boldsymbol{R}^{n+1}, \tag{3.21}
$$

where

$$
K = \frac{A(\boldsymbol{n} \cdot \boldsymbol{l}_r)}{\|\boldsymbol{l}_r\|^2}, \tag{3.22}
$$

$\boldsymbol{l}_r$ is vector from left cell center to right cell center. In this expression, K represen the projection of face area A along $\boldsymbol{l}_r$.

3.1.2 Discretization of k-ω equation

The k-ω equations can also be cast under a conservative form. The conservative vector, flux matrices and source term vector are Eq. (3.1).

$$\boldsymbol{Q} = \begin{pmatrix} \rho k \\ \rho \omega \end{pmatrix},$$

$$\boldsymbol{\mathcal{F}} = \begin{pmatrix} \rho k u & \rho k v & \rho k w \\ \rho \omega u & \rho \omega v & \rho \omega w \end{pmatrix},$$

$$\boldsymbol{\mathcal{F}}_d = \begin{pmatrix} (\mu + \mu_t \sigma_k)\frac{\partial k}{\partial x} & (\mu + \mu_t \sigma_k)\frac{\partial k}{\partial y} & (\mu + \mu_t \sigma_k)\frac{\partial k}{\partial z} \\ (\mu + \mu_t \sigma_\omega)\frac{\partial \omega}{\partial x} & (\mu + \mu_t \sigma_\omega)\frac{\partial \omega}{\partial y} & (\mu + \mu_t \sigma_\omega)\frac{\partial \omega}{\partial z} \end{pmatrix},$$

$$\boldsymbol{S}_v = \begin{pmatrix} P_k - D_k \\ P_\omega - D_\omega \end{pmatrix}.$$

For this system of equations, the vector of primitive variables $\boldsymbol{P}$ is

$$\boldsymbol{P} = \begin{pmatrix} k \\ \omega \end{pmatrix}.$$

The iterative form of k-ω follow the same form as Eq. (3.21). For convenience, it is shown again here

$$\left(\frac{V}{\triangle t}\frac{\partial \boldsymbol{Q}}{\partial \boldsymbol{P}} - \sum_{\text{face}}(\frac{\partial \boldsymbol{\mathcal{F}}_d}{\partial \boldsymbol{P}_R}K - \frac{\partial \boldsymbol{\mathcal{F}}_d}{\partial \boldsymbol{P}_L}K) + \sum_{\text{face}} \frac{\partial(\boldsymbol{\mathcal{F}} \cdot \boldsymbol{n})}{\partial \boldsymbol{P}}A - \frac{\partial \boldsymbol{S}_v}{\partial \boldsymbol{P}}V \right)\triangle \boldsymbol{P} = \boldsymbol{R}^n, \quad (3.23)$$

where

$$\frac{\partial \boldsymbol{Q}}{\partial \boldsymbol{P}} = \begin{pmatrix} \rho & 0 \\ 0 & \rho \end{pmatrix}, \qquad \frac{\partial(\boldsymbol{\mathcal{F}} \cdot \boldsymbol{n})}{\partial \boldsymbol{P}} = \begin{pmatrix} \rho(un_x + vn_y + wn_z) & 0 \\ 0 & \rho(un_x + vn_y + wn_z) \end{pmatrix},$$

$$\frac{\partial \boldsymbol{\mathcal{F}}_d}{\partial \boldsymbol{P}_R} = \begin{pmatrix} \frac{(\mu+\mu_t)\sigma_k}{\triangle n} & 0 \\ 0 & \frac{(\mu+\mu_t)\sigma_\omega}{\triangle n} \end{pmatrix}, \qquad \frac{\partial \boldsymbol{\mathcal{F}}_d}{\partial \boldsymbol{P}_L} = -\begin{pmatrix} \frac{(\mu+\mu_t)\sigma_k}{\triangle n} & 0 \\ 0 & \frac{(\mu+\mu_t)\sigma_\omega}{\triangle n} \end{pmatrix},$$

$$\frac{\partial \boldsymbol{S}_v}{\partial \boldsymbol{P}} = \begin{pmatrix} -\beta^* \rho \omega - \frac{2}{3}(\nabla \cdot \rho \boldsymbol{u}) & -\beta^* \rho k \\ -\frac{\alpha \rho}{\mu_t}(\frac{2}{3}\nabla \cdot \rho \boldsymbol{u}) & -2\beta \rho \omega \end{pmatrix}.$$

3.2 Discretization of incompressible governing equation

Numerically, pressure cannot be calculated directly from governing equations above. In order to couple the pressure and velocity in the momentum equation, a class of Navier-Stokes equation solution procedures – the projection method [101, 102] is implemented. The projection method is based on Helmholtz decomposition [103]. In particular, here we use the finite volume projection method [104] which is based on Gresho projection-1 method [105]. Although the second-order projection method of [106] for the incompressible flow was also investigated. It solves the governing equation in two steps [107]. First, the momentum equation without pressure is solved, and an intermediate velocity field is obtained. Then the pressure field is calculated with the intermediate velocity and is used to correct the intermediate velocity to satisfy the divergence free condition. In order to efficiently solve the incompressible Reynolds-averaged Navier-Stokes equation, the divergence-free condition, Eq. (2.82), is not solved simultaneously with the other equations but is enforced by using a finite volume projection [101] based on the Gresho projection-1 method [105]. For convenience, the Reynodls-averaging notation, as shown in Eq. (2.82) and (2.83) is dropped, and $\boldsymbol{u}$, p is used to represent $\bar{\boldsymbol{u}}$, $\bar{p}$ respectively. Also, the velocity vector $\boldsymbol{u}$ can be expressed by (u, v, w), where $u(\boldsymbol{x}, t) \in \mathbb{R}$, $v(\boldsymbol{x}, t) \in \mathbb{R}$, $w(\boldsymbol{x}, t) \in \mathbb{R}$ are the speed in the x, y, z directions of Cartesian coordinates. Eq. (2.83), is thus re-cast as two equations that are solved sequentially: the pressure-less momentum transport equation, Eq. (3.24), and the pressure Poisson equation, Eq. (3.25). Therefore, the real equations solved are

$$\frac{\boldsymbol{u}^* - \boldsymbol{u}^n}{\Delta t} = -\nabla \cdot (\boldsymbol{u}^n \boldsymbol{u}^n) + \nabla \cdot (\boldsymbol{\tau} + \boldsymbol{R}), \tag{3.24}$$

$$\nabla p^* = \frac{\rho(\boldsymbol{u}^* - \boldsymbol{u}^{n+1})}{\Delta t}. \tag{3.25}$$

$$\boldsymbol{u}^{n+1} = \boldsymbol{u}^* - \Delta t \nabla p, \tag{3.26}$$

$$\frac{\partial k}{\partial t} + \nabla \cdot (k \boldsymbol{u}^{n+1}) = \nabla \cdot ((\nu + \nu_t \sigma_k) \nabla k) + \frac{S_k}{\rho}, \tag{3.27}$$

41

$$\frac{\partial \omega}{\partial t} + \nabla \cdot (\omega \boldsymbol{u}^{n+1}) = \nabla \cdot ((\nu + \nu_t \sigma_\omega) \nabla \omega) + \frac{S_\omega}{\rho}, \tag{3.28}$$

$$\nu_t = \frac{k}{\omega}, \tag{3.29}$$

In these equations, $\boldsymbol{u}^n$ and $\boldsymbol{u}^{n+1}$ are the velocity vector at time step n and $n+1$, respectively; $\boldsymbol{u}^*$ is the intermediate velocity vector before projecting to the divergence-free field; Δt is time step; and p^* is the pseudo-pressure, which has order of Δt error relative to the actual pressure.

The momentum transport and the closure equations can take the form of Eq. (3.1) and can solve simultaneously. Thus, Eq. (3.24), Eq. (2.134), and Eq. (2.135) can be re-arrange

$$\boldsymbol{P} = \begin{pmatrix} u \\ v \\ w \\ k \\ \omega \end{pmatrix}, \qquad \boldsymbol{S} = \begin{pmatrix} 0 \\ 0 \\ 0 \\ \boldsymbol{R} \cdot \nabla \boldsymbol{u} - \beta^* \omega k \\ \alpha \frac{\omega}{k} \boldsymbol{R} \cdot \nabla \boldsymbol{u} - \beta \omega^2 \end{pmatrix}, \tag{3.30}$$

$$\boldsymbol{\mathcal{F}} = \begin{pmatrix} u^2 & vu & wu \\ uv & v^2 & wv \\ uw & vw & w^2 \\ ku & kv & kw \\ \omega u & \omega v & \omega w \end{pmatrix}, \qquad \boldsymbol{\mathcal{F}}_d = \begin{pmatrix} \boldsymbol{R} + \boldsymbol{\tau} \\ \\ (\nu + \nu_t \sigma_k) \nabla k \\ (\nu + \nu_t \sigma_\omega) \nabla \omega \end{pmatrix}. \tag{3.31}$$

This system of equation is thus discretized using Eq. (3.21), and solved according to the numerical procedure described earlier.

The pressure Poisson equation, Eq. (3.25), cannot be cast in the form of Eq. (3.10), and therefore must be solved independently. This is achieved by taking the divergence of Eq. (3.25) and applying the divergence free condition, Eq. (2.82), on the velocity field to obtain:

$$\nabla \cdot \nabla p = \frac{\rho \nabla \cdot \boldsymbol{u}^*}{\Delta t}. \tag{3.32}$$

By integrating Eq. (3.32) over volume V, we obtain

$$\int_V \nabla \cdot \nabla p \mathrm{d}V = \int_V \frac{\rho \nabla \cdot \boldsymbol{u}^*}{\Delta t} \mathrm{d}V \tag{3.33}$$

$$\oint \nabla p \cdot \boldsymbol{n} \mathrm{d}A = \frac{\rho \nabla \cdot \boldsymbol{u}^*}{\Delta t} V_{\mathrm{cell}} \tag{3.34}$$

Numerically, this equation can be represented as a summation over all faces of the discrete cell volume V_{cell}:

$$\sum_{j \in \text{ face}} \frac{p_l - p_r}{\|\boldsymbol{l}_r\|^2} \boldsymbol{l}_r \cdot \boldsymbol{n}_j \, A_j = \frac{\rho \nabla \cdot \boldsymbol{u}^*}{\Delta t} V_{\mathrm{cell}} , \tag{3.35}$$

where $\boldsymbol{l}_r$ is the vector from the left cell center to the right cell center of face A_j. Applying this to the mesh stencil, this becomes a linear system of equations that can be solved for p everywhere. A biconjugate gradient method is used to solve this sparse system of linear equations, using a Neuman condition for inlet, symmetry and wall boundaries, and a Dirichlet condition for outlet boundaries.

3.3   Numerical gradient for non-uniform structured the grid

In order to solve the governing equations, the finite volume method for non-uniform structured grids is applied. Calculating the gradient for such a grid is not necessarily trivial. In order to illustrate the method used in KATS, the two-dimensional example shown in Fig. 3.1 is used.   rotation matrix x-direction term of gradient vector y-direction term of gradient vector z-direction term of gradient vector   n-direction term of gradient vector   l-direction term of gradient vector   m-direction term of gradient vector

As an example, the gradient of an arbitrary quantity ξ is used

$$\boldsymbol{G} = \nabla \xi.$$

Therefore, the gradient at cell 0 is calculated using neighbor cells 1 through 4. The component calculated from cell 1 and cell 2 is in the $\boldsymbol{n} = (n_x, n_y, n_z)$ direction, and the
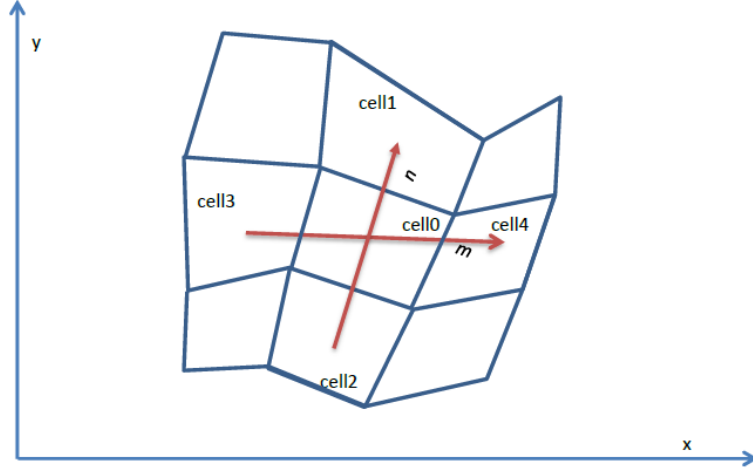
Figure 3.1: 2-D example of gradient calculation

one from cell 3 and cell 4 is in the $\boldsymbol{m} = (m_x, m_y, m_z)$ direction. In three-dimensional space, there would be an additional direction $\boldsymbol{l} = (l_x, l_y, l_z)$.

A rotation matrix $\boldsymbol{R}_G$ is needed to transform the gradient (G_n, G_ℓ, G_m) expressed using the cells (e.i. in the nml directions) in the gradient (G_x, G_y, G_z) aligned with the reference axis

$$
\boldsymbol{R}_G = \begin{pmatrix} n_x & n_y & n_z \\ l_x & l_y & l_z \\ m_x & m_y & m_z \end{pmatrix}.
$$

This leads to the following relation

$$
\boldsymbol{R}_G \begin{pmatrix} G_x \\ G_y \\ G_z \end{pmatrix} = \begin{pmatrix} n_x & n_y & n_z \\ l_x & l_y & l_z \\ m_x & m_y & m_z \end{pmatrix} \begin{pmatrix} G_x \\ G_y \\ G_z \end{pmatrix} = \begin{pmatrix} G_n \\ G_l \\ G_m \end{pmatrix}.
$$

Therefore the gradient (G_n, G_l, G_m) can easily be calculated from each pair of neighbor cells. As an example, the explicit gradient of quantity ξ would be

$$
\begin{pmatrix} G_x \\ G_y \\ G_z \end{pmatrix} = \boldsymbol{R}_G^{-1} \begin{pmatrix} G_n \\ G_l \\ G_m \end{pmatrix} = \boldsymbol{R}_G^{-1} \begin{pmatrix} \frac{\xi_1 - \xi_2}{|x_1| - |x_2|} \\ \frac{\xi_5 - \xi_6}{|x_5| - |x_6|} \\ \frac{\xi_3 - \xi_4}{|x_3| - |x_4|} \end{pmatrix}.
$$

44

3.4 Boundary conditions

In order to simplify the boundary settings, ghost cells, which are the mirror image points of the cells on the other side of the boundary, are created. At every time step, the value in the ghost cells should be updated according to the boundary type. ratio of specific heats total pressure (Pa) total temperature (K)

For an inlet boundary, the simplest condition is to impose the total pressure p_t and total temperature T_t. The pressure and temperature is therefore calculated as

$$T = T_t - \frac{(\gamma - 1)}{\gamma \mathcal{R}} \frac{(u^2 + v^2 + w^2)}{2}, \tag{3.36}$$

$$p = \frac{p_t}{(1 + \frac{u^2 + v^2 + w^2}{2\mathcal{R}T})}, \tag{3.37}$$

where γ is the ratio of specific heats, and $\mathcal{R}$ is the specific gas constant. This condition is much preferred to, say, a constant inlet velocity. This type of boundary condition causes stability issues since, at the corner of the inlet, where a non-slip wall boundary should be present, the velocity on the solid wall becomes non-zero and generates a non-physical solution. This, in turns, will decrease the density and influence the whole flow field. If a velocity inlet condition is needed, there exist two primary methods to avoid the non-physical conditions added. The first involves adding a small length, extending the inlet boundary with symmetry boundary. The second use a physical velocity profile, which means velocity decreases gradually until it is zero on the solid wall.

For the outlet boundary, all ghost cell variables are set equal to the value of boundary cell. For a symmetry boundary condition, the velocity vector is set as being symmetric. This leads to the sum of normal components of both side of the boundary to be zero, and the component parallel to the boundary face, equal on both sides. This ensures flow rate across the surface is zero.

turbulent intensity distance from point to wall wall roughness shear velocity shear stress non-dimensional roughness maximum bound of ω

In order to the solve k-ω equation, values for the turbulent intensity I_t and turbulent viscosity μ_t are needed [108]. This allows to directly compute k and ω at the boundary, and set them in the inlet ghost cells, using

$$k = \frac{3}{2}I_t^2(u^2 + v^2 + w^2),\qquad(3.38)$$

$$\omega = \frac{\rho k}{\mu_t}.\qquad(3.39)$$

At the outlet and symmetry boundary, k and ω in the ghost cells are set equal to value at the boundary cells. At the non-slip solid wall, the turbulent kinetic energy is suppressed [109] which means k is equal to 0. Since the distance of nearest cell to the wall is different for every simulation, specific dissipation rate ω is set based on distance Δy from the nearest cell center to the wall. For smooth wall, if the nearest cell is in log layer, which means the non-dimensional distance $\Delta y^+ > 30$, specific dissipation rate is calculated according to

$$\omega_{log} = \frac{u_\tau}{\kappa\sqrt{\beta^*}\Delta y}\qquad \Delta y^+ > 30,\qquad(3.40)$$

where κ is von Karman constant, equal to 0.41. If the nearest cell is in viscous layer, which means the non-dimensional distance $\Delta y^+ \leq 5$, the specific dissipation rate is calculated as

$$\omega_{vis} = \frac{6\mu}{\rho\beta\Delta y^2}.\qquad(3.41)$$

If the nearest cell is in buffer layer, which means the non-dimensional distance $5 < \Delta y^+ < 30$, specific dissipation rate is calculated by blending specific dissipation rate of the viscous layer and log layer.

$$\omega_{buf} = \sqrt{\omega_{vis}^2 + \omega_{log}^2}\qquad 5 < \Delta y^+ \leq 30.\qquad(3.42)$$

For non-smooth wall with a roughness height $\triangle h$, specific dissipation at the wall can be calculated from

$$\omega = \frac{u_\tau^2}{\ } S_R,$$ (3.43)

where

$$S_R = \left(\frac{50}{k_R}\right)^2 \qquad k_R < 25,$$ (3.44)

$$S_R = \frac{100}{k_R} \qquad k_R \geq 25,$$ (3.45)

$$k_R = max(1.0, \frac{u_\tau \triangle h}{\nu}),$$ (3.46)

$$u_\tau = \sqrt{\frac{\tau_w}{\rho}}.$$ (3.47)

u_τ is shear velocity, τ_w is shear stress, k_R is the non-dimensional roughness. The k_r parameter needs to be bounded since, at the beginning of the calculation, the friction velocity u_τ is inaccurate and likely too big.

3.5   Domain decomposition and parallelization

Use of multiple processors can greatly increase calculation speed. KATS uses domain decomposition (ParMETIS [95]) to split domains into several smaller ones. Then, the sub-domains use OpenMPI [96] to communicate together.

For each new boundary created by the partitioning scheme, ghost cells are created at each boundary cell. These ghost cells hold the information of the neighboring cell they would have if the domain was treated as a whole. After each time step, MPI threads exchanges primitive in the ghost cells are updated using their corresponding cells from the other domain. In order to illustrate this process, a simple two-dimensional domain is used, as shown in Fig. 3.2.
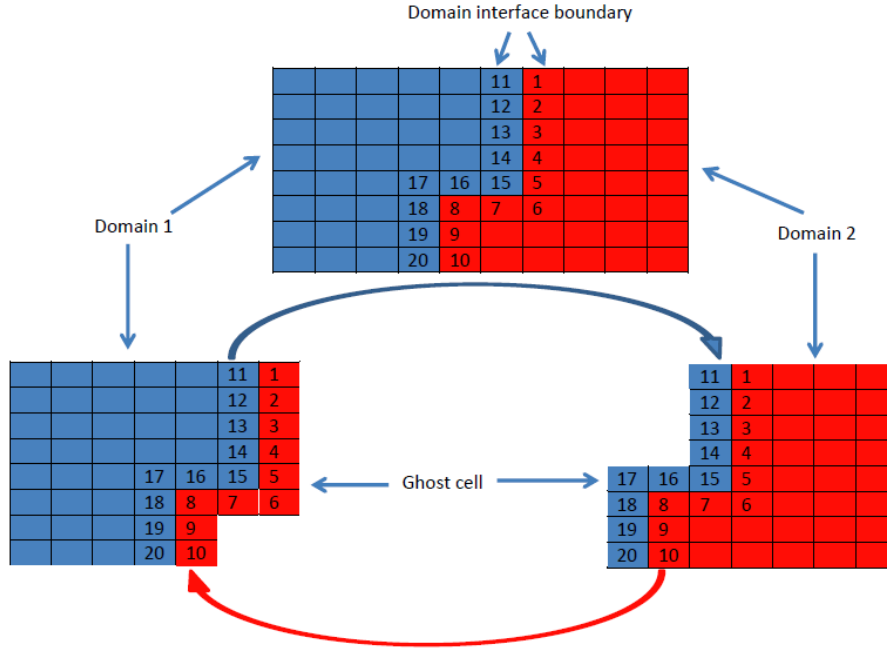
Figure 3.2: Domain decomposition at 2-D.

3.6 Verification and validation of KATS solver

3.6.1 Compressible solver verification – pipe flow

A code to code comparison was performed to verify the numerical implementation. The commercial code ANSYS Fluent was used for comparison as it has a k-ω model implemented. To conduct the verification, the same case are used for both KATS and Fluent. A pipe flow was selected as an initial verification test using the quarter pipe mesh shown in Fig. 3.3.

The pipe diameter was 0.022 m and pipe length was 20 times the diameter. The distance of first node to the wall was 1×10^{-6}m. The stagnation pressure at the inlet boundary was $103,000$ Pa, the static pressure at the outlet boundary was $101,325$ Pa, and temperature was 288 K everywhere. The value of the parameters used for the k-ω model are listed in Table(3.6.1).

The results of the axial velocity in the radial direction for both codes are presented
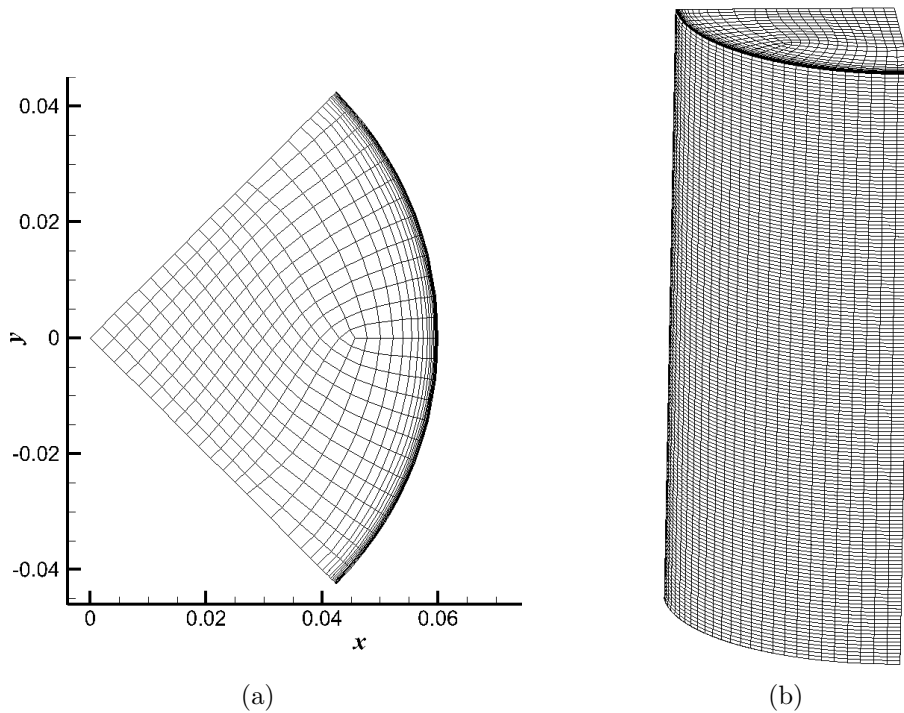
Figure 3.3: Computational mesh used for the pipe-flow verification.

Table 3.1: Parameter settings of Fluent and KATS

σ_k	σ_ω	β	β^*	α	Transitional	Shear corrections
0.5	0.5	0.072	0.09	0.52	false	false

in Fig. 3.4. The results are identical, indicating that the k-ω model was successfully implemented in KATS.

3.6.2 Compressible solver validation – backward-facing step

Following the code-to-code verification, a validation test-case was performed using the compressible k-ω model. The geometry chosen is the 2D backward-facing step, a benchmark case from the Turbulence Model Benchmarking Working Group. The experimental data was obtained in Ref. [2, 3], and can be downloaded from a NASA Turbulence Modelling Resources website[110]. In the experiment, the reference Mach number was 0.128, and the reference temperature 298.33 K. Using the step height as

(a) Linear scale   (b) Semi-logarithmic scale
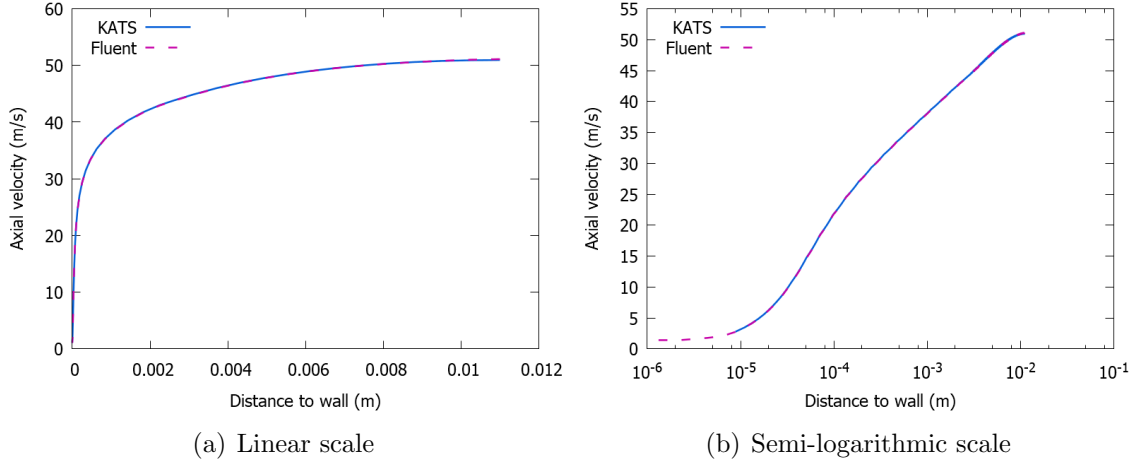
Figure 3.4: Axial velocity profile along the radius of the pipe using the k-ω model with Re=72,000

the reference length, the Reynolds number of the experiment was $36,000$.

In the KATS simulation, the step height h was fixed at 0.01 m, and the at 298.33 K. In order to match the reference Mach number, the reference velocity was set to $U_{\text{ref}} = 43$ m/s. Total pressure at the inlet boundary was set to $p_t = 102,325$ Pa, the total temperature at $T_t = 299.3109$ K, and the static pressure at outlet boundary was set to $p = 101,325$ Pa. The grid of the backward facing step case show as Fig. 3.5. Five different grids are provided by the Turbulence Model Benchmarking Working Group, with the finest grid at $1,282,500$ cells. The grid used here had $19,968$ cells. Zone 1 has 65×65 cells, zone 2 has 25×65 cells, zone 3 has 97×113 cells, zone 4 has 33×113 cells.

The results of the simulation are shown in Fig. 3.6 to 3.10. Fig. 3.6 shows the mean stream-wise velocity profile non-dimensional profile along the vertical line at x equal to -4h. Fig. 3.7 shows the velocity profile at x equal to h. The flow separates from the backward step and forms a recirculation region. There is 4.5% error between the measurements and simulation results. These results demonstrate prove that the k-ω model works well. To improve the accuracy of the simulation, the

50

k-ω closure coefficients, $\boldsymbol{\theta}$, can be further adjusted through trial and error. However which direction to adjust the parameters to make the simulation more accurate is a challenge. If there is an automated way to adjust the parameters, it will help us to obtain more accurate flow field. The next chapter will present an adaptive way approach adjust the closure coefficients of k-ω model and improve agreement with known measurements.
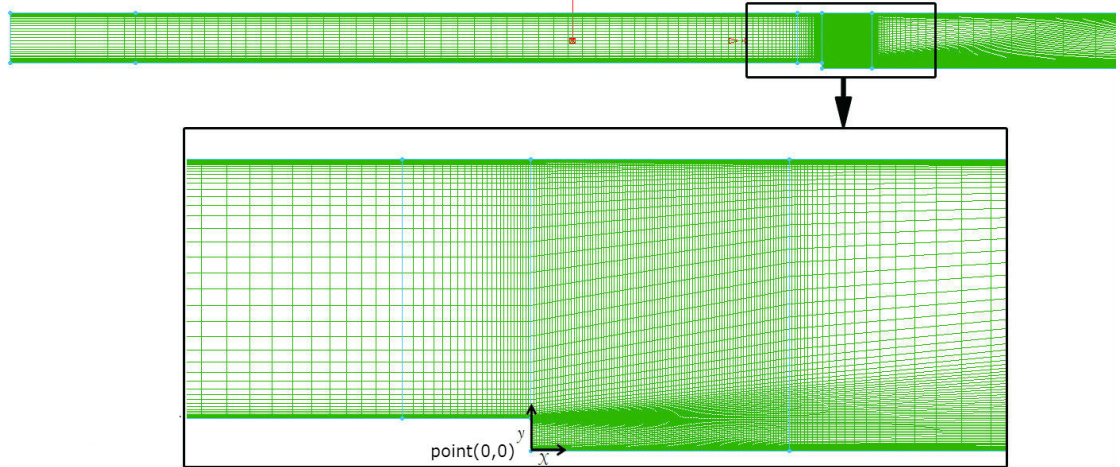
Figure 3.5: Computational mesh of the backward-facing step case.

(a) Dimensional values

(b) Dimensionless values
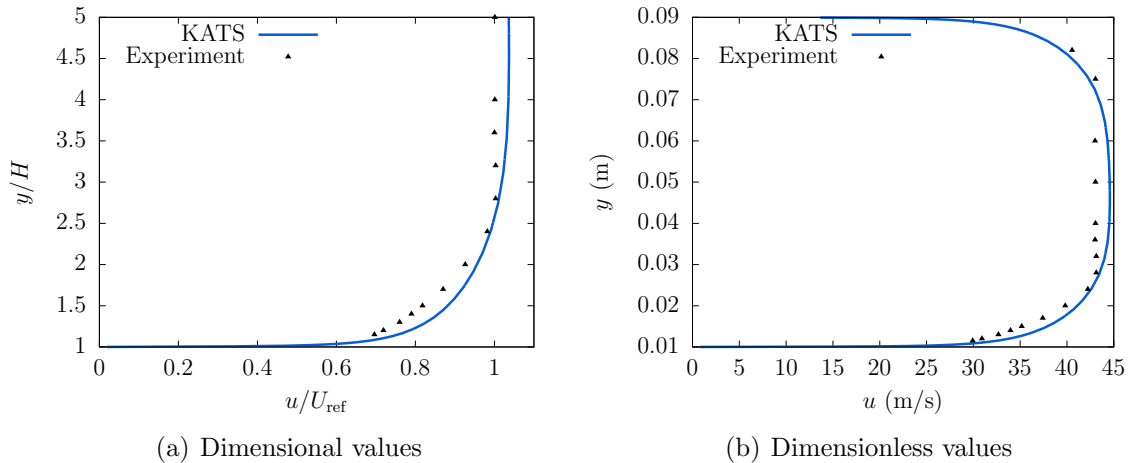
Figure 3.6: Velocity of backward-facing step case in the x-direction at x/h=-4 for KATS compressible solver validation

(a) Dimensional values   (b) Dimensionless values
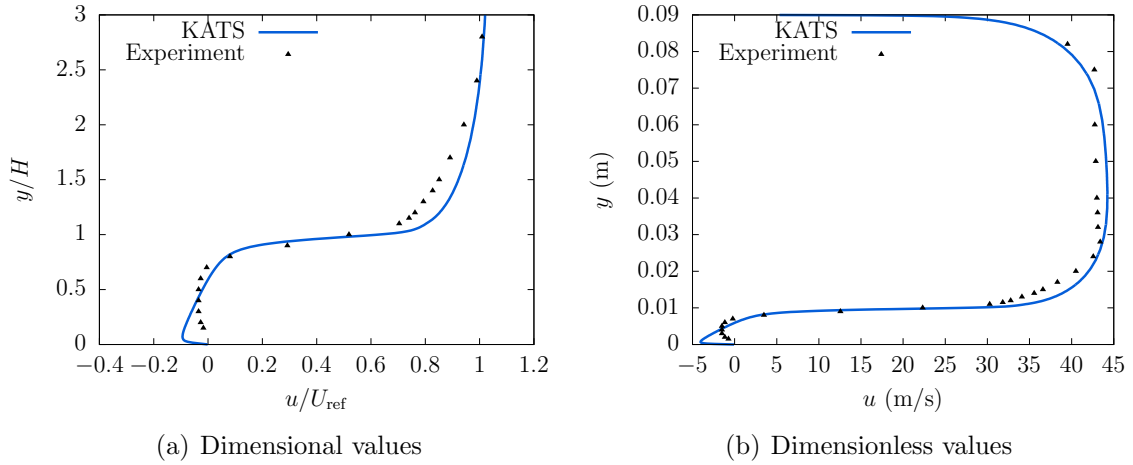
Figure 3.7: Velocity of backward-facing step case in the x-direction at $x/h{=}1$ for KATS compressible solver validation

(a) Dimensional values   (b) Dimensionless values
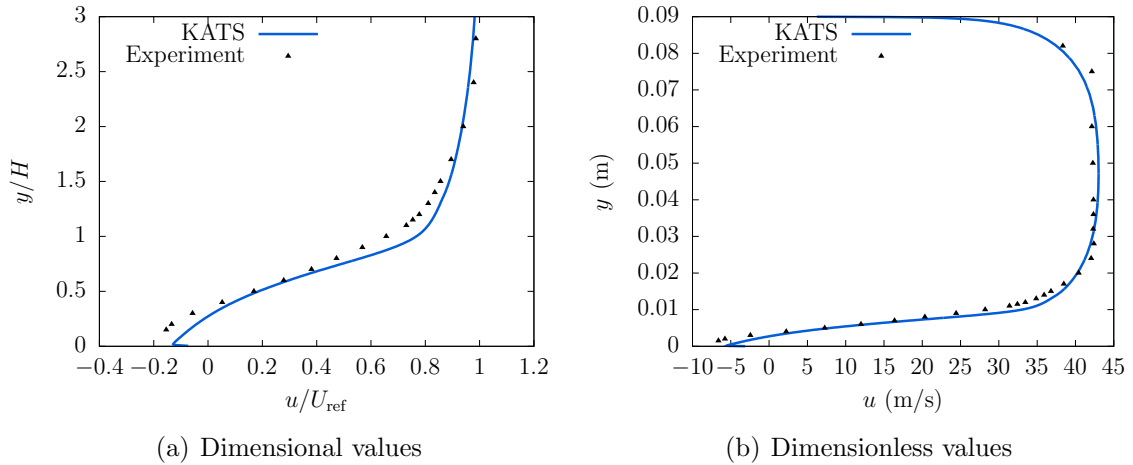
Figure 3.8: Velocity of backward-facing step case in the x-direction at $x/h{=}4$ for KATS compressible solver validation

3.6.3 Incompressible solver validation – pipe flow

The incompressible solver was also validated using the same pipe-flow test case as the one used for the compressible solver (see Fig. 3.3). Although the mesh used was the same, the pipe radius was scaled to 0.06 m and pipe length was 20 times the diameter. This also changed the the distance of the first node from the wall, which

(a) Dimensional values

(b) Dimensionless values
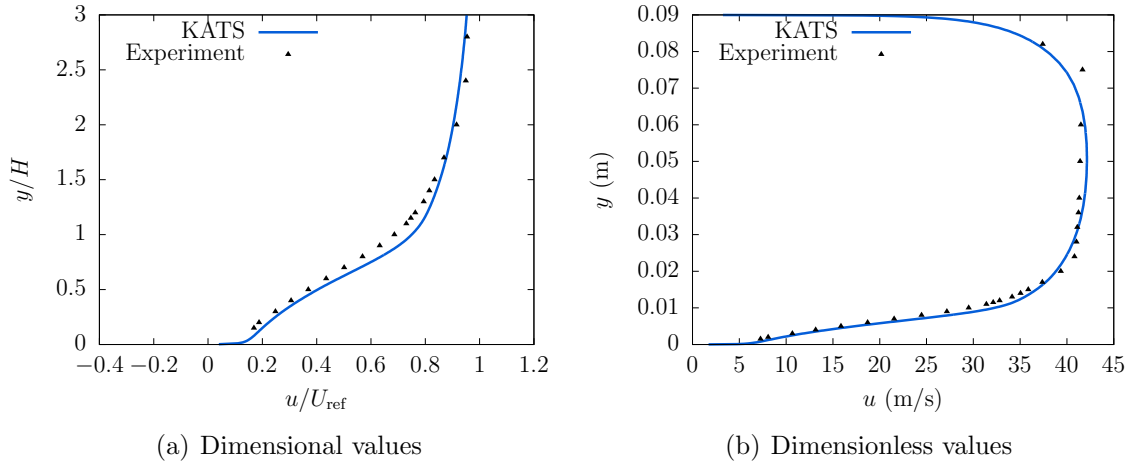
Figure 3.9: Velocity of backward-facing step case in the x-direction at x/h=6 for KATS compressible solver validation

(a) Dimensional values

(b) Dimensionless values
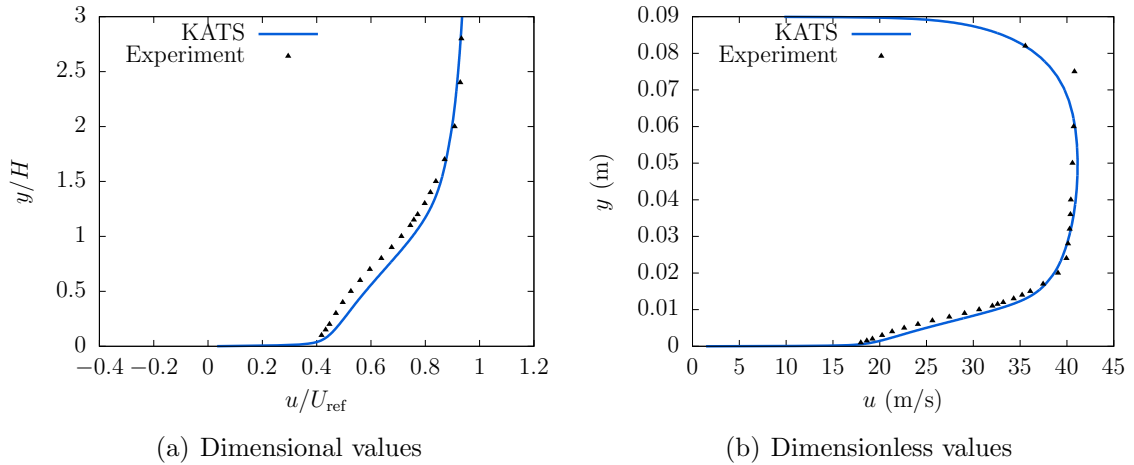
Figure 3.10: Velocity of backward-facing step case in the x-direction at x/h=10 for KATS compressible solver validation

ended being 5.45×10^{-6}m. The velocity at the inlet boundary was set at 9.1 m/s, and the parameters used for the k-ω model are listed in Table(3.6.3).

Table 3.2: Parameter settings of Fluent and KATS

σ_k	σ_ω	β	β^*	α	Transitional	Shear corrections
0.5	0.5	0.072	0.09	0.52	false	false

The experiment results used to compare the numerical results were taken from Ref. [1]. These consists of 42 measured points along the radius R at a location where the pipe flow is considered to be fully developed. The numerical velocity profile in the radial direction r is compared with experimental result in Fig. 3.11. The results almost collapse on each other indicating that the incompressible solver was successfully implemented in KATS.

(a) Linear scale

(b) Logarithmic scale
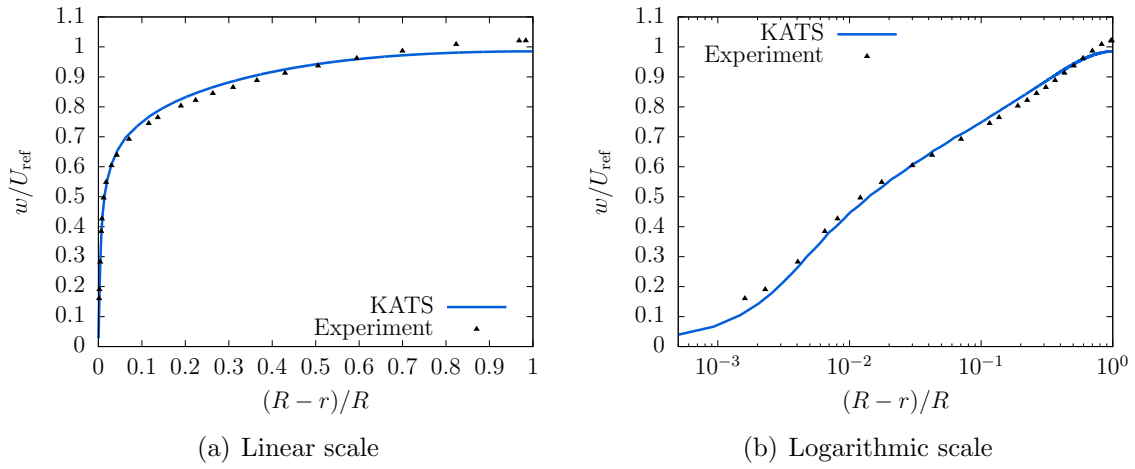
Figure 3.11: Mean axial velocity profile along the radius at $z = 0.8L$ cross section of the pipe for KATS incompressible solver validation.

Chapter 4 Data-Driven Adaptive RANS k-ω Model

This chapter presents a new data-driven adaptive computational model for simulating turbulent flow, where partial-but-incomplete measurement data is available. The model automatically adjusts the closure coefficients of the Reynolds-averaged Navier-Stokes (RANS) k-ω turbulence equations to improve agreement between the simulated flow and the measurements. This data-driven adaptive RANS k-ω (D-DARK) model is validated with three canonical flow geometries: pipe flow, backward-facing step, and flow around an airfoil. For all test cases, the D-DARK model improves agreement with experimental data in comparison to the results from a non-adaptive RANS k-ω model that uses standard values of the closure coefficients. For the pipe flow, adaptation is driven by mean stream-wise velocity data from 42 measurement locations along the pipe radius, and the D-DARK model reduces the average error from 5.2% to 1.1%. For the 2-dimensional backward-facing step, adaptation is driven by mean stream-wise velocity data from 100 measurement locations at four cross-sections of the flow. In this case, D-DARK reduces the average error from 40% to 12%. For the NACA 0012 airfoil, adaptation is driven by surface-pressure data at 25 measurement locations. The D-DARK model reduces the average error in surface-pressure coefficients from 45% to 12%. The result of this chapter is published in [111].

4.1   Introduction

Turbulent flow arises in a vast array of engineering technologies ranging from aerospace vehicles to biomedical devices. Thus, computational techniques for accurate turbulent-flow simulation can advance numerous technologies. Direct numerical simulation

(DNS) is effective for turbulent flow; however, DNS with complex geometry or high Reynolds number requires significant computing resources. Turbulence models such as large-eddy simulation (LES), detached-eddy simulation (DES), and Reynolds-averaged Navier-Stokes (RANS) are employed to reduce computational cost about DNS. However, these turbulence models, particularly RANS, contain model coefficients which may not necessarily be universal. The best values for the model coefficients are generally problem dependent and often determined using trial-and-error calibration, which relies on experimental data or higher-fidelity numerical results.

The concept of *adaptation* has been employed in a variety of ways to improve the accuracy of turbulent flow simulations. For example, scale-adaptive simulations [112, 113, 58, 114] use the von Kármán length scale to adapt the turbulence model to the scale of the mesh. Alternatively, wall functions, which compensate for the simulation cell center nearest to a surface, can also be adapted depending on the local Reynolds number [115] or estimated location relative to the logarithmic layer [116, 117].

The above adaptive approaches are often implemented with RANS models and use the current iteration of the simulated flow for adaptation. Conversely, data assimilation has long been implemented with non-RANS models to improve flow-field reconstruction or prediction (e.g., [69, 70, 71]). The most common application is meteorology, although it is also used in other areas such as training simple fluid models to produce realistic-looking computer generated scenes in real time [72]. In meteorological modeling, measurement data can be incorporated in a computational fluid dynamics (CFD) model using approaches ranging from simple interpolation to direct incorporation in the governing equations [73]. For example, Pérez-Muñuzuri and Gelpi [74] use a nonlinear forecasting method, which is based on the reconstruction of a chaotic strange attractor, to predict the behavior of cloud coverage based on data from previous years. As another example, Lee and Majda [75] apply a multi-

scale data assimilation method, which is based on stochastic superparameterization, to forecast the turbulent signals on different levels of scale.

Recently, data-driven and data-assimilation approaches have been used with RANS models. For example, Duraisamy et al. and Singh and Duraisamy [87, 118] use an adjoint-driven inversion procedure combining with artificial neural networks and Gaussian process regression to adjust the intermittency parameter and other closure coefficients of a turbulence model to better predict the flow field of turbulent boundary layer undergoing bypass transition to turbulence. Foures et al. [88] do not employ a closure model but instead replace the Reynolds stress term in the RANS equation with a forcing function. This forcing function is then determined using measurement data through a variational formulation and Lagrange-multiplier approach.

In the case where some measurement information is available, data-driven approaches can be used to calibrate closure coefficients. For example, Iungo et al. [89] use a database of high-fidelity LES to calibrate a mixing-length turbulence model to reduce the computational cost of simulating the flow in wind farms.

This chapter presents a new data-driven adaptive CFD model for simulation of turbulent flow, where partial-but-incomplete flow-field information is available. The approach uses a RANS $k - \omega$ turbulence model and is thus termed data-driven adaptive RANS $k - \omega$ (D-DARK). This method automatically adjusts or *adapts* model parameters, specifically, the $k - \omega$ closure coefficients, to improve agreement between the simulated flow field and measured data, which are at spatially separated locations in the flow field. The data-driven adaptive algorithm is implemented in combination with a compressible CFD solver. This chapter also presents D-DARK model validation results with several canonical flow-field geometries: pipe flow, the backward-facing step, and flow around an airfoil. These validation results demonstrate that the D-DARK model improves agreement with experimental data in comparison to the results from a non-adaptive RANS $k - \omega$ model that uses the standard values of the

$k - \omega$ closure coefficients, which are given in Ref. [10].

4.2 Range of k-ω closure coefficients

To ensure that the closure coefficients do not adapt to unrealistic values, we define physically possible ranges for each of the closure coefficients. To do this, we follow the arguments of Wilcox [119] in establishing his recommended values.

In the transport equations, σ_k and σ_ω adjust the contribution of the diffusion due to turbulence relative to viscous effects. Therefore we let,

$$\sigma_k \in [0,\ 1], \qquad \sigma_\omega \in [0,\ 1] \tag{4.1}$$

The standard value for both σ_k and σ_ω is 0.5, established by comparison of model results to experimental data.

Next, Wilcox [119] shows that for homogeneous isotropic turbulence the equations of turbulent kinetic energy conservation and specific dissipation rate conservation can be reduced to an expression related to the ratio β^*/β, which is given by

$$k \sim t^{-\beta^*/\beta}. \tag{4.2}$$

Using Refs. [120], [121], and [122, p. 160], a range for this ratio can be provided as

$$\beta^*/\beta \in [0.9, 2.5] \tag{4.3}$$

which encompasses values for homogeneous isotropic turbulence in both the initial period of decay, where β^*/β is empirically observed to be approximately 1.3, and final period of decay, where it can found be from self-similar solution of the Kármán-Howarth equation to be 5/2.

To find a suitable range for β^* we examine the logarithmic layer of a high-Reynolds-number turbulent boundary layer, where the turbulent kinetic energy is generated and dissipated rapidly, the diffusion caused by molecular viscosity is much

smaller than that associated with the Reynolds stress. In this region, the mean velocity $\boldsymbol{U}$ is assumed to be parallel to the wall direction x and is assumed to vary logarithmically with the distance y from the wall. Under these assumptions, the steady-state conservation equations can be solved for the velocity profile

$$u = \frac{u_\tau}{\kappa} \ln \left(\frac{u_\tau y \rho}{\mu} \right), \tag{4.4}$$

and for the turbulent kinetic energy

$$k = \frac{u_\tau^2}{\sqrt{\beta^*}}, \tag{4.5}$$

where κ is the von Kármán constant, and $u_\tau = \sqrt{\tau_w / \rho}$ is the friction velocity with τ_w the shear stress at the wall. See Ref. [119] for more details. However, the approach in Ref. [119] imposes a constraint between the von Kármán constant κ and the closure coefficients, which is given by

$$\alpha = \frac{\beta}{\beta^*} - \frac{\sigma_\omega \kappa^2}{\sqrt{\beta^*}}, \tag{4.6}$$

where $\kappa \in [0.37,\ 0.42]$ [123].

The experimental results presented in [124], which were performed in different flow regimes, show a range in the ratio of Reynolds shear stress, τ^*, to k of

$$\frac{\tau^*}{k} \in [0.19,\ 0.41], \tag{4.7}$$

where τ^* is the streamwise/wall-normal shear stress in the Reynolds stress tensor. In the logarithmic region of high Reynolds number turbulent boundary layers, typical ranges observed for the ratio between u_τ and τ^* are

$$\frac{u_\tau^2}{\tau^*} \in [0.9,\ 1.1], \tag{4.8}$$

as shown in Townsend [124]. Thus, the combination of (4.5), (4.7), and (4.8) imply that

$$\beta^* \in [0.029,\ 0.20], \tag{4.9}$$

which, assuming the range of β^*/β for homogeneous isotropic turbulence holds approximately for anisotropic, inhomogeneous turbulence, can be combined with (4.3) to yield a condition on β, which is given by $\beta \in [0.012, 0.23]$. Note that this condition on β is not sufficient to ensure (4.3) but rather provides an approximation for a range of physically possible parameters β.

To obtain bounds for α, note that it is the coefficient assigned to the production term of the conservation equation for the dissipation rate, which implies that $\alpha \geq 0$. Since $\alpha \geq 0$, it follows from (4.1), (4.3), and (4.6) that

$$\alpha \in [0, \, 1.1]. \tag{4.10}$$

Thus, to ensure physically reasonable values of the closure coefficients, the adapted coefficients produced by the data-driven algorithm described in the next section updates the $k\text{-}\omega$ closure coefficients subject to the constraints described by (4.1), (4.3), (4.9), and (4.10).

4.3 Data-driven adaptation

The D-DARK model relies on known flow-field measurements (e.g., mean velocities, or pressure) at N locations in the physical flow to adapt the $k\text{-}\omega$ closure coefficients

$$\boldsymbol{\theta} = \begin{bmatrix} \alpha & \beta & \beta^* & \sigma_k & \sigma_\omega \end{bmatrix}^{\mathrm{T}}. \tag{4.11}$$

We use the term *'measurement'* to describe information about the flow field that is known *a priori* at N locations.

For $i = 1, \ldots, N$, let $\boldsymbol{\phi}_{\mathrm{m},i} \in \mathbb{R}^{\ell_i}$ denote the ith flow-field measurement, that is, the flow-field measurement at the ith location, and let $\boldsymbol{\phi}_i(\boldsymbol{\theta}) \in \mathbb{R}^{\ell_i}$ denote the simulated flow-field values at the ith location that are obtained with $k\text{-}\omega$ closure coefficients $\boldsymbol{\theta}$. We use the difference between the simulated $\boldsymbol{\phi}_i(\boldsymbol{\theta})$ and measured $\boldsymbol{\phi}_{\mathrm{m},i}$ values to

adapt $\boldsymbol{\theta}$. In particular, we seek to minimize the cost function

$$J(\boldsymbol{\theta}) \triangleq \sum_{i=1}^{N} [\boldsymbol{\phi}_i(\boldsymbol{\theta}) - \boldsymbol{\phi}_{\mathrm{m},i}]^{\mathrm{T}} \boldsymbol{\mathcal{W}}_i [\boldsymbol{\phi}_i(\boldsymbol{\theta}) - \boldsymbol{\phi}_{\mathrm{m},i}], \qquad (4.12)$$

where $\boldsymbol{\mathcal{W}}_1, \ldots, \boldsymbol{\mathcal{W}}_N$ are symmetric positive-definite weighting matrices, which reflect the relative importance of the N measurements as well as the relative importance of the elements of each measurement. For example, if the ith weighting matrix is $\boldsymbol{\mathcal{W}}_i = \mathrm{diag}(w_{i,1}, w_{i,2}, w_{i,3} \ldots)$, where $\mathrm{diag}(\cdot)$ is a diagonal matrix whose diagonal elements are given by the arguments of the operator, then $w_{i,j} > 0$ is the weight associated with the jth element of the ith measurement. If each element of the ith measurement has equal weight, then the weighting matrix can be expressed as

$$\boldsymbol{\mathcal{W}}_i = w_i \boldsymbol{\mathcal{I}}, \qquad (4.13)$$

where $w_i > 0$ reflects the relative importance of the ith measurement. As an example, the weight w_i in (4.13) can be selected to normalize each term in the cost (4.12). In this case, the weight is $w_i = 1/\|\boldsymbol{\phi}_{\mathrm{m},i}\|^2$, where $\|\cdot\|$ is the Euclidean norm. This weight yields a cost (4.12) that reflects an approximately equal importance of minimizing the error $\|\boldsymbol{\phi}_i(\boldsymbol{\theta}) - \boldsymbol{\phi}_{\mathrm{m},i}\|$ for each $i = 1, \ldots, N$ independent of the magnitude $\|\boldsymbol{\phi}_{\mathrm{m},i}\|$ of each measurement. In this chapter, we adopt a variation on the normalized weight, where we also impose upper and lower bounds $w_{\mathrm{max}} > 0$ and $w_{\mathrm{min}} > 0$ on the weight w_i. Specifically, for $i = 1, \ldots, N$, the weight is

$$w_i = \min \left\{ \max \left\{ \frac{1}{\|\boldsymbol{\phi}_{\mathrm{m},i}\|^2}, w_{\mathrm{min}} \right\}, w_{\mathrm{max}} \right\}. \qquad (4.14)$$

The selection of the upper w_{max} and lower w_{min} bounds is discussed in the examples.

In general, (4.12) is a nonlinear function of $\boldsymbol{\theta}$ without a known analytic expression. Thus, it is not feasible to compute the analytic gradient of J with respect to $\boldsymbol{\theta}$; however, this gradient can be approximated numerically. To approximate the gradient, let ℓ_θ denote the number of entries in the vector $\boldsymbol{\theta}$. For a single set of $k\text{-}\omega$

closure coefficients as shown in (4.11), it follows that $\ell_\theta = 5$. However, if different closure coefficients are used at different spatial locations in the flow, then $\ell_\theta > 5$. Section 4.6.2 demonstrates that segmenting the flow (i.e., using different $k\text{-}\omega$ closure coefficients at different spatial locations) can improve performance. Next, let $\epsilon_0 << 1$ be positive, and define the *approximate gradient*

$$\mathbf{\Gamma}(\boldsymbol{\theta}) \triangleq \begin{bmatrix} \dfrac{J(\boldsymbol{\theta} + \epsilon_0 \boldsymbol{e}_1^{\mathrm{T}} \boldsymbol{\theta} \boldsymbol{e}_1) - J(\boldsymbol{\theta})}{\epsilon_0 \boldsymbol{e}_1^{\mathrm{T}} \boldsymbol{\theta}} \\ \vdots \\ \dfrac{J(\boldsymbol{\theta} + \epsilon_0 \boldsymbol{e}_{\ell_\theta}^{\mathrm{T}} \boldsymbol{\theta} \boldsymbol{e}_{\ell_\theta}) - J(\boldsymbol{\theta})}{\epsilon_0 \boldsymbol{e}_{\ell_\theta}^{\mathrm{T}} \boldsymbol{\theta}} \end{bmatrix} \in \mathbb{R}^{\ell_\theta}, \tag{4.15}$$

where for $j = 1, \ldots, \ell_\theta$, let $\boldsymbol{e}_j \in \mathbb{R}^{\ell_\theta}$ is the jth column of the $\ell_\theta \times \ell_\theta$ identity matrix. For sufficiently small $\epsilon_0 > 0$, $\mathbf{\Gamma}^{\mathrm{T}}(\boldsymbol{\theta})$ approximates the gradient of J with respect to $\boldsymbol{\theta}$, that is, $\mathbf{\Gamma}^{\mathrm{T}}(\boldsymbol{\theta}) \approx \partial J(\boldsymbol{\theta})/\partial \boldsymbol{\theta}$. Furthermore, (4.15) can be computed numerically by perturbing each element of $\boldsymbol{\theta}$ and computing the change in the cost J.

The approximate gradient (4.15) indicates the direction in which $\boldsymbol{\theta}$ should be adjusted to reduce the difference between $\boldsymbol{\phi}_i(\boldsymbol{\theta})$ and $\boldsymbol{\phi}_{\mathrm{m},i}$. To develop an adaptive law for $\boldsymbol{\theta}$, let $\boldsymbol{\theta}_0 \in \mathbb{R}^{\ell_\theta}$ denote the initial value for the vector of $k\text{-}\omega$ closure coefficients. For example, $\boldsymbol{\theta}_0$ can be the closure coefficients proposed in [47]. Then, at each step $n \in \mathbb{N} \triangleq \{0, 1, 2, \ldots\}$, the updated parameter $\boldsymbol{\theta}_{n+1}$ is determined from the adaptive law

$$\boldsymbol{\theta}_{n+1} = \boldsymbol{\theta}_n - \xi_n \mathbf{\Gamma}(\boldsymbol{\theta}_n), \tag{4.16}$$

where $\xi_n > 0$ is the adaptive step size.

To determine the adaptive step size, let $\boldsymbol{\theta}_* \in \mathbb{R}^{\ell_\theta}$ denote a local minimizer of J. Note that the local minimizer $\boldsymbol{\theta}_*$ is assumed to exist but is not necessarily a global minimizer of J and is not necessarily unique. Next, for all $n \in \mathbb{N}$, consider the cost function

$$\mathcal{J}_n(\xi_n) \triangleq \|\boldsymbol{\theta}_{n+1} - \boldsymbol{\theta}_*\|^2 - \|\boldsymbol{\theta}_n - \boldsymbol{\theta}_*\|^2. \tag{4.17}$$

62

We seek to determine a step size ξ_n such that $\mathcal{J}_n(\xi_n) < 0$, which implies that $\boldsymbol{\theta}_n$ gets closer to the minimizer $\boldsymbol{\theta}_*$ at each step n. For each $n \in \mathbb{N}$, define the *optimal step size*

$$\xi_{\mathrm{opt},n} \triangleq \frac{2\left[J(\boldsymbol{\theta}_n) - J(\boldsymbol{\theta}_*)\right]}{\|\boldsymbol{\Gamma}(\boldsymbol{\theta}_n)\|^2}. \tag{4.18}$$

The following result demonstrates that if $\boldsymbol{\Gamma}$ is equal to the transpose of the gradient, and $\boldsymbol{\phi}_i$ is affine in $\boldsymbol{\theta}$, then the optimal step size $\xi_{\mathrm{opt},n}$ minimizes the cost $\mathcal{J}_n$. The proof is in Appendix A.

Theorem 1. Consider the adaptive law (4.16), and assume that the following conditions are satisfied:

(A1) For all $n \in \mathbb{N}$, $\boldsymbol{\Gamma}(\boldsymbol{\theta}_n) \neq 0$.

(A2) For all $n \in \mathbb{N}$, $\boldsymbol{\Gamma}(\boldsymbol{\theta}_n) = (\partial J(\boldsymbol{\theta})/\partial\boldsymbol{\theta}|_{\boldsymbol{\theta}=\boldsymbol{\theta}_n})^{\mathrm{T}}$.

(A3) For $i = 1, \ldots, N$, there exists $\boldsymbol{\Phi}_i \in \mathbb{R}^{\ell_i \times \ell_\theta}$ and $\boldsymbol{\psi}_i \in \mathbb{R}^{\ell_i}$ such that $\boldsymbol{\phi}_i(\boldsymbol{\theta}) = \boldsymbol{\Phi}_i\boldsymbol{\theta} + \boldsymbol{\psi}_i$.

Then, for all $n \in \mathbb{N}$, $\mathcal{J}_n(\xi_n) < 0$ if and only if $0 < \xi_n < 2\xi_{\mathrm{opt},n}$. Furthermore, for all $n \in \mathbb{N}$, $\xi_n = \xi_{\mathrm{opt},n}$ minimizes $\mathcal{J}_n(\xi_n)$.

Theorem 1 imposes the assumption that $\boldsymbol{\phi}_i$ is affine in $\boldsymbol{\theta}$. While this assumption is most likely not valid globally in $\boldsymbol{\theta}$, it is reasonable to assume that $\boldsymbol{\phi}_i$ can be approximate locally as an affine function of $\boldsymbol{\theta}$.

Theorem 1 shows that under simplifying assumptions the optimal step size $\xi_{\mathrm{opt},n}$ minimizes $\mathcal{J}_n$; however, $\xi_{\mathrm{opt},n}$ is not implementable because $\boldsymbol{\theta}_*$ and thus $J(\boldsymbol{\theta}_*)$ are unknown. Nevertheless, if we assume that $J(\boldsymbol{\theta}_*)$ is small (i.e., $J(\boldsymbol{\theta}_*) \approx 0$), then we can consider the approximately optimal step size

$$\xi_{*,n} \triangleq \frac{2J(\boldsymbol{\theta}_n)}{\|\boldsymbol{\Gamma}(\boldsymbol{\theta}_n)\|^2}, \tag{4.19}$$

which is implementable. Thus, $\xi_{*,n}$ is the maximum allowable step size; however, we also aim to select a step size that is small enough to ensure that the cost J does not

increase and that the k-ω closure coefficients do not change more than a user-selected threshold percentage $\bar{p} > 0$. Therefore, for each step $n \in \mathbb{N}$, the adaptive step size is given by

$$\xi_n \triangleq \left(\frac{1}{2} \right)^{\gamma_n} \eta_n, \tag{4.20}$$

where

$$\eta_n \triangleq \min \left\{ \min_{j=1,\dots,\ell_\theta} 10^{-2} \bar{p} \left| \frac{\boldsymbol{e}_j^{\mathrm{T}} \boldsymbol{\theta}_n}{\boldsymbol{e}_j^{\mathrm{T}} \boldsymbol{\Gamma}(\boldsymbol{\theta}_n)} \right|, \xi_{*,n} \right\}, \tag{4.21}$$

and where γ_n is the smallest nonnegative integer such that

$$J \left(\boldsymbol{\theta}_n - \left(\frac{1}{2} \right)^{\gamma_n} \eta_n \boldsymbol{\Gamma}(\boldsymbol{\theta}_n) \right) \leq J(\boldsymbol{\theta}_n), \tag{4.22}$$

and $\boldsymbol{\theta}_n - (1/2)^{\gamma_n} \eta_n \boldsymbol{\Gamma}(\boldsymbol{\theta}_n)$ satisfies the constraints (4.1), (4.3), (4.9), and (4.10).

If $\xi_{*,n} \leq \min_{j=1,\dots,\ell_\theta} 10^{-2} \bar{p} | \boldsymbol{e}_j^{\mathrm{T}} \boldsymbol{\theta}_n / (\boldsymbol{e}_j^{\mathrm{T}} \boldsymbol{\Gamma}(\boldsymbol{\theta}_n)) |$ and $\gamma_n = 0$, then the step size is $\xi_n = \xi_{*,n}$. However, if the approximately optimal step size $\xi_{*,n}$ yields an updated closure coefficient that is more than $\bar{p}$ percent from its current value, then (4.21) implies that $\eta_n < \xi_{*,n}$, and it follows from (4.20) that $\xi_n < \xi_{*,n}$. In this case, if $\gamma_n = 0$ satisfies (4.22) and the constraints (4.1), (4.3), (4.9), and (4.10), then the step size is $\xi_n = \eta_n = \min_{j=1,\dots,\ell_\theta} 10^{-2} \bar{p} | \boldsymbol{e}_j^{\mathrm{T}} \boldsymbol{\theta}_n / (\boldsymbol{e}_j^{\mathrm{T}} \boldsymbol{\Gamma}(\boldsymbol{\theta}_n)) |$. If, on the other hand, this step size violates (4.1), (4.3), (4.9), (4.10), or (4.22), then the integer γ_n is increased (i.e., η_n is bisected) until (4.1), (4.3), (4.9), (4.10), and (4.22) are satisfied.

4.4 Implementation

The D-DARK approach is illustrated in Fig. 4.1. We assume that the measurements $\boldsymbol{\phi}_{\mathrm{m},1}, \dots, \boldsymbol{\phi}_{\mathrm{m},N}$ are obtained *a priori*. Next, a numerical simulation is conducted with the initial closure coefficients $\boldsymbol{\theta}_0$, and a solution is obtained through convergence of (3.10), which yields the initial simulation results $\boldsymbol{\phi}_1(\boldsymbol{\theta}_0), \dots, \boldsymbol{\phi}_N(\boldsymbol{\theta}_0)$. The initial cost $J(\boldsymbol{\theta}_0)$ is constructed using the measurements $\boldsymbol{\phi}_{\mathrm{m},i}$ and the simulation data $\boldsymbol{\phi}_i(\boldsymbol{\theta}_0)$. The weighting matrices $\boldsymbol{\mathcal{W}}_i$ used to compute the cost J are given by (4.13) and
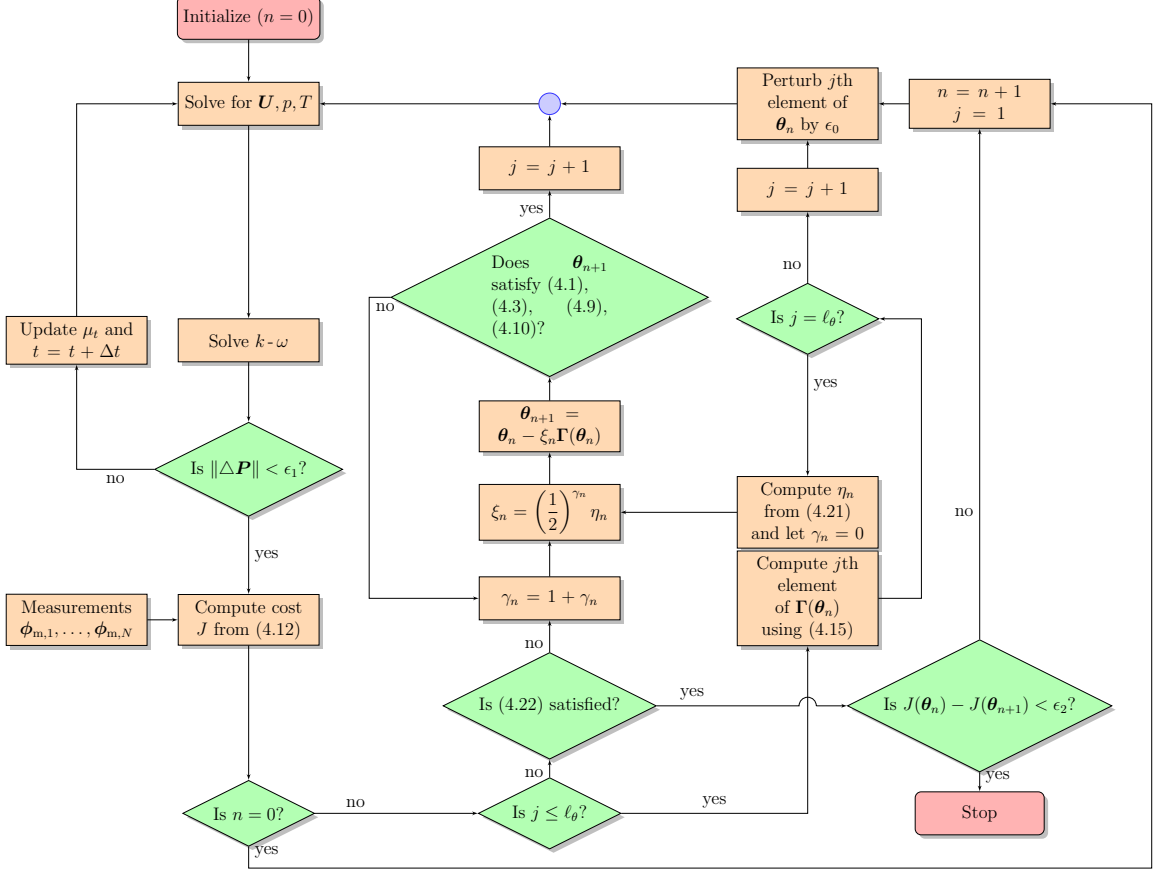
Figure 4.1: Flow chart for D-DARK model. Note that $\epsilon_1 > 0$ and $\epsilon_2 > 0$ are the convergence thresholds for the primitive variables and adaptation cost, respectively.

(4.14). The upper and lower bounds in (4.14) are

$$w_{\max} = \frac{10^2}{\phi_{\mathrm{av}}^2}, \qquad w_{\min} = \frac{1}{\phi_{\mathrm{av}}^2}, \tag{4.23}$$

where $\phi_{\mathrm{av}} \in \mathbb{R}$ is either the far-field mean stream-wise velocity or the far-field mean pressure depending on the measurement type. Thus, for each $i = 1, \ldots, N$, if $\|\boldsymbol{\phi}_{\mathrm{m},i}\| > |\phi_{\mathrm{av}}|$, then the weight is $w_i = w_{\min}$, and if $\|\boldsymbol{\phi}_{\mathrm{m},i}\| < |\phi_{\mathrm{av}}|/10$, then the weight is $w_i = w_{\max}$. If, on the other hand, $\|\boldsymbol{\phi}_{\mathrm{m},i}\| \in [|\phi_{\mathrm{av}}|/10, |\phi_{\mathrm{av}}|]$, then the weight is $w_i = 1/\|\boldsymbol{\phi}_{\mathrm{m},i}\|^2$. Thus, the minimum weight is used for measurements with magnitude greater than the far-field mean value, while larger weights are used for measurements with magnitude less than the far-field mean value. This selection of the weights normalizes the cost J and helps to account for measurements with dif-

ferent magnitudes. In the following sections, the values for ϕ_{av} are provided in each example.

For each adaptation step n, the approximate gradient $\mathbf{\Gamma}(\boldsymbol{\theta}_n)$ is calculated by individually perturbing each element of $\boldsymbol{\theta}_n$ and simulating the flow-field response. If the positive perturbation $\epsilon_0 << 1$ is sufficiently small, then $\mathbf{\Gamma}(\boldsymbol{\theta}_n)$ approximates the gradient. In this work, $\epsilon_0 = 10^{-7}$, which was determined through numerical testing. If $\epsilon_0 < 10^{-7}$, then the perturbation is less than the numerical accuracy of KATS. After perturbing the jth element of $\boldsymbol{\theta}_n$, a numerical simulation is performed to compute the perturbed cost $J(\boldsymbol{\theta} + \epsilon_0 \boldsymbol{e}_j^{\mathrm{T}} \boldsymbol{\theta} \boldsymbol{e}_j)$. Note that each closure coefficient is perturbed individually, which implies that ℓ_θ perturbations and numerical simulations are required to calculate $\mathbf{\Gamma}(\boldsymbol{\theta}_n)$. However, each simulation requires relatively few computational steps to converge because the perturbation ϵ_0 is small. In addition, the results in the following sections suggest that for certain flow geometries, relatively few (e.g., $n \leq 20$) adaptive steps are needed for the cost J to converge.

The closure coefficients are updated according (4.16), where the step size ξ_n is determined from (4.20)–(4.22), where the approximately optimal step size $\xi_{*,n}$ is given by (4.19). The maximum allowable percent change is $\bar{p} = 10$, which was determined by numerical testing. If $\bar{p} > 10$, then numerical testing shows that for many adaptation steps n, the nonnegative integer γ_n must be greater than zero to satisfy (4.22). In this case, an additional simulation is required each time that γ_n is increased.

4.5   D-DARK model verification with pipe flow

The D-DARK model and its numerical implementation are verified using the test case of air flow through a pipe. This test case is solved on a 3-dimensional mesh with cell clustering near the wall as shown in Fig. 3.3. The mesh is refined in the near-wall region to ensure smooth mesh transition from the wall to the center of the pipe. The computational mesh consists of $106,080$ cells, and produces grid-independent results

as determined through comparison with results from a similar mesh with $225,000$ cells.

For this test case, the pipe's radius and length are $R = 0.06$ m and $L = 2.4$ m. The total temperature $T_t = 288.025$ K and total pressure $p_t = 101,427.5$ Pa are specified at the inlet. A static pressure boundary condition $p = 101,325$ Pa is applied at the outlet. The reference velocity is the area-averaged velocity at the inlet, which is approximate $U_{\mathrm{ref}} = 12$ m/s. The Reynolds number based on pipe diameter and reference velocity is approximate $\mathrm{Re}_D = 100,000$. The turbulence intensity and eddy-viscosity-to-molecular-viscosity ratio at the inlet are $I_t = 0.01$ and $\mu_t/\mu = 0.1$. The upper and lower bounds (4.23) for the cost-function weights are computed using $\phi_{\mathrm{av}} = 11.32$ m/s, which is the far-field mean stream-wise velocity.

For this verification, a numerical solution is first obtained using standard values of the $k\text{-}\omega$ closure coefficients [10], which are in Table 4.1. This solution is used as the *'measurement'*, where each cell is a 'measurement' location, that is, $N = 106,080$, and for each $i = 1,\ldots,N$, the 'measurement' $\phi_{\mathrm{m},i}$ has 3 elements, which are the components u, v, and U_z of flow velocity at the ith location. The D-DARK model is initialized with closure coefficients $\boldsymbol{\theta}_0$ that are different from the standard values used to obtain the 'measurement.' The D-DARK model adapts the closure coefficients until the cost J converges, which occurs after $n_{\mathrm{f}} = 4$ steps. The initial $\boldsymbol{\theta}_0$ and adapted $\boldsymbol{\theta}_{n_{\mathrm{f}}}$ closure coefficients are also given in Table 4.1.

Table 4.1: D-DARK closure coefficients for the pipe-flow verification.

	σ_k	σ_ω	β	β^*	α
Initial	0.4000	0.6000	0.06200	0.08500	0.4500
Adapted	0.4001	0.6000	0.06700	0.08201	0.4501
Measurement	0.5000	0.5000	0.07200	0.09000	0.5200

Figure 4.2 shows the fully-developed mean stream-wise velocity U_z profile at the stream-wise location $z = 0.8L$. The figure shows the 'measurement' results and the D-DARK model results with the initial $\boldsymbol{\theta}_0$ and adapted $\boldsymbol{\theta}_{n_{\mathrm{f}}}$ closure coefficients. The difference between the 'measurement' and the numerical results with the initial

$\boldsymbol{\theta}_0$ closure coefficients is noticeable, particularly in the near-wall and outer layers of the flow. However, after convergence, the D-DARK solution coincides with the 'measurement'. The maximum percent error in the overlap and outer layers (i.e., $(R - r)/R > 10^{-2}$) decreases from 2.45% with the initial $\boldsymbol{\theta}_0$ closure coefficients to 0.033% with the adapted $\boldsymbol{\theta}_{n_{\mathrm{f}}}$ closure coefficients.
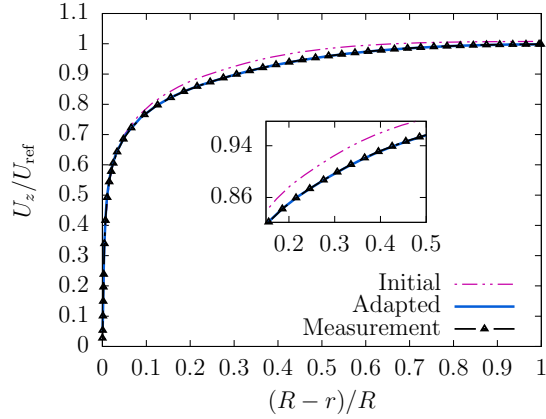
(a) Linear scale
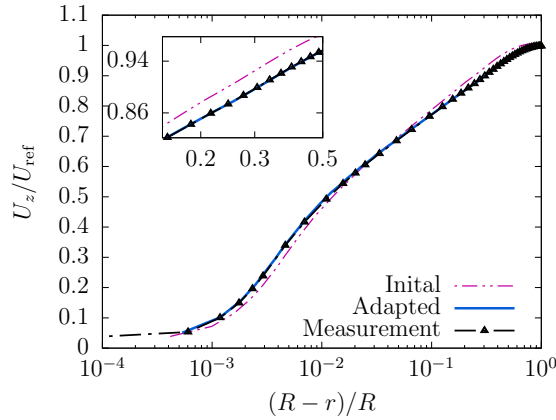
(b) Logarithmic scale

Figure 4.2: Mean stream-wise velocity U_z profile for the pipe-flow verification at the $z = 0.8L$ cross section. Results are shown for the D-DARK model with the initial and adapted closure coefficients, and for the 'measurement'.

As shown in Table 4.1, the improvement occurs following less than 8.1% change in the value of the closure coefficients, demonstrating the sensitivity of the results to the closure coefficients. Note also that the adapted closure coefficients are not equal

to the closure coefficients used to produce the 'measurement', which suggests that the cost J has multiple local minima. Thus, the data-driven adaptation algorithm may be sensitive to the initial value $\boldsymbol{\theta}_0$. Nevertheless, the adaptation improved agreement with the 'measurement' by an average of 95%. These results demonstrate that the D-DARK model can adapt the flow-field solution to improve agreement with a set of known 'measurements', which could be physical measurements, an analytic flow-field solution, or results from another numerical simulation.

4.6 Validation

This section presents validation results, where the D-DARK model is applied to 3 test cases: pipe flow, the backward-facing step, and flow around an airfoil. For each test case, experimental data is used as the *measurement* for model adaptation.

4.6.1 Pipe flow

For the pipe-flow validation, we use experimental data published in [1], which provides fully-developed mean stream-wise velocity data at 42 different locations along the radius of a pipe. These experimental data are used as the measurement, that is, $N = 42$ and for each $i = 1, \ldots, N$, the measurement $\boldsymbol{\phi}_{\mathrm{m},i} \in \mathbb{R}$ is the mean stream-wise velocity at the ith location.

The simulation domain and boundary conditions are defined to match those of the experiment except the pipe length $L = 2.4$ m, which was found to be sufficiently long for the mean velocity to approximate fully-developed flow conditions. The pipe radius is $R = 0.06$ m, and the reference velocity is the area-averaged velocity at the inlet, which is approximate $U_{\mathrm{ref}} = 10.8$ m/s; both of which match the experimental conditions. The Reynolds number based on pipe diameter and reference velocity is approximately $\mathrm{Re}_D = 89,000$. The computational mesh consists of $225,000$ cells, and produces grid-independent results as determined through comparison with results

from a similar mesh with $106,080$ cells. The computational mesh as well as the measurement locations are shown in Fig. 4.3.

<center>(a)</center> <center>(b)</center>
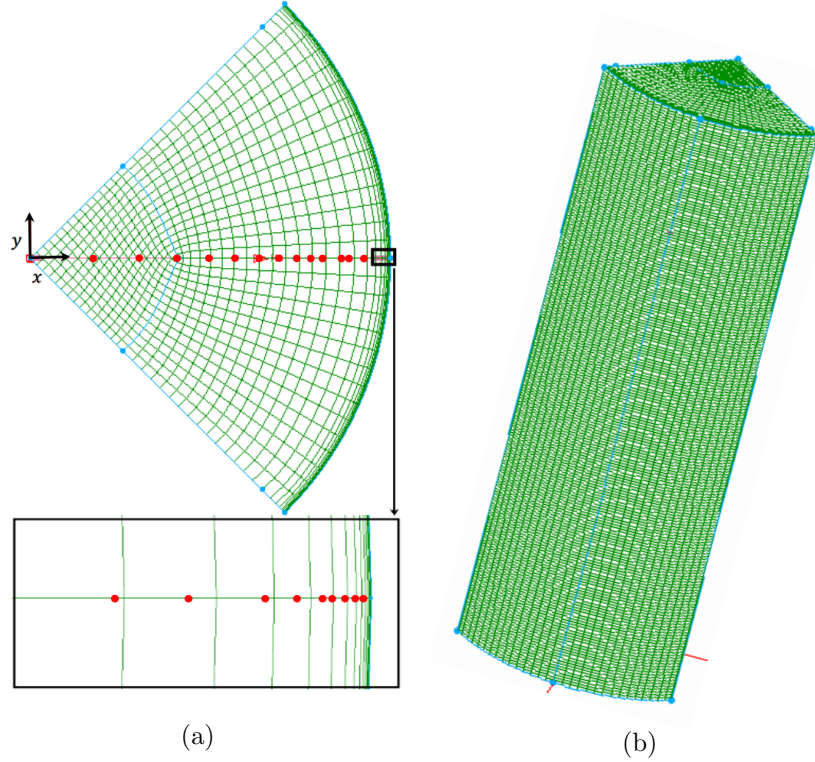
Figure 4.3: Computational mesh used for the pipe-flow validation. The measurement locations are shown as the dots.

The inlet boundary conditions are $T_t = 288.025$ K and $p_t = 101,404$ Pa, and the pressure boundary condition at the outlet is $p = 101,325$ Pa, which together match the experimental pressure gradient. The turbulence intensity and eddy-viscosity-to-molecular-viscosity ratio at the inlet are $I_t = 0.01$ and $\mu_t/\mu = 0.1$. The upper and lower bounds (4.23) for the cost-function weights are computed using $\phi_{av} = 9.71$ m/s, which is the far-field mean stream-wise velocity.

The D-DARK model is initialized with standard values for the k-ω closure coefficients [10], and the model adapts the closure coefficients until the cost J converges, which occurs after $n_f = 4$ steps. The initial and adapted closure coefficients are in Table 4.2. The closure coefficients change significantly more than in the pipe-flow

<center>70</center>

verification. Specifically, β increases by 19%, and β^* decreases by 8.1%, while the remaining closure coefficients change by less than one-tenth of a percent.

Table 4.2: D-DARK closure coefficients for the pipe-flow validation.

	σ_k	σ_ω	β	β^*	α
Initial	0.5000	0.5000	0.07200	0.09000	0.5200
Adapted	0.5002	0.4999	0.08563	0.08269	0.5201

Figure 4.4 shows the fully developed mean stream-wise velocity U_z profile at the stream-wise location $z = 0.8L$. The figure shows the experimental data and the D-DARK model results with the initial and adapted closure coefficients. The difference between the data and numerical results with the initial closure coefficient is noticeable. Figure 4.5 shows the normalized mean stream-wise-velocity error $|(\phi_i(\boldsymbol{\theta}_n) - \phi_{\mathrm{m},i})/\phi_{\mathrm{m},i}|$ at each location i with the initial (i.e., $n = 0$) and adapted (i.e., $n = n_\mathrm{f}$) closure coefficients. Note that the blue lines in Figs. 4.4 and 4.5 correspond to a D-DARK model with two sets of adaptive k-ω closure coefficients; this segmented-flow case is discussed in the next section. As shown in Fig. 4.5, the initial closure coefficients result in an average error of approximately 5.2% in the overlap and outer layers (i.e., $(R - r)/R > 10^{-2}$), and a peak error of approximately 46%, which occurs at $(R - r)/R = 0.0050$. In contrast, the adapted closure coefficients (with one region) result in an average error of approximately 3.3% in the outer layer, and a peak error of approximately 35%, which occurs at $(R - r)/R = 0.0021$. Both of these represent an improvement relative to the results with the initial closure coefficients. As shown in Fig. 4.6, the cost J is reduced by approximately 80% on the first adaptation step, while the additional adaptation steps result in minimal additional reduction to the cost J. Despite this reduction in cost, the adapted D-DARK model over predicts mean velocity near the wall and under predicts mean velocity near the center line.
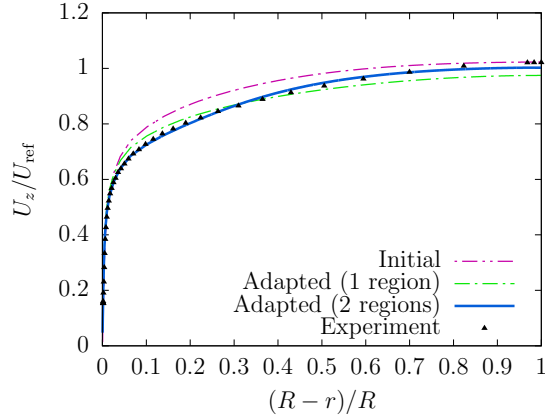
(a) Linear scale
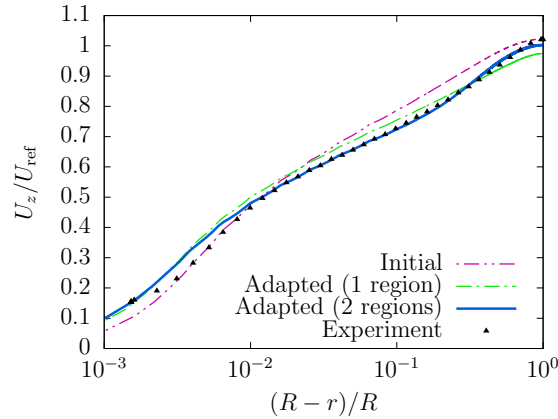
(b) Logarithmic scale

Figure 4.4: Mean stream-wise velocity U_z profile for the pipe-flow validation at the $z = 0.8L$ cross section. Results are shown for the D-DARK model with the initial and adapted closure coefficients (1 and two segmentation regions), and for the measurement data, which are stream-wise velocities at 42 locations [1]. For the 2-region case, the segmentation threshold is $G_{st} = 15$.

4.6.2 Improving accuracy by flow segmentation

This section considers using different adaptive closure coefficients in different spatial locations of the flow to reduce the error between the adapted D-DARK model and the measurement data and to account for possibly different turbulent phenomenon in different regions of the flow. Assuming that phenomenological differences are partially captured by the relative magnitude of velocity gradient, the flow is segmented using
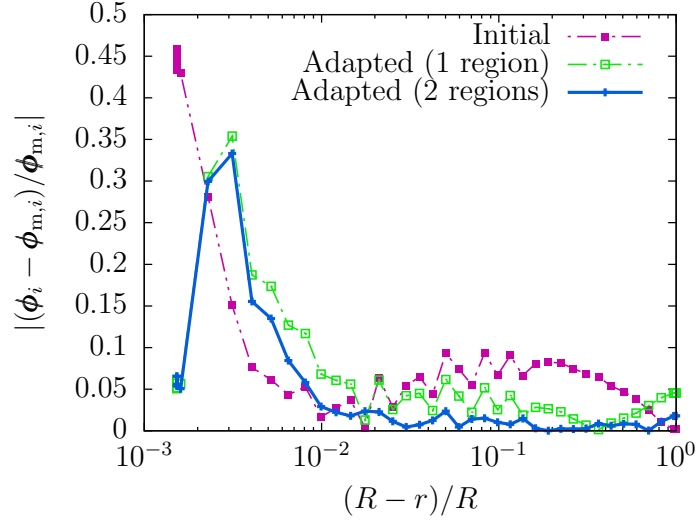
Figure 4.5: Normalized mean stream-wise-velocity error between the D-DARK model and the measurement data, which are stream-wise velocities at 42 locations [1]. Results are shown for the D-DARK model with the initial and adapted closure coefficients (1 and two segmentation regions). For the 2-region case, the segmentation threshold is $G_{st} = 15$.
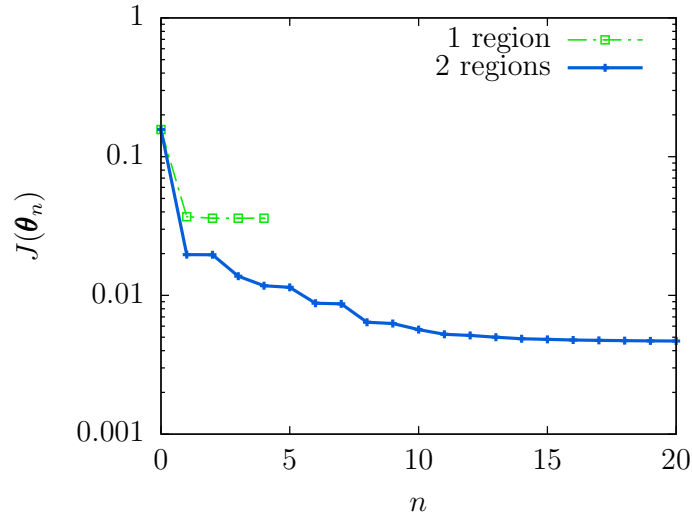
Figure 4.6: Cost J as a function of adaptation step n for the pipe-flow validation. For the 2-region case, the segmentation threshold is $G_{st} = 15$.

the magnitude of a dimensionless velocity gradient relative to Reynolds number, which

is defined as

$$G \triangleq \frac{10^6}{\mathrm{Re}} \left(\|\nabla \boldsymbol{U}\| \frac{\ell}{U_{\mathrm{ref}}} \right), \tag{4.24}$$

where ℓ is a suitably selected characteristic length of the flow, U_{ref} is a characteristic velocity, and Re is the Reynolds number based on ℓ and U_{ref}. Note that 10^6 is a scaling factor. selected characteristic length

To examine the effect of segmentation regions, we perform a parametric study using the pipe flow described above using the area averaged inlet velocity and R to define G and to vary the number of regions and the segmentation thresholds for G. The k-ω closure coefficients for each region are adapted independently by the D-DARK model, thus increasing the dimension ℓ_θ of $\boldsymbol{\theta}_n$.

Figure 4.7 shows the converged cost $J(\boldsymbol{\theta}_{n_{\mathrm{f}}})$ as a function of the segmentation threshold G_{st} for the dimensionless gradient G. If $G_{\mathrm{st}} \in (10, 10^3)$, then the converged cost $J(\boldsymbol{\theta}_{n_{\mathrm{f}}})$ with 2 regions is approximately 70% lower than that with one region. Moreover, Fig. 4.7 suggests that the converged cost is minimized by G_{st} in the interval $(10, 20)$; thus, we consider G_{st} approximately equal to 15. Figure 4.6 shows that 2-region segmentation, where $G_{\mathrm{st}} = 15$, reduces the cost J relative to one region; however, the D-DARK model with two regions requires more adaptation steps for the cost J to converge. Specifically, $n_{\mathrm{f}} = 20$ steps with 2 segmentation regions, where $G_{\mathrm{st}} = 15$.

To investigate further flow segmentation, we set a first segmentation threshold at 15 and conduct a parametric study where a second segmentation threshold is varied across eight orders of magnitude. As shown in Fig. 4.7, the converged cost $J(\boldsymbol{\theta}_{n_{\mathrm{f}}})$ with 3-region segmentation is not significantly lower than that with 2-region segmentation. These results suggest that 2-region segmentation can lead to significant improvement in cost, whereas 3-region segmentation may be unnecessary for certain flows.

Figures 4.4 and 4.5 show that the converged D-DARK model with two regions, where $G_{\mathrm{st}} = 15$, improves agreement with the measurement relative to the case with

74
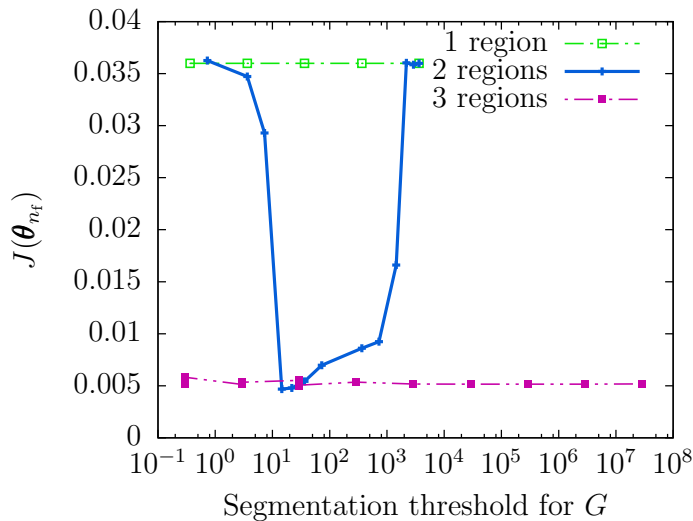
Figure 4.7: Cost J as a function of segmentation threshold for the pipe-flow validation. For the 3-region case, the first segmentation threshold is 15.

one region. Although 2-region segmentation results in minimal improvement near the wall, Fig. 4.5 shows that the adapted closure coefficients (with 2 regions) result in an average error of approximately 1.1% in the outer layer, which is an improvement relative to the case with the initial closure coefficients and the case with one region, which have average outer-layer errors of 5.2% and 3.3%, respectively. Note that flow segmentation can result in discontinuities in the adapted closure coefficients between different regions. However, the values of k, ω, and μ_t for the converged solution remain continuous across different regions.

The initial and adapted closure coefficients are in Table 4.3. The improvement with 2 regions appears to be a result primarily of the differences in the converged β and β^* for the high- and low-gradient regions. For this test case, the adapted coefficients were within the constraints provided by (4.1), (4.3), (4.9), and (4.10) for each step of the adaptation (without bisecting the adaptive step size). As shown in Fig. 4.8, the solutions for k and ω are continuous even though the values of the closure coefficients are discontinuous at the interface between the two segmentation regions.

Table 4.3: D-DARK closure coefficients for the pipe flow with segmentation.

	σ_k	σ_ω	β	β^*	α
Initial	0.5000	0.5000	0.07200	0.09000	0.5200
Adapted $(G > G_{\mathrm{st}})$	0.5001	0.4990	0.08496	0.07967	0.5159
Adapted $(G \leq G_{\mathrm{st}})$	0.5002	0.4999	0.05088	0.1062	0.5201

dimensionless velocity gradient threshold of segmentation dimensionless velocity gradient

4.6.3 Backward-facing step

This section considers a 2-dimensional backward-facing step in order to test the D-DARK model for flows containing both free shear and wall-bounded shear. For this case, we use experimental data published in [2, 3], which provides mean stream-wise velocity data at $N = 100$ measurement locations. Thus, for each $i = 1, \ldots, N$, the measurement $\phi_{\mathrm{m},i} \in \mathbb{R}$ is the mean stream-wise velocity at the ith location.

The experiment in [2, 3] was conducted with a reference Mach number of 0.128 and a reference temperature of 298.33 K. The height of the step was $H = 0.01$ m, and the free-stream reference velocity was $U_{\mathrm{ref}} = 43$ m/s. Thus, the Reynolds number based on height and reference velocity is approximately $\mathrm{Re}_H = 28,000$. The simulation domain and boundary conditions are defined to match those of the experiment. Specifically, the flow field is initialized using free-stream conditions of 298.33 K and $101,325$ Pa. The inlet boundary conditions are $T_t = 299.3109$ K and $p_t = 102,350$ Pa, and the pressure boundary condition at the outlet is $p = 101,325$ Pa. The turbulence intensity and eddy-viscosity-to-molecular-viscosity ratio at the inlet are $I_t = 6.1 \times 10^{-4}$ and $\mu_t/\mu = 0.009$. The upper and lower bounds (4.23) for the cost-function weights are computed using $\phi_{\mathrm{av}} = 40.85$ m/s, which is the far-field mean stream-wise velocity.

The computational mesh for this test case is that distributed by NASA [125]. This mesh consists of $23,216$ cells and produces grid-independent results as determined through comparison with results from a similar mesh with $81,280$ cells. The
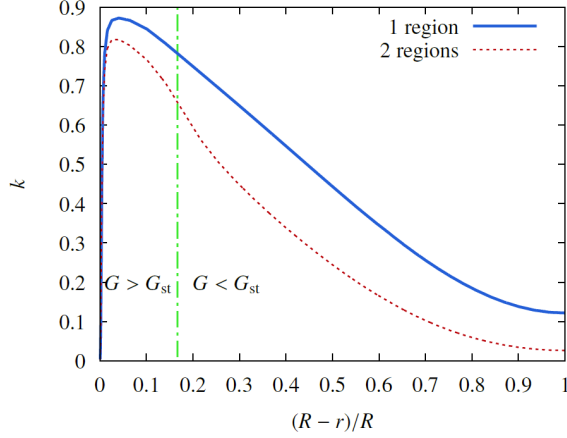
(a) Solution for k
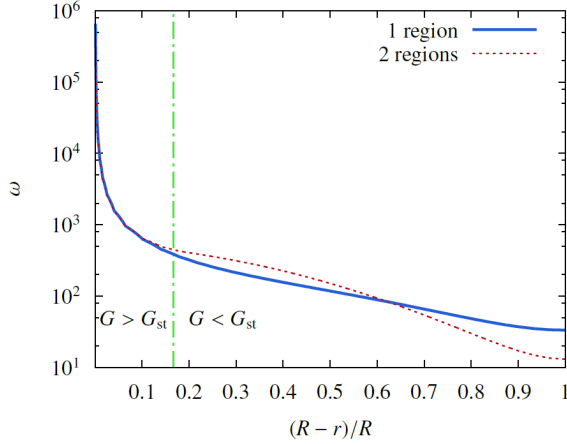
(b) Solution for ω

Figure 4.8: Radial solution of the k and ω variables at $z = 0.8L$ obtained using the 1-region model (blue) and the 2-region segmentation model (red). For the latter case, the solution is smooth.

computational mesh as well as the measurement locations are shown in Fig. 4.9. Note that measurement locations near the wall are not shown because of the density of these measurement locations.

The D-DARK model is initialized with standard values for the k-ω closure coefficients [10], and the model adapts the closure coefficients until the cost J converges, which occurs after $n_{\mathrm{f}} = 4$ steps. The initial and adapted closure coefficients are in Table 4.4. The coefficient β decreases by 6.5%, and β^* increases by 2.2%, while the
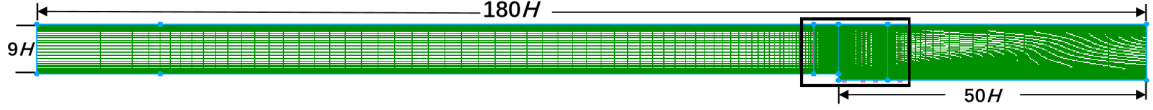
(a) Entire computational domain
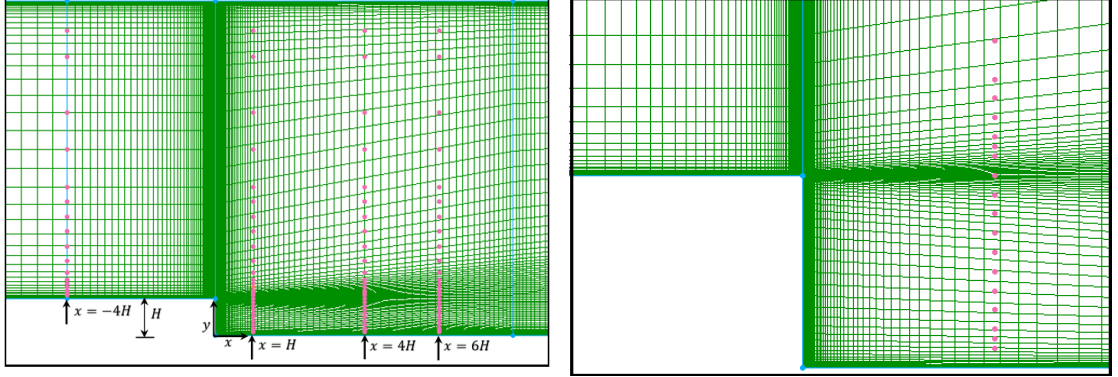
(b) Zoom-in view of the measurements points in the flow

(c) Zoom-in view of the measurement points near the step

Figure 4.9: Computational mesh used for the backward-facing step, with he measurement locations shown as the dots.

remaining closure coefficients changed by approximately one-tenth of a percent.

Table 4.4: D-DARK closure coefficients for the backward-facing step.

	σ_k	σ_ω	β	β^*	α
Initial	0.5000	0.5000	0.07200	0.09000	0.5200
Adapted	0.5004	0.4995	0.06732	0.09188	0.5206

The near-step flow using the initial closure coefficients is illustrated in Fig. 4.10 (a), where Ω_z is the z component of vorticity normalized by U_{ref} and H. This figure shows that the simulation captures important features of the flow, including flow separation after the step and reattachment at $x/H \approx 6$, which produces a large primitive recirculation region and a smaller counter-rotating secondary recirculation region close to the step. Fig. 4.11 shows that the results with the initial closure coefficients agree with the measurements near the far wall, but fail to capture near-wall features of the flow. In particular, Fig. 4.11 (b) shows that the result with the initial closure coefficients fails to capture the signature flow reversal in the $x/H = 1$ recirculation region. How-
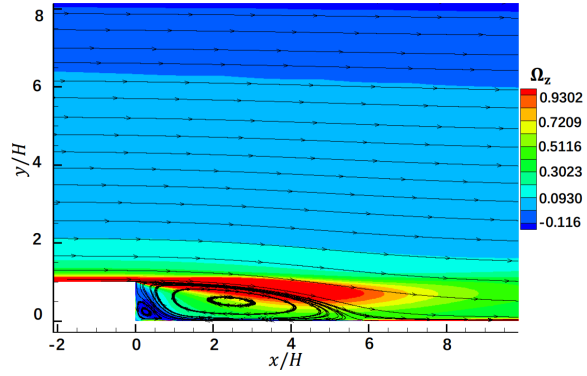
(a) Initial
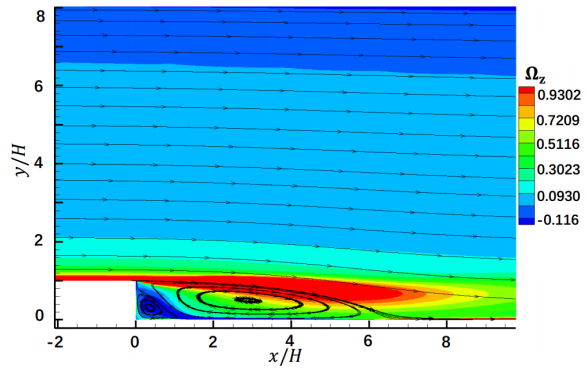
(b) Adapted (1 region)
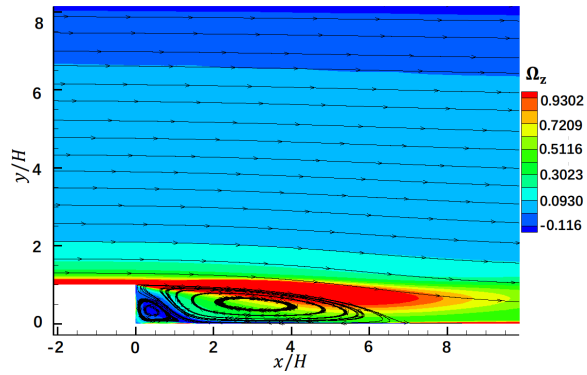
(c) Adapted (2 regions)

Figure 4.10: Vorticity contours and streamlines for the backward-facing step. Results are shown for the D-DARK model with (a) the initial closure coefficients, (b) the adapted closure coefficients with one region, and (c) the adapted closure coefficients with two segmentation regions. For the 2-region case, the segmentation threshold is $G_{\text{st}} = 15$.

ever, Fig. 4.11 shows that the adapted D-DARK model (with one region) improves

agreement with the measurement relative to the results with the initial closure coef-
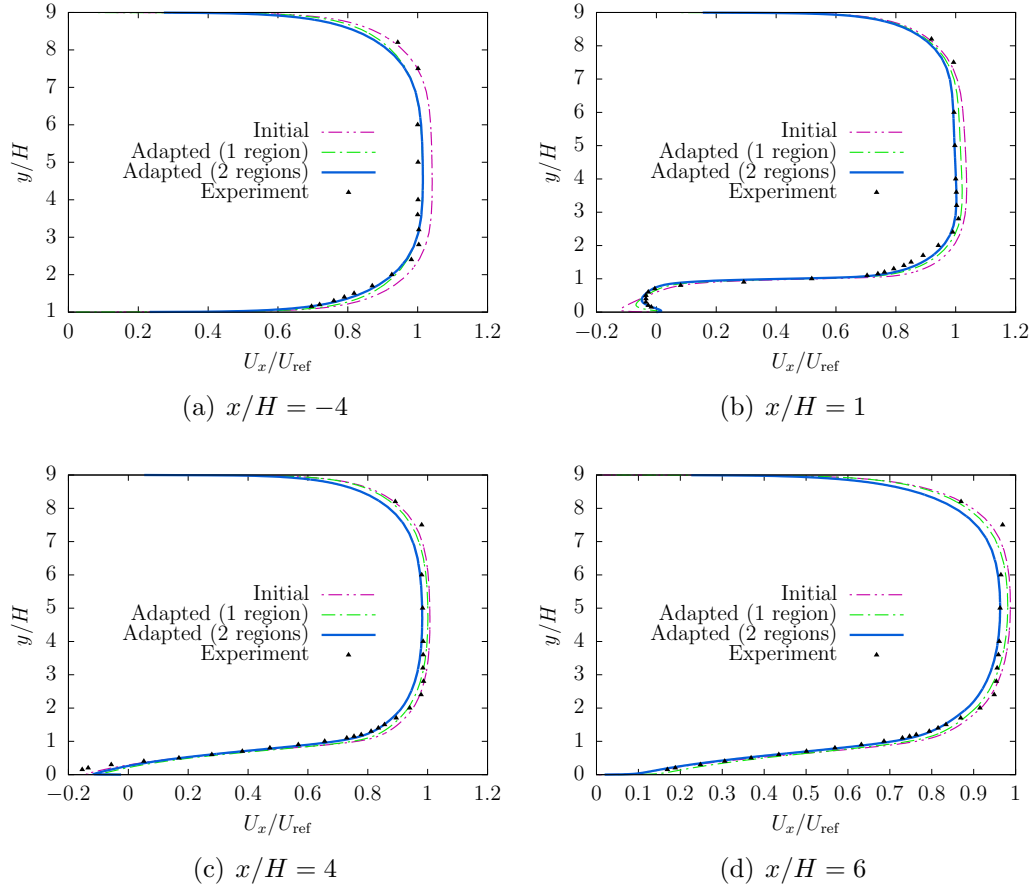
Figure 4.11: Mean stream-wise velocity U_x profiles for the backward-facing step at 4 cross sections: (a) $x/H = -4$, (b) $x/H = 1$, (c) $x/H = 4$, and (d) $x/H = 6$. Results are shown for the D-DARK model with the initial and adapted closure coefficients (1 and two segmentation regions), and for the measurement data, which are stream-wise velocities at 100 locations [2, 3]. For the 2-region case, the segmentation threshold is $G_{st} = 15$.

ficient. Notably, the flow profile at $x/H = 1$, shown in Fig. 4.11 (b), for the adapted D-DARK model captures the flow reversal. Comparing Fig. 4.10 (b) to Fig. 4.10 (a), we note that the adapted D-DARK model produces a longer recirculation region than the initial model, where the re-attachment is at approximately $x/H \approx 6.5$ rather than $x/H \approx 6$. In addition, the secondary recirculation near the face of the step is also larger. These topological differences between the initial and adapted D-DARK model

flows are reflected in the modeled surface-pressure coefficient

$$C_{\mathrm{p}} = \frac{p - p_{\mathrm{ref}}}{0.5\rho U_{\mathrm{ref}}^2}, \tag{4.25}$$

and surface-friction coefficient

$$C_{\mathrm{f}} = \frac{\tau_w}{0.5\rho U_{\mathrm{ref}}^2}, \tag{4.26}$$

where $p_{\mathrm{ref}} = 101.325$ Pa is the reference pressure taken at the location of U_{ref}. reference pressure Figure 4.12 shows the initial and adapted surface pressure and surface friction on the wall (at $y/H = 0$ or $y/H = 1$) for the D-DARK model. In addition, Fig. 4.12 shows experimental surface-pressure and surface-friction data, which is published in [2, 3]. These surface-pressure and surface-friction data are distinct from the mean stream-wise velocity data $\boldsymbol{\phi}_{\mathrm{m},1}, \ldots, \boldsymbol{\phi}_{\mathrm{m},100}$ used by the adaptation algorithm; however, all data is from the same experiment. Figure 4.12 shows that the adapted D-DARK model improves agreement with the data relative to the initial model. Specifically, the improvement from adaptation is noticeable in the surface pressure downstream of the reattachment point and, importantly, downstream of the last measurement location. Furthermore, adaptation improves agreement in the wall shear stress throughout the domain.

Figure 4.13 shows that the cost with the initial closure coefficients is $J(\boldsymbol{\theta}_0) = 1.07$, whereas the cost with the adapted closure coefficients (with one region) is $J(\boldsymbol{\theta}_{n_{\mathrm{f}}}) = 0.96$. Thus, adaptation reduces the cost by approximately 10%.

Next, we investigate using different adaptive closure coefficients in different spatial locations of the flow to reduce the error between the adapted D-DARK model and the measurement data. We segment the flow using the magnitude of the dimensionless velocity gradient G given by (4.24). As shown in Fig. 4.14, segmenting the flow into 2 regions with the segmentation threshold G_{st} of approximately 15 minimizes the converged cost, with similar behavior as observed for pipe flow.
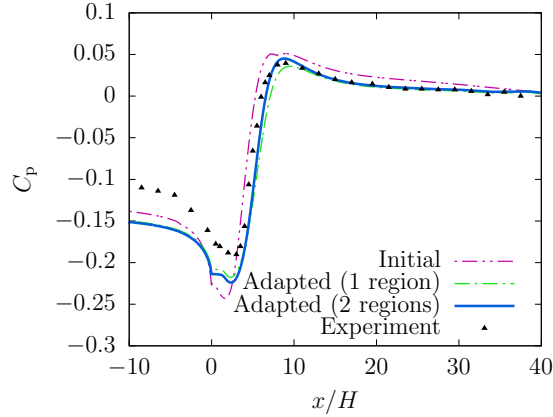
(a) Surface-pressure coefficient
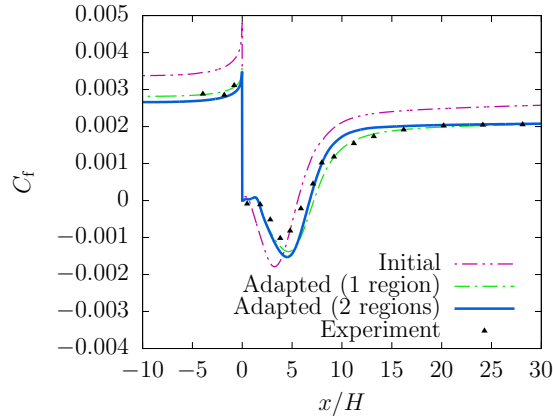
(b) Surface-friction coefficient

Figure 4.12: Surface-pressure coefficient and surface-friction coefficient for the backward-facing step. Results are shown for the D-DARK model with the initial and adapted closure coefficients (1 and two segmentation regions). The experimental surface-pressure and surface-friction data are published in [2, 3]. For the 2-region case, the segmentation threshold is $G_{\mathrm{st}} = 15$.

To investigate further flow segmentation, we set a first segmentation threshold at 15 and conduct a parametric study where a second segmentation threshold is varied across 8 orders of magnitude. As shown in in Fig. 4.14, the converged cost with 3-region segmentation is not significantly lower than that with 2-region segmentation; this trend is also similar to that observed with the pipe flow.

For the 2-region segmentation results, the D-DARK model is initialized with standard values for the closure coefficients [10] in both regions, and the model adapts the
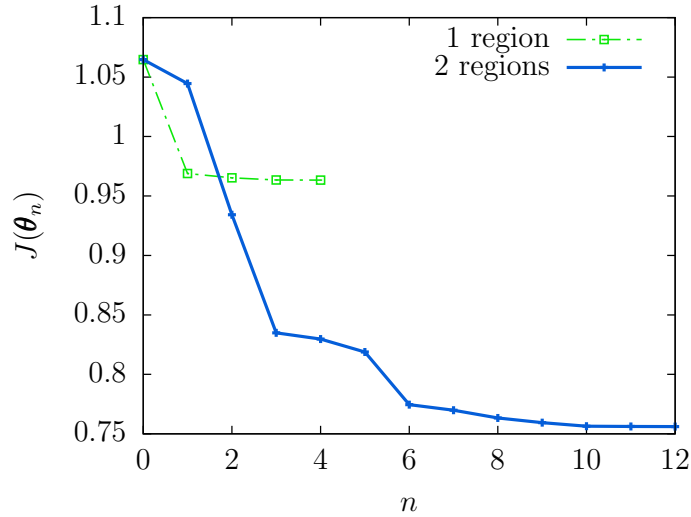
Figure 4.13: Cost J as a function of adaptation step n for the backward-facing step. For the 2-region case, the segmentation threshold is $G_{\mathrm{st}} = 15$.
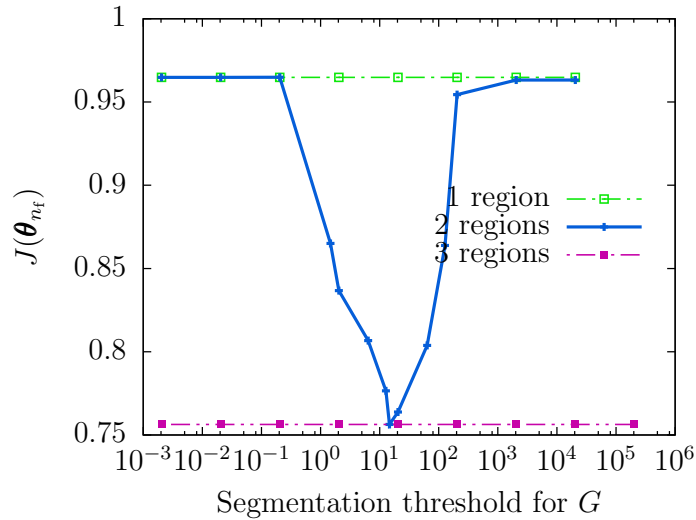
Figure 4.14: Cost J as a function of segmentation threshold for the backward-facing step. For the 3-region case, the first segmentation threshold is 15.

closure coefficients until the cost J converges, which occurs after $n_{\mathrm{f}} = 12$ steps. The initial and adapted closure coefficients are in Table 4.5. On step $n = 9$, the constraint (4.3) was enforced by bisecting the adaptive step size; see (4.20)–(4.22) for details. On this step, the unconstrained ratio β^*/β was less than 0.9; however, bisecting the
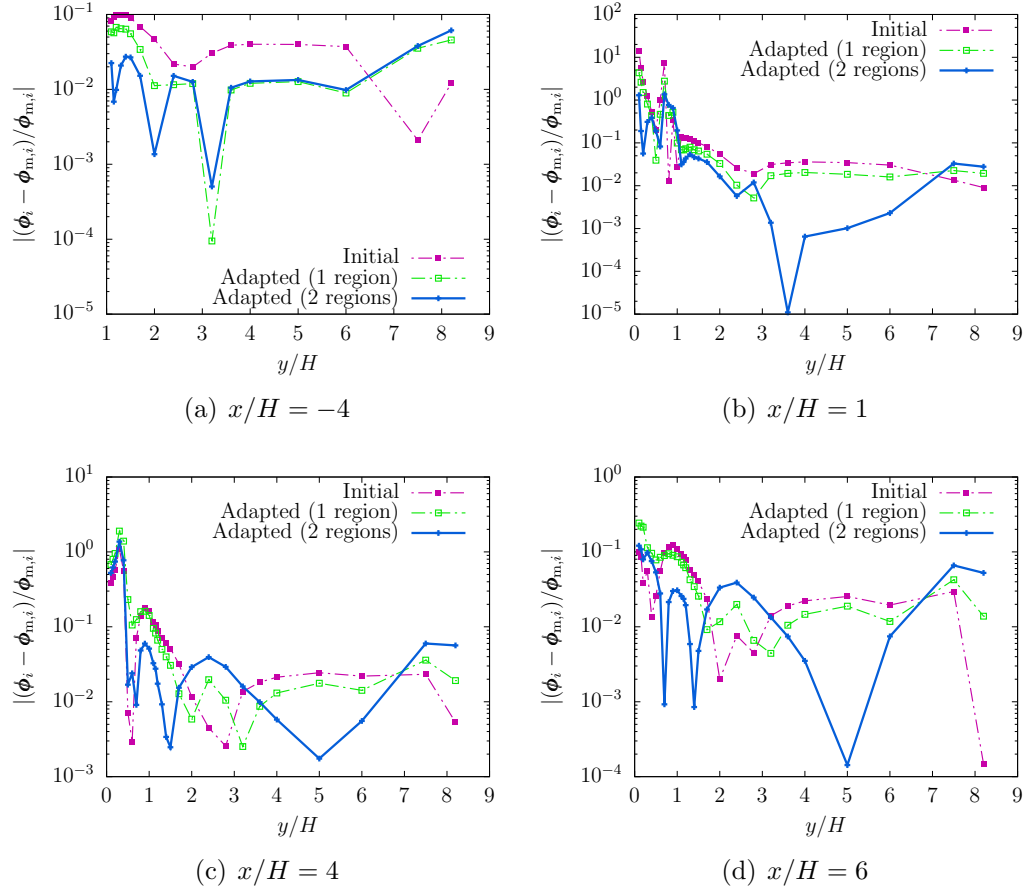
Figure 4.15: Normalized mean stream-wise-velocity error between the D-DARK model and the measurement data, which are stream-wise velocities at 100 locations [2, 3]. Results are shown for the D-DARK model with the initial and adapted closure coefficients (1 and 2 segmentation regions) at 4 cross sections: (a) $x/H = -4$, (b) $x/H = 1$, (c) $x/H = 4$, and (d) $x/H = 6$. For the 2-region case, the segmentation threshold is $G_{\mathrm{st}} = 15$.

adaptive step size enforced the constraint (4.3). Moreover, on step $n = n_{\mathrm{f}} = 12$, the constraints (4.1), (4.3), (4.9), and (4.10) were satisfied without bisecting the adaptive

Table 4.5: D-DARK closure coefficients for the backward-facing step with segmentation.

	σ_k	σ_ω	β	β^*	α
Initial	0.5000	0.5000	0.07200	0.09000	0.5200
Adapted ($G > G_{\mathrm{st}}$)	0.5004	0.4995	0.08868	0.07982	0.5206
Adapted ($G \leq G_{\mathrm{st}}$)	0.5002	0.4998	0.06843	0.09231	0.5186

step size.

The flow topology for the converged D-DARK model with 2-region segmentation, where $G_{st} = 15$, is shown in Fig. 4.10 (c). Together, Figs. 4.10 (b) and (c) illustrate relatively few differences between the converged D-DARK model with one region and the converged D-DARK model with 2 regions. However, the mean stream-wise velocity profiles in Fig. 4.11 show that the converged D-DARK model with 2 regions improves agreement with the measurement—both in the recirculation region and in the bulk flow region of the channel. Two-region segmentation also improves agreement between the measured and modeled C_p and C_f as shown in Fig. 4.12.

Figure 4.15 shows the normalized mean stream-wise-velocity error $|(\phi_i(\theta_n) - \phi_{m,i})/\phi_{m,i}|$ at each location i with the initial (i.e., $n = 0$) and adapted (i.e., $n = n_f$) closure coefficients with 1-region and 2-region segmentation. As shown in Fig. 4.15, the initial closure coefficients result in an average normalized error of approximately 40% between the measured and simulated mean velocities. In contrast, the adapted closure coefficients with 1-region and 2-region segmentation result in average normalized errors of approximately 24% and 12%, respectively.

Figure 4.13 shows that the converged cost with 2-region segmentation is $J(\theta_{n_f}) = 0.76$. Note that 2-region segmentation for the backward-facing step reduces the converged cost by a factor of 21% relative to the 1-region converged cost. In contrast, the 2-region segmentation for the pipe flow reduces the converged cost by a factor of 87% relative to the 1-region converged cost. Thus, the flow segmentation provided less improvement for the more complex geometry of the backward-facing step.

The D-DARK model (both 1-region and 2-region) reduces the cost J and in the process, captures key features of the measurement, specifically, within the reversed flow region downstream of the step, which are not captured by the standard k-ω closure coefficients proposed in [10]. This results in improved agreement in the derived pressure and friction coefficients, although the accuracy of the friction factor

of the segmented D-DARK simulation is reduced in the pressure recovery region.

4.6.4   NACA 0012 airfoil

The pipe-flow and backward-facing-step examples use the mean velocity to construct the D-DARK cost function. The backward-facing-step example demonstrates an improvement agreement in the surface-pressure and surface-friction coefficients even though adaptation is based on mean velocity. Frequently, surface parameters are the only available measurement data. To demonstrate D-DARK in such a situation, we consider a validation case in which the cost is constructed using surface-pressure data around a NACA 0012 airfoil. For this case, we use experimental data published in [4], which provides surface-pressure data at $N = 25$ measurement locations around the airfoil. Thus, for each $i = 1, \ldots, N$, the measurement $\phi_{\mathrm{m},i} \in \mathbb{R}$ is the surface pressure at the ith location.

The experiment in [4] was conducted with a reference Mach number of 0.15 and an airfoil cord $c = 1$ m. Thus, the Reynolds number based on chord length is approximately $\mathrm{Re}_c = 3 \times 10^6$. The boundary conditions are defined to match those of the experiment. Note that this validation case includes both laminar and turbulent regions of the flow field, which increases the complexity of the example. The upper and lower bounds (4.23) for the cost-function weights are computed using $\phi_{\mathrm{av}} = 101,325$ Pa, which is the far-field mean pressure. The turbulence intensity and eddy-viscosity-to-molecular-viscosity ratio at the inlet are $I_t = 5.2 \times 10^{-4}$ and $\mu_t/\mu = 0.009$.

The computational mesh for this test case is that distributed by NASA [125]. This mesh consists of $57,344$ cells, and produces grid-independent results as determined through comparison with results from a similar mesh with $230,529$ cells. The computational mesh as well as the measurement locations are shown in Fig. 4.16. The far-field boundary is $500c$ from the airfoil, which minimizes the influence of the

far-field boundary on the flow near the airfoil.
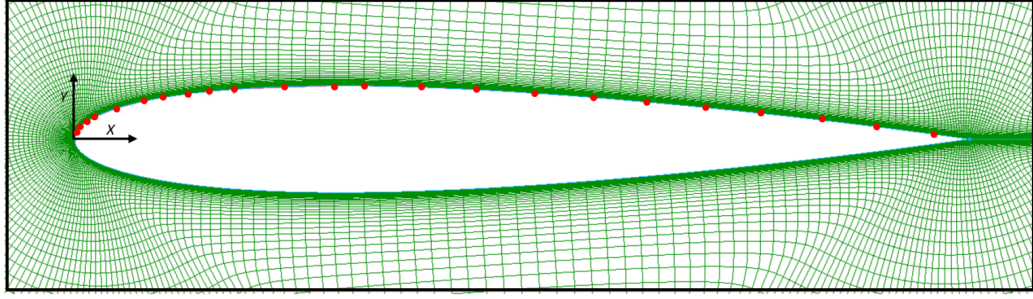
Figure 4.16: Computational mesh used for the NACA 0012 airfoil. The measurement locations are shown as the dots.

The D-DARK model implements 2-region segmentation, where the segmentation threshold is $G_{\mathrm{st}} = 15$, which is the approximately optimal threshold for the previous 2 validation cases. The model is initialized with standard values for the k-ω closure coefficients [10] in both regions, and the model adapts the closure coefficients until the cost J converges, which occurs after $n_{\mathrm{f}} = 10$ steps. The initial and adapted closure coefficients are in Table 4.6. The flow fields using the initial and adapted closure coefficients are illustrated in Fig. 4.17, where Ω_z is the z component of vorticity non-dimensionalized using c and U_{ref}. Differences are evident in the boundary layer development between the results using the initial and adapted closure coefficients. Specifically, the boundary layer and separated wake are noticeably thicker in the adapted case. For this test case, the constraints (4.1), (4.3), (4.9), and (4.10) were satisfied on each step of the adaptation without bisecting the adaptive step size.

Table 4.6: D-DARK closure coefficients for the NACA 0012 airfoil.

	σ_k	σ_ω	β	β^*	α
Initial	0.5000	0.5000	0.07200	0.09000	0.5200
Adapted $(G > G_{\mathrm{st}})$	0.5003	0.4998	0.1383	0.1258	0.5186
Adapted $(G \leq G_{\mathrm{st}})$	0.5004	0.4995	0.1038	0.1328	0.5206

Figure 4.18 shows the surface-pressure coefficient calculated from the experimental data and the surface-pressure coefficient calculated from the D-DARK model results
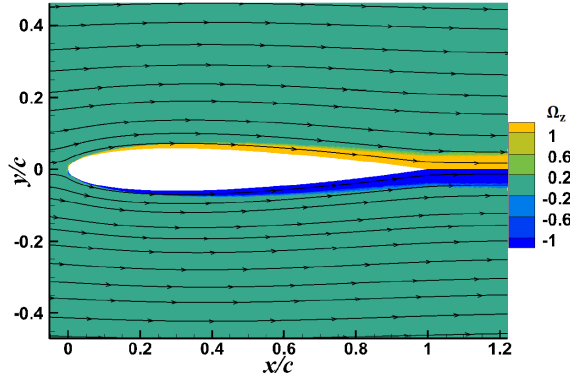
(a) Initial
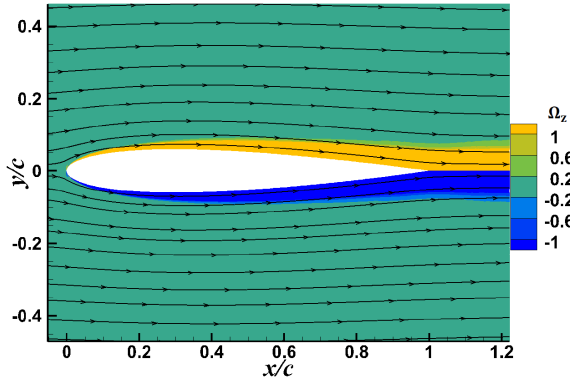
(b) Adapted (2 regions)

Figure 4.17: Vorticity contours and streamlines for the NACA 0012 airfoil. Results are shown for the D-DARK model with (a) the initial closure coefficients and (b) the adapted closure coefficients with 2 segmentation regions, where the segmentation threshold is $G_{\text{st}} = 15$.

with the initial and adapted closure coefficients. The difference between the data and the D-DARK results with the initial closure coefficients is noticeable, whereas the results with the adapted closure coefficients improves agreement with the data. For the $i = 1, \ldots, 25$ measurement locations, Fig. 4.19 shows the normalized error between the surface-pressure coefficient $C_{\text{p,m},i}$ calculated from the experimental data and the the surface-pressure coefficient $C_{\text{p},i}$ calculated from the D-DARK results. As shown in Fig. 4.19, the initial closure coefficients result in an average error of approximately 45% over the airfoil, but as large as 170% at the leading edge and 210% at the trailing edge. In contrast, the adapted closure coefficients result in an

88

average error of approximately 12% over the airfoil, and peak errors of 95% at the leading edge and 32% at the trailing edge. Thus, the average normalized error in the surface-pressure coefficient reduces by approximately 73%.

(a) x direction
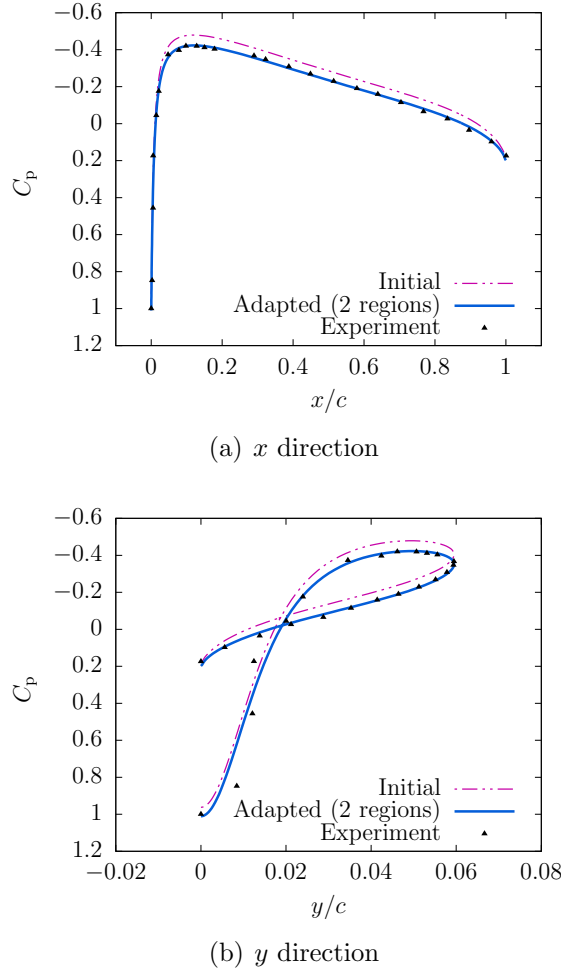
(b) y direction

Figure 4.18: Surface-pressure coefficient for the NACA 0012 airfoil along the (a) x direction and (b) y direction. Results are shown for the D-DARK model with the initial and adapted closure coefficients (2 segmentation regions with $G_{st} = 15.$), and for the measurement data, which are surface pressures at 25 locations [4].

Figure 4.20 shows the normalized mean pressure error $|(\phi_i(\boldsymbol{\theta}_n) - \phi_{m,i})/\phi_{m,i}|$ at each location i with the initial (i.e., $n = 0$) and adapted (i.e., $n = n_f$) closure coefficients. As shown in Fig. 4.20, the initial closure coefficients result in an average normalized error of approximately 0.10%, whereas the adapted closure coefficients

result in average normalized error of approximately 0.043%. Thus, the average normalized error in the absolute surface pressure reduces by approximately 57%. This case therefore demonstrates that the D-DARK model can improve agreement between measured and simulated results for cases where only surface parameters are available.

Note that the k-ω turbulence model does not necessarily predict transition to turbulence. However, the D-DARK model does recover the effects of transition as it adapts the coefficients to the measurement, whether transition effects are present or not.
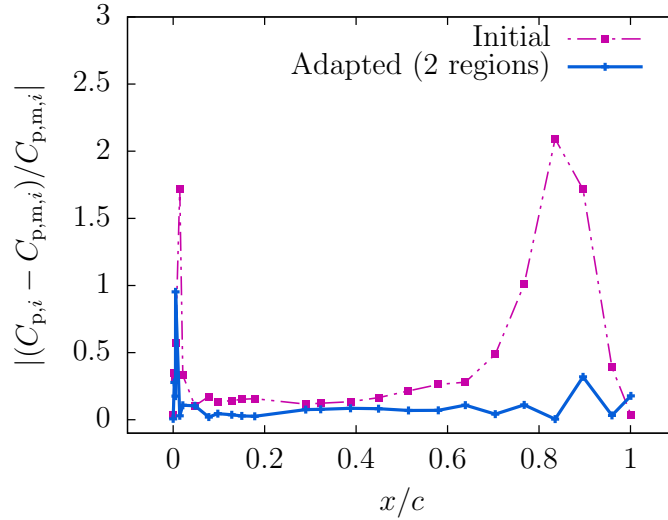
Figure 4.19: Normalized surface-pressure-coefficient error between the D-DARK model and the measurement data, which are surface-pressure coefficients calculated from absolute surface pressure data at 25 locations [4]. Results are shown for the D-DARK model with the initial and adapted closure coefficients (2 segmentation regions with $G_{\mathrm{st}} = 15$.).

4.7   Conclusions

The data-driven adaptive RANS k-ω (D-DARK) model is a new technique for simulating turbulent flow, where partial-but-incomplete measurement data is available. The D-DARK model automatically adapts the k-ω closure coefficients to improve
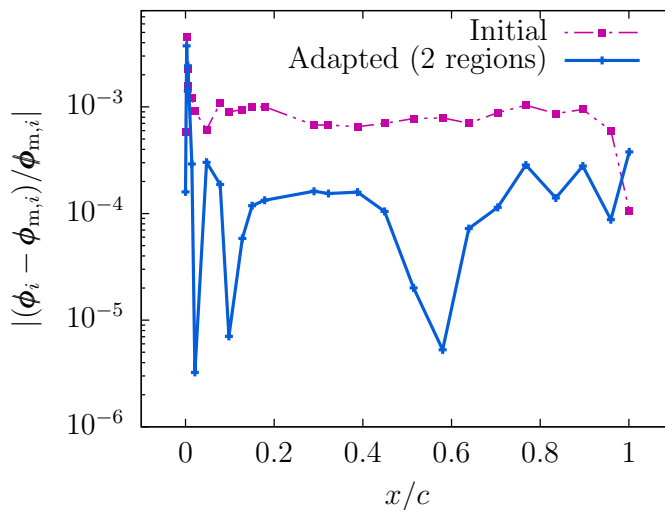
Figure 4.20: Normalized surface-pressure error between the D-DARK model and the measurement data, which are surface pressures at 25 locations [4]. Results are shown for the D-DARK model with the initial and adapted closure coefficients (2 segmentation regions with $G_{st} = 15$.).

accuracy of the CFD solution in comparison to the measurement data. For the three validation cases in this chapter, the D-DARK model improves agreement with experimental data in comparison to the results from a non-adaptive RANS k-ω model that uses standard values of the closure coefficients. Results from these validation cases suggest that the D-DARK model cost function and thus the accuracy of the adapted D-DARK solution is most sensitive to two of the k-ω closure coefficients, namely, β and β_*.

The D-DARK model is an alternative to high-resolution numerical simulations such as DNS, which require significant computing resources. The D-DARK method has potential application to pollution-dispersion prediction and the operation of wind-turbine fields, where the boundary conditions will be difficult to replicate exactly within simulation, but overall results can still be improved by model adaptation.

The D-DARK model presented here uses the k-ω closure model, and is therefore subject to its assumptions and limitations, such as the requirement of extensive mesh

refinement near the wall. The algorithm also relies on the calculation of an approximate gradient which increases the computation time when using complex closure equations, such as the k-ω model. However, the approach is not specific to the k–ω model and could be used in conjunction with other turbulence models or even other fluid physics that have coefficients to adapt [126]. Moreover, the D-DARK method can potentially be implemented in unsteady simulations, thus broadening its range of application.

Chapter 5 Retrospective Cost Adaptive k-ω Model

A real-time adaptive control technology, called retrospective cost adaptation (RCA), is applied to automatically adjust the closure coefficients of the unsteady Reynolds-averaged Navier-Stokes (URANS) k-ω turbulence equations. RCA approach has been successfully validated on numerous control applications that have significant transient behavior, which suggests that RCA is well suited for adaptation with unsteady flows. The RCA-URANS k-ω model is verified by a statistically steady test case (pipe flow) as well as two unsteady test cases: vortex shedding from a surface-mounted cube and flow around a square cylinder. The results of all cases demonstrate that the k-ω closure coefficients can be updated to match the measurement data. Specifically, the periodicity in the simulated unsteady flow is in good agreement with the phase-averaged experimental data. It is therefore concluded that the RCA-URANS k-ω model is able to improve the original k-ω model results by adapting to measurement data for both averaged steady and unsteady turbulent flows. Unless otherwise stated, all notation in this chapter is defined with in this chapter and specific to this chapter.

5.1 Introduction

The phenomenon of turbulence is innate to natural and engineered systems and, as a result, accurate modeling of its impact on fluid systems is critical for numerous engineering problems. Thus, turbulence simulation within the framework of computational fluid dynamics (CFD) has become an important tool for the design and analysis of fluid systems, especially with the improvement in availability and power of computational resources.

Among the most commonly used CFD approaches to turbulence, direct numerical simulation (DNS) produces the most accurate results, but still remains computationally expensive for high Reynolds number problems, with computational cost increasing as $\sim \mathcal{O}(Re^3)$. Large-eddy simulation (LES), Reynolds-averaged Navier-Stokes (RANS), and their hybrid method, detached-eddy simulation (DES), are alternatives to DNS; being less computationally expensive, but require some form of turbulence model to either account for inadequate resolution or to close the system of equations.

The RANS and LES equations are obtained from applying averaging and filtering processes, respectively, to the original Navier-Stokes equation. Although they use different derivation methods, the resulting formulas are similar with an additional dissipative term, referred to as the Reynolds stress (for RANS) or sub-grid scale stress (for LES) that introduce additional unknowns and therefore require additional equations to close the system of equations. Many different models have been proposed to achieve closure, with the models attempting to accurately determine the impact of the unresolved scales of turbulence on the resolved scales or mean flow. Common to these Reynolds stress, or sub-grid scale, models is that all of them introduce semi-empirical closure coefficients. Although certain assumptions and simplifications allow experimental data to be applied to estimate these coefficients, they tend to produce good results only in cases similar to the original experiments. When applied to more complex geometries or conditions which deviate from the canonical case, the accuracy of the simulation decreases correspondingly.

The goal of the current work is to provide an approach which allows applying limited experimental data towards identifying closure coefficients which will then accurately reconstruct the unmeasured portion of the flow field. For example, there are many instances where measurement data can be obtained from a finite number of discrete points inside the fluid domain. Rather than use this information to simply verify the simulation results, we present an approach which will autonomously identify

the closure coefficients that will provide the best agreement with the measurements.

To to achieve this objective, we build on prior work [111] and employ a data-driven model adaptation approach. Numerous other applications for adaptation and data-driven methods have previously been identified to improve the simulating accuracy of the turbulence models. For example, scale-adaptive simulations [112, 113, 58, 114] apply the von Kármán length scale to adapt the turbulence model to the scale of the mesh. Adaptive wall functions, which compensate for the simulation at the cell center nearest to the surface, have also be produced to adapt the wall function using the local Reynolds number [115] or the estimated location relative to the logarithmic layer [127, 117].

These approaches utilize the simulation results as a measure for driving the adaptation. However, instead of using simulated flow information for adaptation, data assimilation has long been implemented with non-RANS models to improve flow-field reconstruction or prediction (e.g., [69, 70, 71]). In meteorological modeling, measurement data from different locations and times can be assimilated into the computational fluid dynamics (CFD) model [73, 74]. As another example, [75] applies a multi-scale data assimilation method, which is based on stochastic super-parameterization, to predict different scales of turbulence fluctuations.

Recently, data-driven and data-assimilation approaches have also begun to be used with RANS models. For example, Duraisamy et al.[85] use machine learning tools, such as artificial neural networks and Gaussian process regression, to produce a model for an intermittency parameter introduced into the k-ω equations to better predict bypass transition in boundary layers. More recently high fidelity simulation and experimental data has been coupled with a new machine learning method, termed multiscale Gaussian process regression, to develop more accurate closure for the turbulence model [86]. The results highlight the potential of the machine learning method as a data-driven modeling tool. They also apply this new data-driven method

to transitional modeling [87]. Foures et al. [88] do not employ a closure model, but instead replace the Reynolds stress term in the RANS equation with a forcing function, and use the data to implement the forcing.

In this chapter, we apply the retrospective cost adaptive (RCA) method to determine the closure coefficients of the k-ω RANS model. The RCA method was initially designed to control linear systems but has been extended to treat nonlinear systems. One important benefit of RCA is that it does not require knowledge of the details of the system, in this case the RANS equations and boundary conditions which are producing the solution. Instead, it measures the response to an impulse introduced into the system and uses this information to tune the adaptation [128]. Although not utilized in the present work, RCA can also be applied to multi-input and multi-output systems [129]. The main benefit of the approach for finding closure coefficients is its ability to be applied to transient processes; this allows it to be implemented in unsteady simulations.

In addition to offering improved performance over the similar approaches which have been developed [111], the method can be applied to unsteady flow fields. The RCA method was initially designed for system control [130, 129, 131] and has here been adapted to determine the closure coefficients of the standard k-ω RANS model by minimizing a performance parameter that is built using information from prior time steps and limited measurement information. In the present work, we use either velocity or pressure measurements, extracted from either a baseline simulation or an experiment, to adapt the closure coefficients of an unsteady Reynolds-averaged Navier-Stokes (RANS) simulation. Here, closure coefficients of the k-ω two equation turbulence model are adapted, although the RCA approach is readily extended to other turbulence models.

5.2 Data-driven retrospective cost adaptation

The RCA-RANS k-ω model relies on known flow-field measurements (e.g., known values of velocity or pressure) at N locations in the flow to adapt the k-ω closure coefficients, which are required to solve Eqs. (3.28) and (3.29), and are given by

$$\theta(n) = [\,\alpha(n) \quad \beta(n) \quad \beta^*(n) \quad \sigma_k(n) \quad \sigma_\omega(n)\,]^{\mathrm{T}} \in \mathbb{R}^{l_\theta}. \tag{5.1}$$

Note that the closure coefficients $\theta(n)$ are a function of the time step n, and subject to the constraints described by (4.1), (4.3), (4.9), and (4.10). We use the term *measurement* to describe information about the flow field that is known *a priori* at N locations.

For $i = 1, \cdots, N$, let $\phi_{\mathrm{m},i}(n) \in \mathbb{R}^{l_i}$ denote the ith flow-field measurement, that is, the flow-field measurement at the ith location, and let $\phi_{\mathrm{s},i}(n) \in \mathbb{R}^{l_i}$ denote the simulated flow-field value at the ith location. For all $n \in \mathbb{N} \triangleq \{0, 1, 2, 3, \cdots\}$, we define

$$\Phi_{\mathrm{m}}(n) \triangleq \begin{bmatrix} \phi_{\mathrm{m},1}(n) \\ \vdots \\ \phi_{\mathrm{m},N}(n), \end{bmatrix} \in \mathbb{R}^{l_\Phi}, \quad \Phi_{\mathrm{s}}(n) \triangleq \begin{bmatrix} \phi_{\mathrm{s},1}(n) \\ \vdots \\ \phi_{\mathrm{s},N}(n), \end{bmatrix} \in \mathbb{R}^{l_\Phi}, \tag{5.2}$$

where $l_\Phi \triangleq \sum_{i=1}^{N} l_i$. We also define the *performance*

$$\zeta(n) \triangleq \Phi_{\mathrm{s}}(n) - \Phi_{\mathrm{m}}(n), \tag{5.3}$$

which is used to adapt $\theta(n)$.

Let $f(n) \in \mathbb{R}^{l_f}$ denote the feedback, that is, a vector of the simulated flow-field results (e.g., mean velocities, or pressure coefficients), which serve as external drivers for $\theta(n)$. For all $n \in \mathbb{N}$, the closure coefficients are given by

$$\theta(n) = \sum_{i=1}^{n_c} M_i(n)\theta(n-i) + \sum_{i=1}^{n_c} N_i(n)f(n-i) + L(n), \tag{5.4}$$

where n_c is a positive integer, $M_i(n) \in \mathbb{R}^{l_\theta \times l_\theta}$, $N_i(n) \in \mathbb{R}^{l_\theta \times l_f}$, and $L(n) \in \mathbb{R}^{l_\theta}$. We initialize Eq. (5.4) with $M_i(0){=}0$, $N_i(0){=}0$, and $L(0) \in \mathbb{R}^{l_\theta}$ as the initial vector of the

k-ω closure coefficients. For example, $L(0)$ can be the closure coefficients proposed in [10]. Next, Eq. (5.4) can be written as

$$\theta(n) = Q(n)\psi(n), \tag{5.5}$$

where

$$Q(n) = \begin{bmatrix} N_1(n) & \cdots & N_{n_c}(n) & M_1(n) & \cdots & M_{n_c}(n) & L(n) \end{bmatrix} \in \mathbb{R}^{l_\theta \times [n_c(l_f+l_\theta)+1]}, \tag{5.6}$$

$$\psi(n) = \begin{bmatrix} f(n-1) \\ \vdots \\ f(n-n_c) \\ \theta(n-1) \\ \vdots \\ \theta(n-n_c) \\ 1 \end{bmatrix} \in \mathbb{R}^{n_c(l_f+l_\theta)+1}. \tag{5.7}$$

To derive an update equation for the parameters $Q(n)$, which govern the closure coefficients, we define the *retrospective performance*

$$\zeta_{\mathrm{r}}(n) = \zeta(n) + \sum_{i=0}^{n_r} H_i[Q(n) - Q(n-i)]\psi(n-i) \tag{5.8}$$

where n_r is a positive integer, and $H_i \in \mathbb{R}^{l_\Phi \times l_\theta}$ is the ith impulse response coefficient from θ to ζ. It follows from Eq. (5.8) that the retrospective performance $\zeta_{\mathrm{r}}(n)$ is a surrogate measure for the performance $\zeta(n)$. More specifically, if the adaptive parameter $Q(n)$ is constant, then $Q(n-i) \equiv Q(n)$ and Eq. (5.8) implies that $\zeta_{\mathrm{r}}(n) \equiv \zeta(n)$.

Next, Eq. (5.8) can be expressed as

$$\zeta_{\mathrm{r}}(n) = \zeta(n) + \sum_{i=0}^{n_r} \left[\psi^{\mathrm{T}}(n-i) \otimes H_i \right] q(n) - \sum_{i=0}^{n_r} H_i \theta(n-i) \tag{5.9}$$

$$= \zeta(n) - \sum_{i=0}^{n_r} \Psi^{\mathrm{T}}(n) q(n) + H_i \theta(n-i), \tag{5.10}$$

98

where

$$q(n) \triangleq \operatorname{vec} Q(n) \in \mathbb{R}^{l_\theta[n_c(l_f+l_\theta)+1]}, \tag{5.11}$$

$$\Psi(n) \triangleq \sum_{i=0}^{n_r} \psi(n-i) \otimes H_i^{\mathrm{T}} \in \mathbb{R}^{l_\theta[n_c(l_f+l_\theta)+1] \times l_\Phi}, \tag{5.12}$$

where $\operatorname{vec} Q(n)$ is the vector formed by stacking the columns of $Q(n)$, and $\otimes$ denotes the Kronecker product.

Define the retrospective cost

$$J(n) \triangleq \sum_{i=0}^{n} \zeta_{\mathrm{r}}^{\mathrm{T}}(i)\zeta_{\mathrm{r}}(i) + (q(n) - q(0))^{\mathrm{T}}\Gamma(q(n) - q(0)), \tag{5.13}$$

where $\Gamma \in \mathbb{R}^{l_\theta[n_c(l_f+l_\theta)+1] \times l_\theta[n_c(l_f+l_\theta)+1]}$ is symmetric and positive definite. For each $n \in \mathbb{N}$, the retrospective cost J is minimized by

$$q(n+1) = q(n) - P(n)\Psi(n)\Omega(n)^{-1}\zeta_{\mathrm{r}}(n), \tag{5.14}$$

$$P(n+1) = P(n) - P(n)\Psi(n)\Omega(n)^{-1}\Psi^{\mathrm{T}}(n)P(n), \tag{5.15}$$

where $P(0) = \Gamma$ and

$$\Omega(n) \triangleq I + \Psi^{\mathrm{T}}(n)P(n)\Psi(n). \tag{5.16}$$

Then, $Q(n+1)$ is computed as

$$Q(n+1) = \operatorname{vec}^{-1} q(n+1) \in \mathbb{R}^{l_\theta \times [n_c(l_f+l_\theta)+1]}, \tag{5.17}$$

where vec^{-1} is the inverse vec operator, that is, $\operatorname{vec}^{-1}\operatorname{vec} Q(n) = Q(n)$. Note that Eqs. (5.15) to (5.16) are a recursive-least-squares algorithm. In summary, the RCA algorithm is given by Eqs. (5.5), (5.10) to (5.12), and (5.14) to (5.17).

If for any $n \in \mathbb{N}$, the closure coefficients $\theta(n)$ lie outside of the ranges given by Section 4.2, then $\theta(n)$ is projected to the boundary of the ranges given by Section 4.2. However, in all results presented in this chapter, the closure coefficients $\theta(n)$ never leave the ranges given by Section 4.2. For more information on projection of $\theta(n)$, see [132].

In practice, the RCA algorithm will not drive the performance $\zeta(n)$ exactly to zero. In other words, there is generally residual difference between the measurement $\Phi_{\mathrm{m}}(n)$ and the simulation $\Phi_{\mathrm{s}}(n)$ due to factors such as noise in the measurements, noise in the numerics, and the inability of a RANS k-ω model to match experimental data perfectly. However, if $\zeta(n)$ does not converge to zero, then Eq. (5.14) suggests that the parameter $q(n)$, which determines the closure coefficients $\theta(n)$, will continue to adapt, which can potentially lead to drift in both $q(n)$ and $\theta(n)$. Parameter drift is a well-known problem with adaptation algorithms [133].

To eliminate drift, we adopt a deadzone approach. Define the *modified retrospective performance*

$$\zeta_{\mathrm{r}}'(n) \triangleq \begin{cases} \zeta_{\mathrm{r}}(n), & \text{if } d(n) \geq \epsilon_0, \\[2mm] 0, & \text{if } d(n) < \epsilon_0, \end{cases} \tag{5.18}$$

where

$$d(n) \triangleq \sum_{i=0}^{N_d} \left| \|\zeta_{\mathrm{r}}(n-i)\|^2 - \|\zeta_{\mathrm{r}}(n-i-1)\|^2 \right|, \tag{5.19}$$

where N_d is a nonnegative integer, and $\epsilon_0 > 0$ is the threshold value. The deadzone Eq. (5.18) relating $\zeta_r(n)$ to $\zeta_r'(n)$ is shown in Figure 5.1, where the width of the
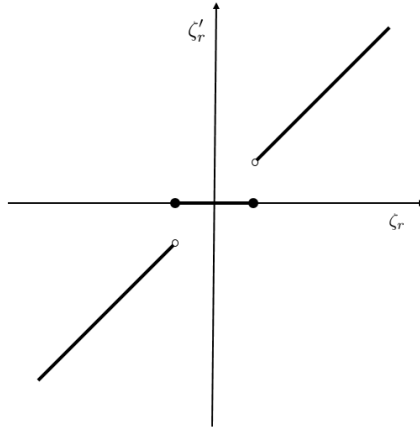
Figure 5.1: Dead zone illustration.

deadzone is determined from Eq. (5.19). Thus, the RCA algorithm used in this

chapter is given by Eqs. (5.5), (5.10) to (5.12), (5.18), (5.19), and

$$q(n + 1) = q(n) - P(n)\Psi(n)\Omega(n)^{-1}\zeta'_{\mathrm{r}}(n), \qquad (5.20)$$

where $P(n)$ and $\Omega(n)$ are given by Eqs. (5.15) and (5.16).

5.3 Verification and validation for steady flow

5.3.1 Verification for pipe flow

The RCA-RANS k-ω model is verified using the test case of air flow through a pipe. The radius of the pipe is $R = 0.06$ m, length of the pipe is $L = 2.4$ m, and the streamwise velocity at the inlet boundary is 9.1 m/s. The resulting Reynolds number, formed from the area-averaged velocity and pipe diameter, is approximately $80,000$.

The quarter-pipe grid used for the simulation is comprised of $225,000$ cells, and is shown in Figure 5.2. The grid-independence of the solution is determined through comparison with a $106,080$ cell grid. To avoid a situation where two specified measurement points are in the same cell, the finer grid is used. The turbulence intensity and eddy viscosity ratio of $I_t = 0.01$ and $\nu_t/\nu = 0.1$, respectively, are used for the initial condition of the whole domain as well as at the inlet. The gauge pressure of the outlet boundary is 0 Pa. A no-slip boundary condition is applied at the wall, a symmetry boundary condition is applied to the two azimuthal surfaces, and a zero-velocity gradient condition is applied at the outlet. Within this simulated flow field, 'measurement' points are selected at $z = 0.8L$, consisting of the $N = 24$ locations shown in Figure 5.2 spaced in the radial, r direction.

The selected measurement $\phi_{\mathrm{m},i}(n)$ for this case is the streamwise velocity U_z at the ith measurement point, taken from a simulation using a 'baseline' set of closure coefficients, provided in Table 5.1. The corresponding simulated value $\phi_{\mathrm{s},i}(n)$, is the streamwise velocity U_z at the ith measurement point of a simulation starting from the converged solution found using the 'initial' set of closure coefficients provided in
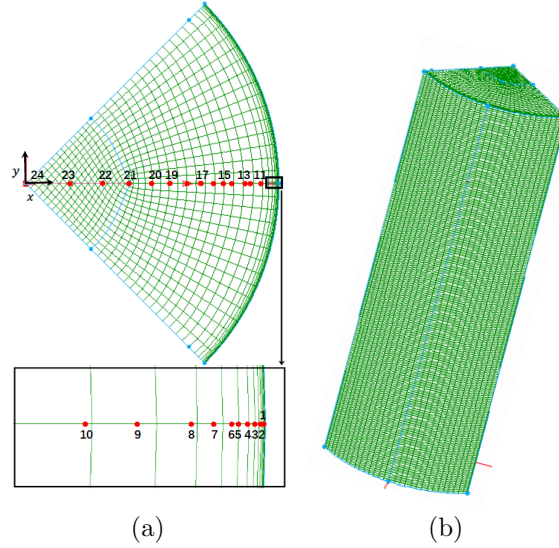
Figure 5.2: Computational mesh used for the pipe-flow verification and validation. The measurement locations are shown as red dots.

Table 5.1. Since the measurement points are not in the cell center where the value can be obtained directly from the solver, interpolation is needed. The cell-center value of cell containing the measurement points and the gradient are used to calculate the simulated value of the measurement points. This set of simulated value $\phi_{s,i}(n)$ is also used as the feedback, which means $f(n) = \Phi_s(n)$. Thus, $l_\Phi = 24$, $l_f = 24$, and $l_\theta = 5$.

Before implementing the RCA-RANS k-ω model, the impulse-response coefficients $H_0, H_1, \cdots, H_{n_r}$ at the measured points are determined. A steady simulation is performed using an initial set of closure coefficients and allowed to converge. Then, we impulse the closure coefficients, that is each closure coefficient is increased to unity for one-time step and returns back to the original value on the following time step. This process is performed on each closure coefficient independently. The difference between streamwise velocity U_z at the time steps following the impulse and the streamwise velocity U_z prior to the impulse is used to determine the response of the system and the impulse response coefficients $H_0, H_1, \cdots, H_{n_r}$ at each of the $N = 24$ measurement locations. Figure 5.3 shows sample impulse response of streamwise ve-

102

locity at every third measurement points. Following approximately 60 time-steps, the flow field returned to its unperturbed condition. Note that the impulse response of β and β^* is larger than that of the other three coefficients.
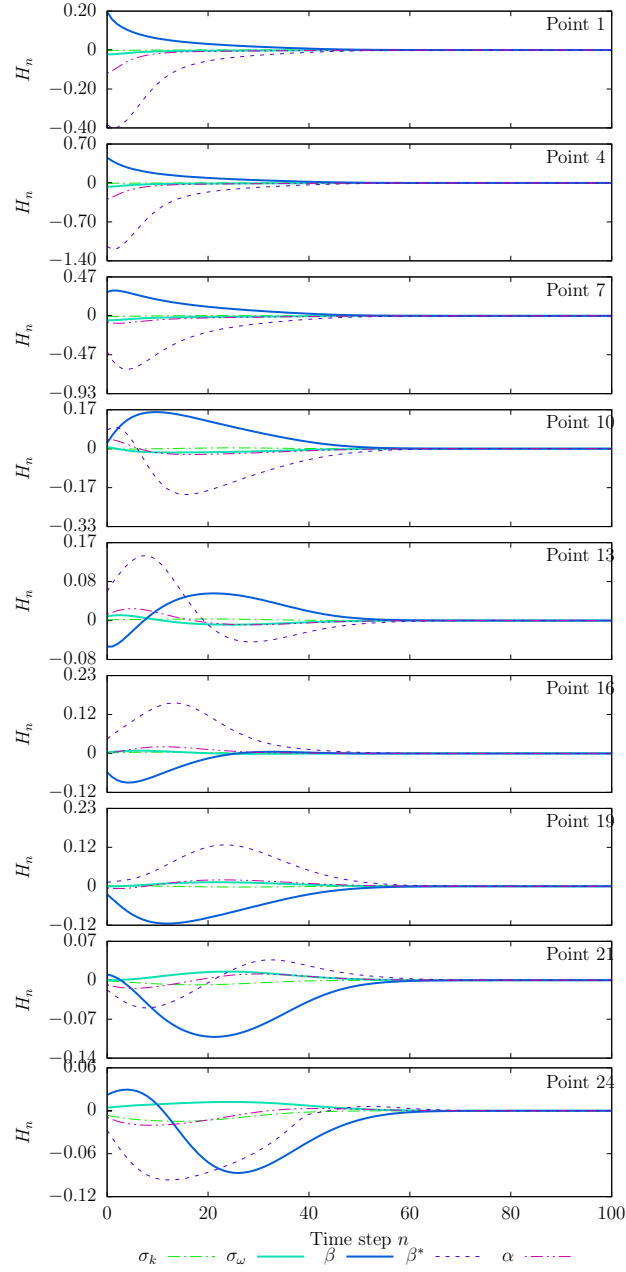
Figure 5.3: Streamwise velocity impulse response H_n of pipe flow case at selected radial locations. Location of measurement indicated in upper right of each subfigure.

From this impulse-response data, we select $n_r = 7$, which is a sufficient number

of steps to determine the initial direction of the impulse response.

The RCA algorithm is implemented with $n_c = 1$, and the initial conditions $M_1(0) = 0$, $N_1(0) = 0$, $L(0) = [0.4500, 0.4500, 0.08300, 0.07600, 0.4500]^\mathrm{T}$, and

$$P(0) = 10^{-20} \sum_{i=1}^{145} e_i e_i^\mathrm{T} + 10^{-5} \sum_{i=146}^{150} e_i e_i^\mathrm{T} \tag{5.21}$$

where $e_i \in \mathbb{R}^{150}$ is the ith column of the identity matrix. The last five diagonal elements of Γ are equal to 10^{-5}, which corresponds to $L(n)$. This value dictates how each coefficient can change for one adaptation step. If those five elements are too large, the adaptation will be underdamped and oscillate, if too small the adaptation will be overdamped and convergence times will be overly long.

As noted above, to test the RCA-RANS k-ω approach, a simulation is conducted in which the target flow field, the baseline case, is generated using a standard set of closure coefficients [10]. An additional simulation is run using the second set of closure coefficients, which is allowed to converge. These are then referred to as the 'Initial' conditions for the adaptation. The adaptation is then initiated, and allowed to converge to a third set of closure coefficients. The results following adaptation are referred to as the 'Adapted' case. The closure coefficients for the baseline simulation are compared to the initial value used, as well as the value of the closure coefficients following adaptation in Table 5.1.

Table 5.1: RCA-RANS k-ω model closure coefficients for the pipe-flow verification.

	σ_k	σ_ω	β	β^*	α
Baseline	0.5000	0.5000	0.07200	0.09000	0.5200
Initial	0.4500	0.4500	0.08300	0.07600	0.4500
Adapted	0.4500	0.4502	0.07351	0.09215	0.4504

The results show that two of the adapted coefficients, β and β^*, approached, but did not return to the baseline values. Interestingly, the other three coefficients are almost unaffected by the adaptation, demonstrating the coupling between coefficients
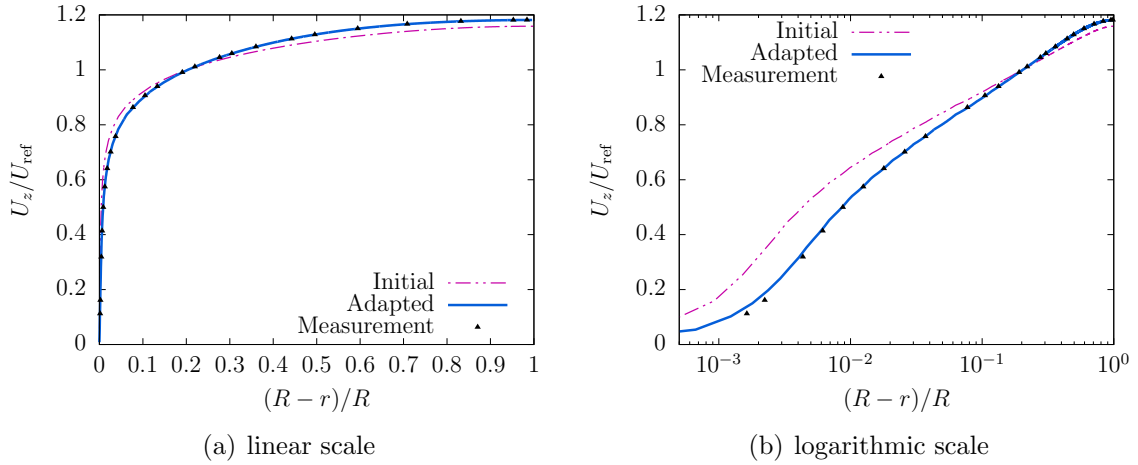
Figure 5.4: Mean streamwise velocity U_z profile for the pipe-flow verification at $z = 0.8L$ cross section.

and suggesting that multiple combinations of closure coefficient values may achieve the same result.

The agreement between the adapted and baseline simulations is demonstrated in Figure 5.4, which compares the profiles of streamwise velocity U_z normalized by the average velocity $U_{\text{ref}} = 9.1$ m/s. The profiles shown are from streamwise location $z = 0.8L$ and are those produced from the simulations using the initial closure coefficients and adapted closure coefficients. These velocity profiles are compared to the measurement points extracted from the baseline simulation. The improvement in agreement introduced by adaptation is clear, whereas the initial coefficients produce higher velocities near the wall relative to the measurements, and lower velocities in the free stream, the adapted coefficients are found to produce excellent agreement over 99% of the flow field, with only a slight overshoot in velocity near the wall. The resulting improvement can be seen from the overall error of 0.00434% found between the adapted simulation and baseline simulation, while the corresponding error between the initial simulation and baseline simulation is 1.16%.

The ratio of closure coefficient value to its original value are shown as a function
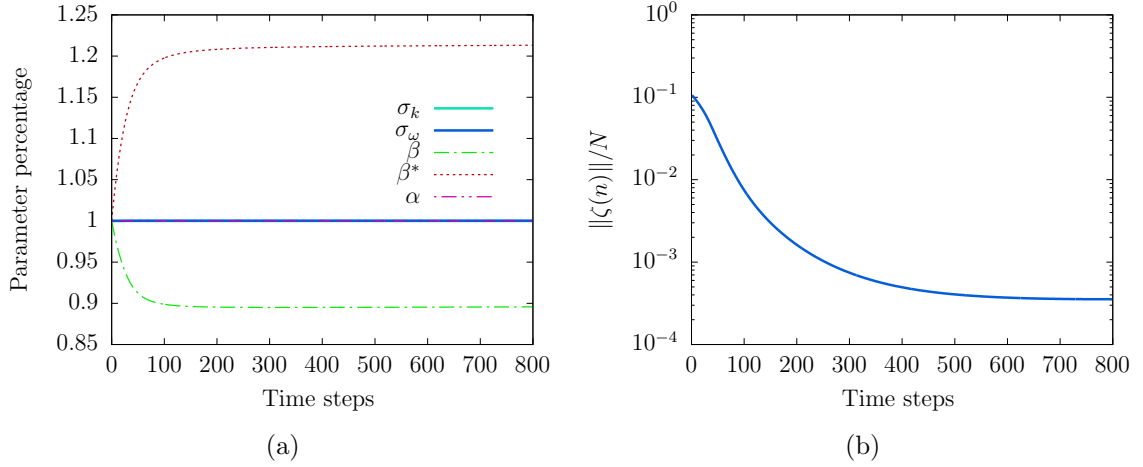
Figure 5.5: Curves of (a) ratio of closure coefficients to their initial value as a function of time step, and (b) performance to adaptation steps for pipe verification case.

of time step in Figure 5.5(a). This figure shows that, whereas σ_k, σ_ω and α have very little change, most of the improvement of the solution is through adaptation of β and β^*. These two coefficients change more than 10%, adjusting monotonically towards their final values. Figure 5.5 (b) shows the corresponding performance of the adaptation as measured through the averaged 2-norm of performance value, $\|\zeta(n)\|/N$. Through adaptation, the performance value drops from 0.1058 to 3.845×10^{-4}.

(a) Linear scale

(b) Logarithmic scale
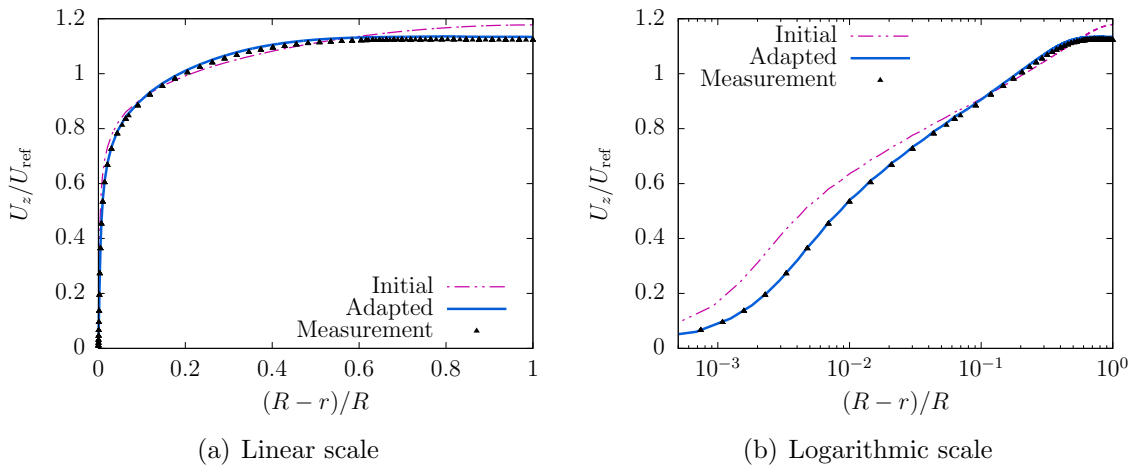
Figure 5.6: Mean streamwise velocity U_z profile for the pipe-flow verification at $z = 0.5L$ cross section.

Figure 5.6 shows the mean streamwise velocity U_z profile at $z = 0.5L$ cross section. Although this location is not used for adaptation, the adaptation improves agreement relative to the initial coefficient values initial result. To get a sense of the global improvement offered by the adaptation, the difference between the volume-averaged stream-wise velocity drops to 9.42×10^{-2} m/s from 2.07×10^{-1} m/s and the difference in maximum streamwise velocity drops from 1.75 m/s to 0.22 m/s. This improvement reflects that the quality of agreement is not limited to the measurement location.

These results thus demonstrate how the RCA-RANS k-ω model can successfully adapt the closure coefficient values to autonomously improve the simulation of steady flow fields when a measurement is available. Although the target coefficient values are not recovered completely, the approach does find values which reproduce the measured flow field.

5.3.2 Validation for pipe flow

The RCA-RANS k-ω model is validated using the same pipe flow case as Sec. 5.3.1. Again, the radius of the pipe is $R = 0.06$ m, length of the pipe is $L = 2.4$ m, and the streamwise velocity at the inlet boundary is 9.1 m/s. Reynolds number based on area-averaged flow rate and pipe diameter is approximately $80,000$, and the same boundary conditions used as described in Sec. 5.3.1. However, for the validation case, we used the experimental fully-developed pipe flow data of Ref. [1] at a set of $i = 1$ to 24 points as the measurement $\phi_{\mathrm{m},i}$; and we used simulated streamwise velocity U_z at the ith point retrieved from a simulation initiated with with the closure coefficients of [10] as $\phi_{\mathrm{s},i}$. The simulated value is also used as the feedback, which means $f(n) = \Phi_s(n)$. Thus, $l_\Phi = 24$, $l_f = 24$, and $l_\theta = 5$.

Since the coordinate points are not changed, the impulse response data $H_0, H_1, \cdots,$ H_{n_r} are the same as in Figure 5.3 at each of the $N = 24$ measurement locations. From the impulse-response data, we select $n_r = 7$.

107

The RCA algorithm is implemented with $n_c = 1$, and the initial conditions $M_1(0) = 0$, $N_1(0) = 0$, $L(0) = [0.5000, 0.5000, 0.07200, 0.09000, 0.5200]^{\text{T}}$, which are the standard [10] k-ω closure coefficients, and

$$P(0) = 10^{-20} \sum_{i=1}^{145} e_i e_i^{\text{T}} + 10^{-4} \sum_{i=146}^{150} e_i e_i^{\text{T}} \tag{5.22}$$

where $e_i \in \mathbb{R}^{150}$ is the ith column of the identity matrix. These last five diagonal values are bigger than that of the verification case, which resulted in the parameter values having more fluctuations during adaptation. The standard closure coefficients[10] are used as the initial closure coefficients

At the beginning of the adaptation, the closure coefficients are set equal to the initial values provided in Table 5.2 and the solution allowed to converge. Also shown in Table 5.2 are the converged values of the coefficients as a result of adaptation. As with the verification case, σ_k, σ_ω and α had only small changes during adaptation, whereas β and β^* change by more than 5%, and appear to be more sensitive than other closure coefficients. For this case, the ratio of β^* and β changes from 1.25 to around 1.08.

Table 5.2: RCA-RANS k-ω closure coefficients for the pipe-flow validation.

	σ_k	σ_ω	β	β^*	α
Initial	0.5000	0.5000	0.07200	0.09000	0.5200
Adapted	0.5001	0.5000	0.07630	0.08219	0.5204

Despite this relatively small change in the coefficient values, there is a measurable improvement in the agreement between the simulation and measurement values. Figure 5.7 compares the streamwise velocity at $z = 0.8L$ determined from the initial and adapted closure coefficients at the $0.8L$ cross-section to the experimental data normalized by the average velocity $U_{\text{ref}} = 9.1$ m/s.

The results show how the adaptation improves agreement with the measurement data, particularly in the outer layer and most notably near the pipe centerline. There

(a) Linear axes   (b) Logarithmic axes
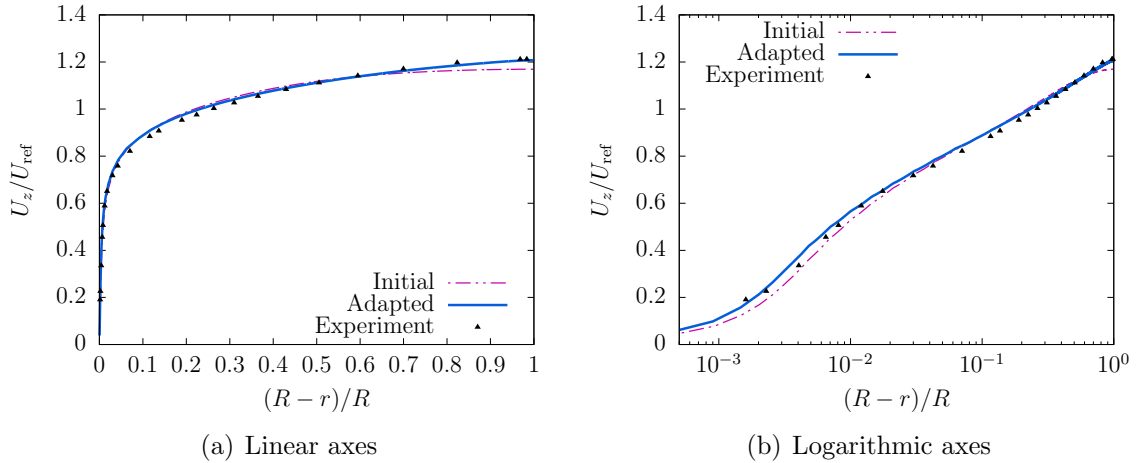
Figure 5.7: Mean stream-wise velocity U_z profile for the pipe-flow validation at $z = 0.8L$ cross section.

is still some over-prediction of velocity within the overlap region, although near the wall the adapted solution again improves agreement with measurements. It is found that additional gains in agreement could be achieved by further subdividing the flow field into two separate regions of adaptation (as done in Ref. [111]). However, this additional improvement is beyond the scope of the present chapter. We note that even without this additional step the adaptation process is able to produce a 35% improvement between measured and simulated velocities from only a 5% adjustment in closure coefficients.

The evolution of the the different closure coefficients as a function of the time step is shown in Figure 5.8(a). The corresponding improvement in the averaged 2-norm of performance is provided in Figure 5.8(b), which shows how the error between the experimental data and simulated velocity, $\|\zeta(n)\|/N$, changes with time step. After convergence, the adaptive process is stopped resulting in a 35% performance improvement. Also, the impact of reducing the diagonal elements of Γ is that the performance oscillates mildly for the first 100 time steps before slowly converging to the final values. Note, however, that 75% of the improvement in performance

occurs within the first few time steps. Thus adaptation could have been halted much earlier in the simulation while preserving considerable gains in agreement between measurements and the simulation.
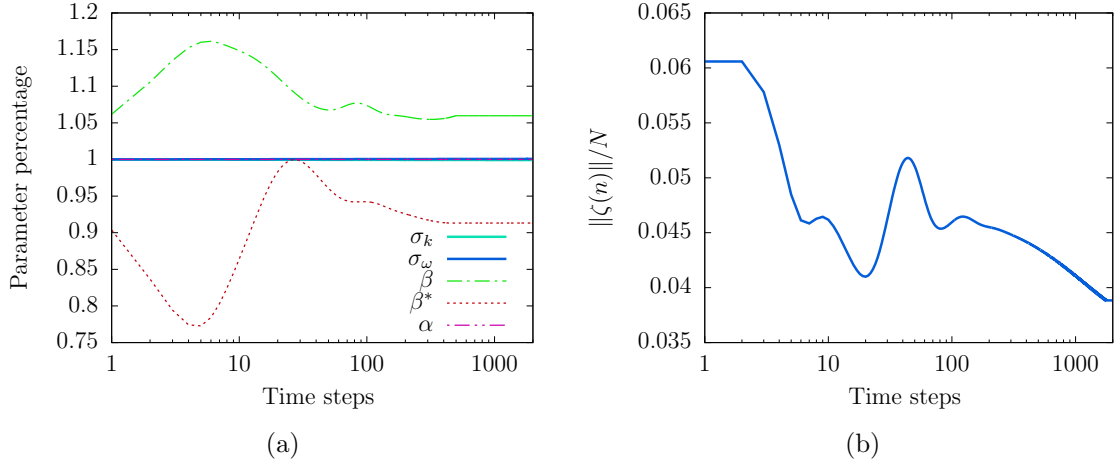
Figure 5.8: Curves of (a) percentage of closure coefficients to the original value and (b) performance to adaptation steps for pipe validation case.

5.4 Verification and validation for unsteady flow

5.4.1 Verification for flow over a surface-mounted cube in a channel

One advantage of the RCA-RANS k-ω approach is that it is readily applied to unsteady flows, provided that an unsteady measurement is available for adaptation. To demonstrate this capability, we apply RCA-RANS k-ω to the simulation of a three-dimensional surface-mounted cube in a fully-developed channel flow.

A sketch of this geometry is provided in Figure 5.9. This domain is divided into $364{,}021$ cells, with grid convergence verified through conducting a simulation using a similar grid with $562{,}349$ cells. The geometry and flow conditions are selected to match that of Ref. [5]. Thus the height of the cube is $h = 0.025$ m, and the average streamwise velocity at the inlet boundary is 23 m/s. The Reynolds number formed from h and mean inlet velocity is therefore approximately $40{,}000$. The inlet velocity

is uniform with boundary conditions set to be that of turbulence intensity $I_t = 0.04$ and eddy viscosity ratio $\nu_t/\nu = 10$ respectively. The gauge pressure at the outlet boundary is 0 Pa. Solid surfaces are set with no-slip boundary conditions, with the left and right sides being symmetry boundary conditions. A zero-normal-velocity gradient condition is applied at the outlet.

Figure 5.9: Sketches of top and side views of surface-mounted cube geometry adapted from Ref. [5]. Measurement points are indicated by numbered red dots.

For this geometry complex, three-dimensional, vortex shedding forms within the wake of the cube. Although complex, this shedding tends to occur at a fixed frequency resulting in a periodic flow field, making this problem suitable for unsteady RANS.

Nine points are chosen inside the fluid domain as measurement locations. These points are indicated in Figure 5.9 and are separated by $1h$ in the spanwise direction at the mid-point of the channel, $2h$ downstream of the back face of the cube. The selected 'measurement' value, $\phi_{\mathrm{m},i}(n)$, is the Z-axis velocity U_z at ith point of a simulation using the 'baseline' set of closure coefficients shown in Table 5.4. The simulated value $\phi_{\mathrm{s},i}(n)$ is the value of U_z at the ith point of a simulation initiated

using the 'initial' closure coefficients given in Table 5.4 and allowed to converge. The simulated value is also used for feedback, which means $f(n) = \Phi_s(n)$. Thus, $N = 9$, $l_\Phi = 9$, $l_f = 9$, and $l_\theta = 5$.

Figure 5.10 shows the impulse-response $H_0, H_1, \cdots, H_{n_r}$ of U_z the ith the measurement point. The process of getting impulse-response coefficients is identical to that used for pipe flow. Unlike the steady case, the impulse-response coefficients of the unsteady case show strong evidence of the periodicity intrinsic to the flow. The impulse-response coefficients do not disappear even after $12,000$ time steps, reflecting the sensitivity of the phase of the vortex shedding to the closure coefficients. Moreover, after the closure coefficients are impulsed, the phase of vortex shedding adjusts. Nevertheless, periodicity is recovered after $6,000$ time steps. From the impulse-response data, we select $n_r = 8000$. The impulse-response coefficients for β and β^* are larger than those of the other three closure coefficients. Thus, we can expect that the flow field will be more sensitive to changes in β and β^*. The RCA algorithm is implemented with $n_c = 1$, and the initial conditions $M_1(0) = 0$, $N_1(0) = 0$, $L(0) = [0.4000, 0.4500, 0.06200, 0.08000, 0.4500]^{\mathrm{T}}$, and

$$P(0) = 10^{-20} \sum_{i=1}^{70} e_i e_i^{\mathrm{T}} + 10^{-6} \sum_{i=71}^{75} e_i e_i^{\mathrm{T}} \qquad (5.23)$$

where $e_i \in \mathbb{R}^{75}$ is the ith column of the identity matrix.

As with the simulations of Sec. 5.3.1, we performed a simulation employing standard closure coefficients, and refer to this as the baseline case. The simulation is then repeated with a different set of closure coefficients (referred to as the initial values). Once the solution with the initial values converged, the adaptation is turned on, using the values of U_z of the 'baseline' case at the measurement locations as the target for adaptation.

The closure coefficients are presented in Table 5.3. As with the steady simulation, σ_k, σ_ω and α only changed slightly during adaptation whereas most of the influence on
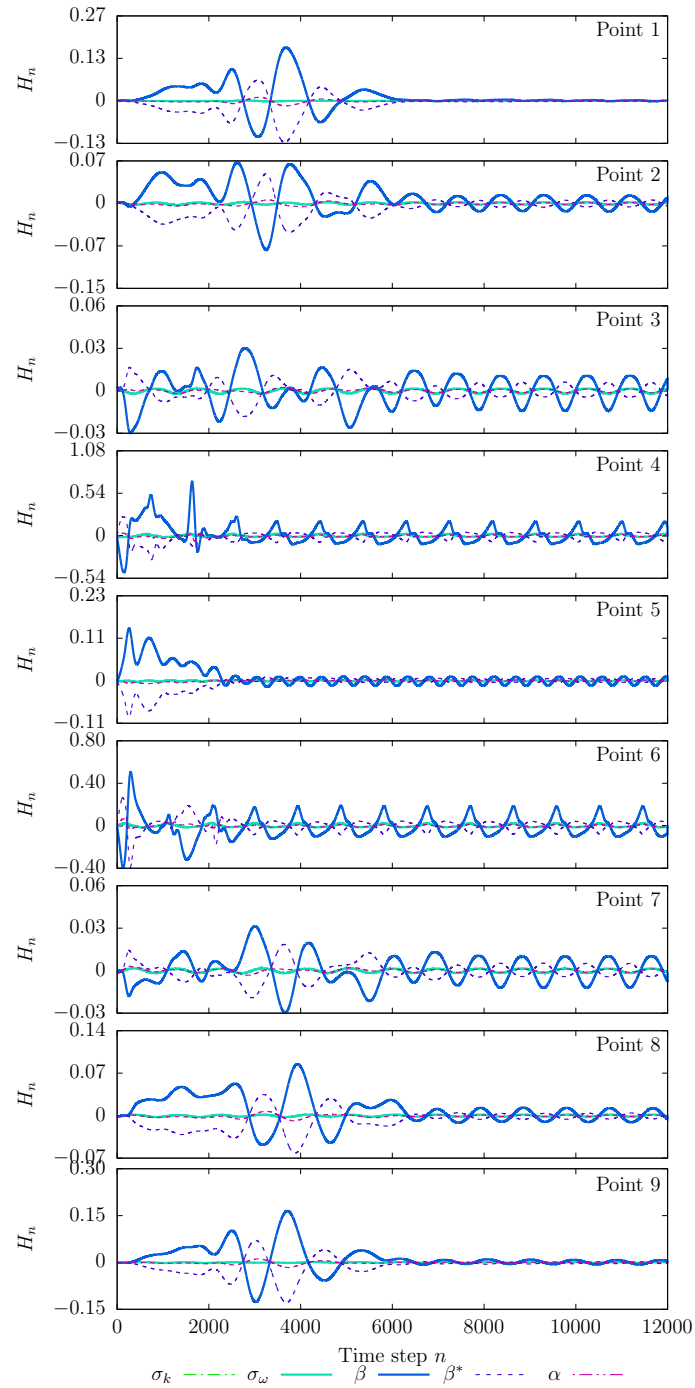
Figure 5.10: Impulse response of U_z for the 9 measured points used for the surface-mounted cube case.

the flow field is through modifications made to β and β^*. These coefficients changed by 7.2% and 7.1% respectively.

113

Table 5.3: Closure coefficients for the surface-mounted cube case.

	σ_k	σ_ω	β	β^*	α
Baseline	0.5000	0.5000	0.07200	0.09000	0.5200
Initial	0.4000	0.4500	0.06200	0.08000	0.4500
Adapted	0.4003	0.4482	0.05754	0.07431	0.4513

Figure 5.11 shows the time series of U_z for the initial closure coefficients at each of the nine measurement locations. The development of the velocities at these locations during adaptation, as well as the measurement values, are also shown in Figure 5.11.

The RCA method is started at the $40,000^{th}$ time step with one adaptation occurring at every ten-time steps. Following initiation of the adaptation, it took approximately $30,000$ time steps for the closure coefficients to approach their final values. During this time, the solution demonstrated large-scale oscillations. However, once the closure coefficients converged, the time series of velocity produced by the adapted simulation is very close to the measurement time series, with the phases of the vortex shedding synchronized. Note that, in Figure 5.11, Point 5 appears to have more discrepancy than other points, but this is due to the low value of the velocity in the middle of the wake. Hence this point did not have much contribution to the performance. The remaining points are found to produce a near perfect fit between the adapted results and the measurement. The overall error between the baseline simulation and the adapted simulation dropped to around 0.25% of the the average streamwise velocity at the inlet, while the corresponding error between the baseline simulation and the initial simulation is 2.26%.

The evolution of the closure coefficients is provided in Figure 5.13(a). As expected, the majority of the adaptation is through β and β^*. In this case, although their final values are not far from their initial values, they demonstrated large oscillations during the initial phase of adaptation; eventually settling down to their final converged values. The result of the solution is apparent in the averaged 2-norm of performance $\|\zeta(n)\|/N$, which is shown in Figure 5.13(b). This metric shows that the error dropped

relatively quickly. However, following this initial decrease, it took significantly longer for the adaptation to eliminate the phase shift between the measurement and the adapted velocities, apparent in the high-frequency oscillations of $\|\zeta(n)\|/N$. Thus, much of the convergence time is taken up correcting this phase difference.

Figure 5.12 compares the power spectrum of the U_z velocity at measurement point 4 in the surface-mounted cube case. The main frequencies of 'Initial', 'Measurement', and 'Adapted' cases are all equal to 51.23 Hz. However, the 'Initial' case has secondary frequency around 100 Hz. After adaptation, not just the secondary frequency is disappeared, the magnitude is also equal to the 'Measurement'.

This verification case shows that the RCA-RANS k-ω model can be applied to unsteady simulations. It can adapt the solution to match the magnitude and phase of the periodicity of the measurement. However, to precisely match the phase and amplitude of the oscillating flow, it took significantly more computational time than for the steady simulations.

5.4.2 Validation for flow over a square cylinder

To validate the capability of RCA-RANS k-ω model for unsteady simulation, we consider the case of a two-dimensional, square-cross-section, cylinder which results in the periodical shedding of von Kármán vortices. The geometry used for this simulation is presented in Figure 5.14(a), along with the flow characteristics designed to match the experimental conditions of Ref. [134]. Each edge of the cylinder is $h = 0.03$ m, and the average stream-wise velocity of the air at the inlet of the domain is uniform and set to 9 m/s. The Reynolds number based on this length and velocity is, therefore, $18,000$. The computational grid used is comprised of $81,932$ cells, as shown in Figure 5.14(b), and grid-independence is verified by comparison to a $123,524$ cell mesh.

The inlet conditions for turbulence intensity and eddy viscosity ratio are respectively $I_t = 0.01$ and $\nu_t/\nu = 1$. As shown in Figure 5.14, a no-slip boundary condition
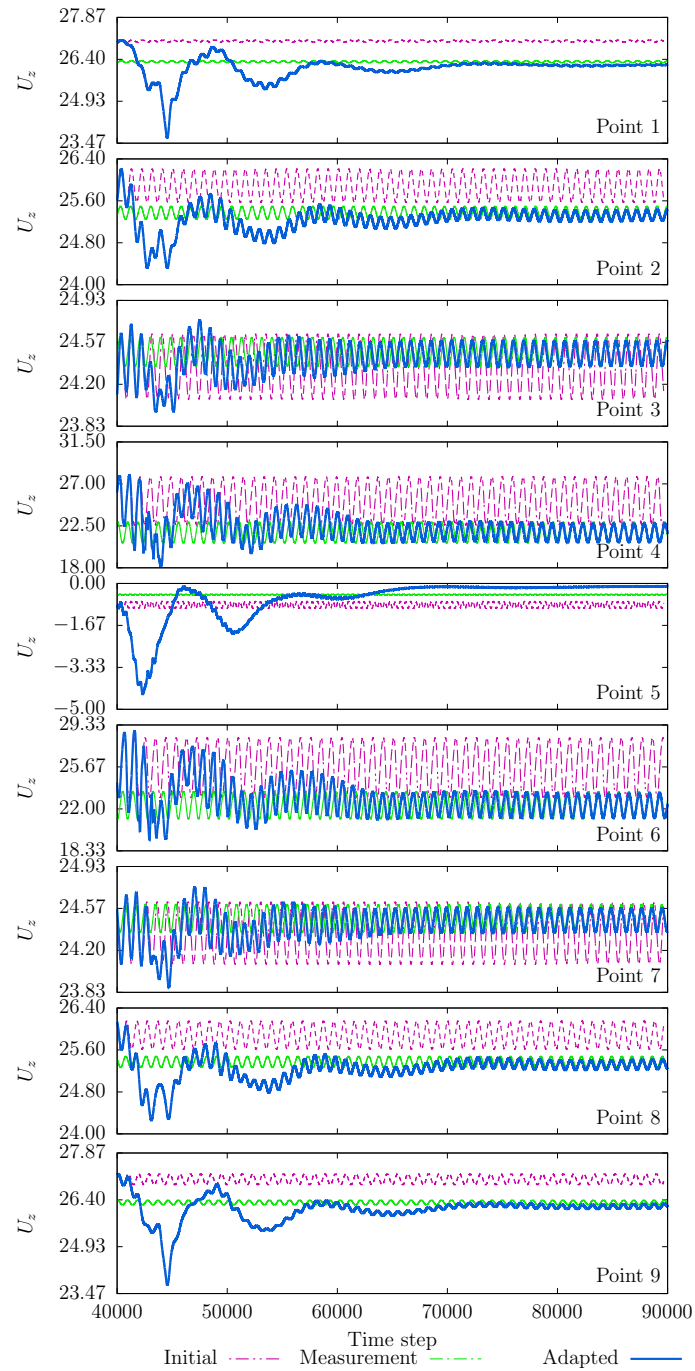
Figure 5.11: Comparison of simulation results for initial and adapted closure coefficients to corresponding measurement values.

is applied to all the solid surfaces, a symmetry boundary conditions are applied to the upper and lower boundary, and a zero normal-velocity gradient is applied to the
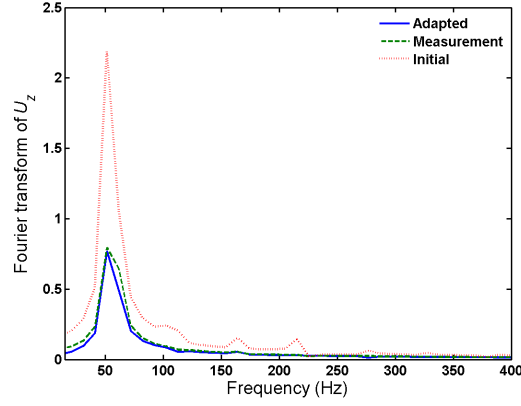
Figure 5.12: Fourier transform of U_z velocity at point 4 in surface-mounted cube case.
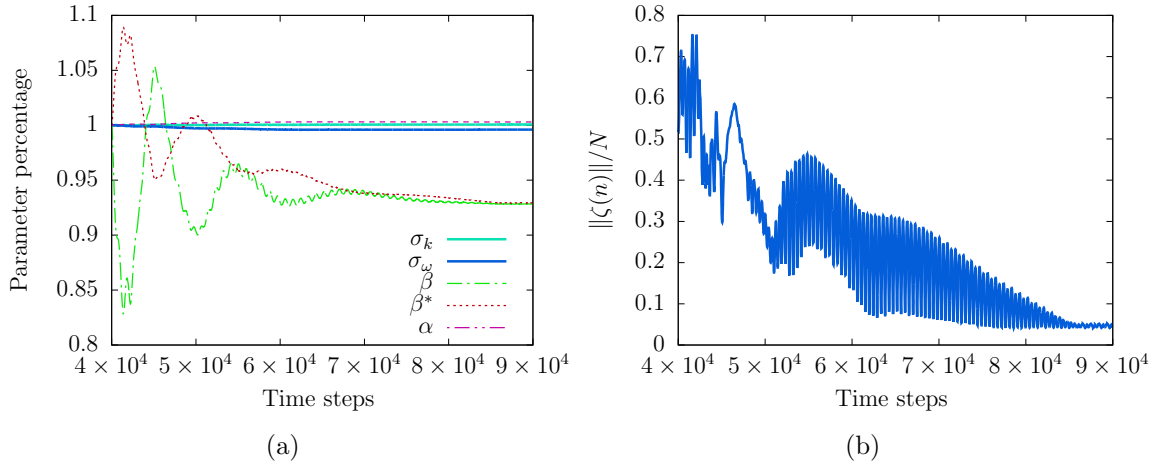
Figure 5.13: Curves of (a) percentage of closure coefficients to the original value, and (b) performance to adaptation steps for the surface-mounted cube case.

outlet. The gauge pressure at the outlet boundary is set to 0 Pa.

Two measurement points are selected, located centrally in the top and bottom faces, as indicated in Figure 5.14(a). At these locations, the phase-averaged pressure measurements of Ref. [134] are used to generate the target measurement conditions. This phase-averaged result, combined with the measured vortex shedding frequency, is used to reconstruct unsteady time series of pressure coefficient

$$C_P = \frac{p - p_{\text{ref}}}{0.5\rho U_{\text{ref}}^2}, \tag{5.24}$$
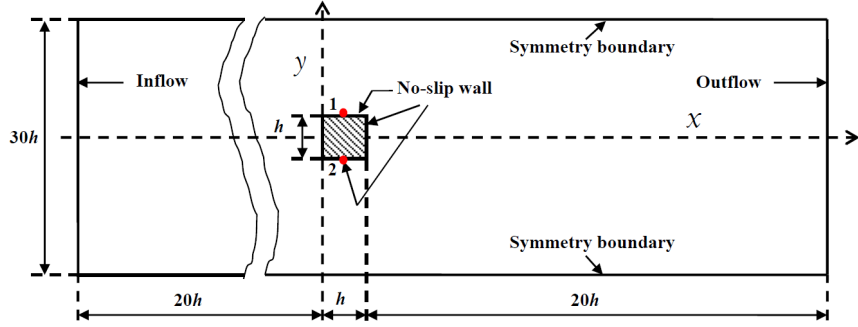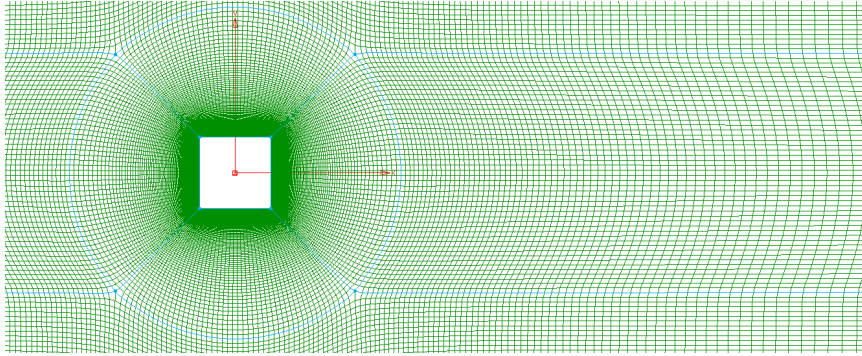
Figure 5.14: (a) Sketch of square-cylinder geometry and (b) corresponding detail of simulation mesh. The red points in (a) are the location of the measurement points.

where p is the local static pressure, ρ is the fluid density, free-stream static pressure $p_{\text{ref}} = 0$ Pa, and the free-stream average velocity U_{ref} is 9 m/s. These pressure coefficient time series at two locations, $i = 1$ to 2 on the top and bottom surface of the cylinder respectively, are used as the measurement values of the adaptation $\phi_{\text{m},i}$. The simulated value, $\phi_{\text{s},i}$, are then the time series of C_P retrieved from a simulation starting with initial closure coefficients. The simulated values are also use as feedback, which means $f(n) = \Phi_s(n)$. Thus, $N = 2$, $l_\Phi = 2$, $l_f = 2$, and $l_\theta = 5$.

Figure 5.15 shows the impulse-response coefficients $H_0, H_1, \cdots, H_{n_r}$ of C_P for $6,000$ time steps at the measurement points, where impulse-response coefficients are the difference between pressure coefficient after the impulse is introduced and the pressure coefficient prior to the impulse at ith point. The impulse-response coefficients

118

of β and β^* are again found to be higher than those of σ_k, σ_ω and α. Figure 5.15 also shows that the impulse caused a phase relative to the pre-impulse state. After 2,500 time steps, the magnitude of fluctuations did not change. Thus, $n_r = 2,500$ is deemed necessary for determining the RCA-RANS k-ω model conditions.
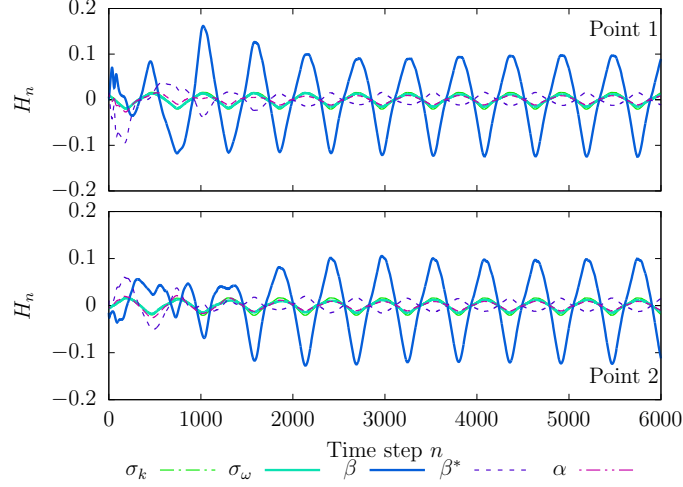
Figure 5.15: Impulse response H_n of pressure coefficients for 2 measured points of square-cylinder case.

The RCA algorithm is implemented with $n_c = 1$, and the initial conditions $M_1(0) = 0$, $N_1(0) = 0$, $L(0) = [0.5000, 0.5000, 0.07200, 0.09000, 0.5200]^{\mathrm{T}}$, and

$$P(0) = 10^{-20} \sum_{i=1}^{35} e_i e_i^{\mathrm{T}} + 10^{-6} \sum_{i=36}^{40} e_i e_i^{\mathrm{T}} \qquad (5.25)$$

where $e_i \in \mathbb{R}^{40}$ is the ith column of the identity matrix.

As with the prior validation case, the initial values of the closure coefficients are set to the standard values shown in Table 5.4. The RCA method is then initiated at the 40,000th time step. One adaptation is performed every ten-time steps. Following adaptation, the closure coefficients converged on the values presented in Table 5.4. As in the previous cases, σ_k, σ_ω and α only adapt a small amount, whereas most of the influence on the flow field is exerted through β and β^*. In this case β changes from 0.07200 to 0.08307 and β^* changes from 0.09000 to 0.08626 and the ratio between β^* and β changes from 1.25 to 1.04.

119

Table 5.4: RCA-RANS k-ω closure coefficients for the square-cylinder validation.

	σ_k	σ_ω	β	β^*	α
Initial	0.5000	0.5000	0.07200	0.09000	0.5200
Adapted	0.5000	0.5002	0.08307	0.08626	0.5199

The evolution of the closure coefficients and averaged 2-norm of performance during adaptation, as measured through $\|\zeta(n)\|/N$, are shown as Figure 5.16(a) and (b) respectively. Here, $\|\zeta(n)\|/N$ is the error between measured pressure coefficients and simulated pressure coefficients. After adaptation, performance drops from 0.56 to around 0.05 and fluctuated at a small range. Following convergence, some oscillations remained in the performance, suggesting adaptation is not able to eliminate the phase shift, unlike for the surface mounted cube case. However, the majority of improvements in performance occurred in just 2500 time steps, which corresponds to the largest change in β. β^*, conversely, adapts much more slowly and shows some oscillations during convergence.
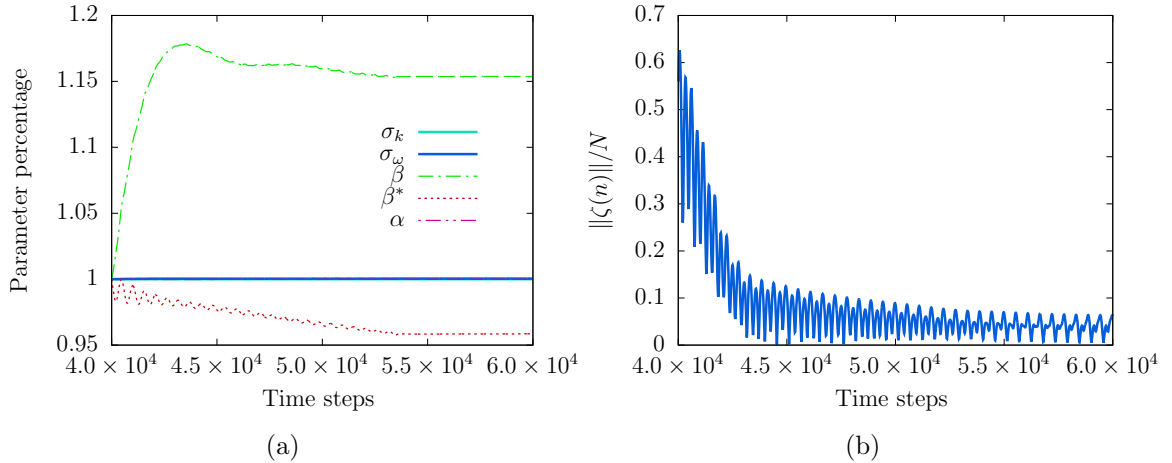
Figure 5.16: Performance and closure coefficients of verification case for applying RCA-RANS k-ω model on square-cylinder case.

The time series of C_P for the top and bottom faces of the cylinder are presented in Figure 5.17. In this figure, the reconstructed experimental time series of C_P alongside time series produced by the simulation with the initial closure coefficients as well as

120

the final adapted simulation are presented. There is a significant difference between the initial simulation and the measurement, with the initial simulation producing pressure oscillations almost double that of the measurement. The most likely reason for this being that the two-dimensional simulation is unable to capture the modulation of the shedding cycle due to three-dimensional effects [135]. However, as shown in Figure 5.17, the adaptation compensates for this difference after the first 2500 time steps of adaptation. The agreement between the simulation and measurement, in both the magnitude and phase, improves significantly, and once fully converged, only a slight difference in magnitude remains.
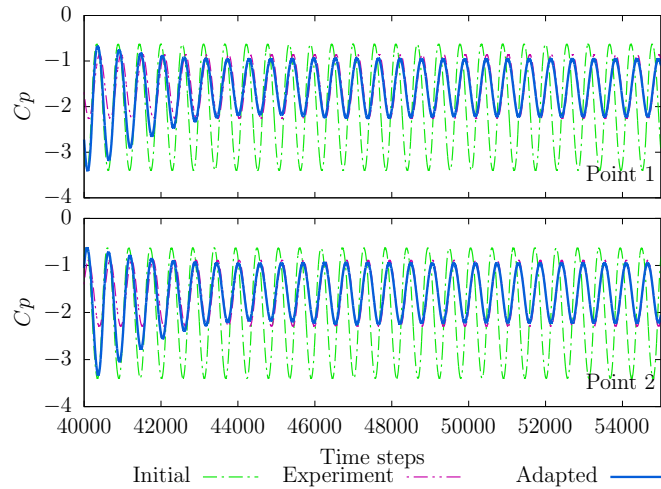
Figure 5.17: Compare the time series of 2 measured points of square-cylinder case.

The initial flow field after $45,000$ time steps is illustrated in Figure 5.18(a), and the adapted results at the same time step is shown in Figure 5.18(b). This figure shows an overall view of the periodic vortex-shedding flow field reproduced by simulation. Even though their time step is the same, their phase and magnitude are both different. The phase angle of the initial case is around $135°$ while the phase angle of the adapted result is around $180°$. The magnitude of C_P for the initial result is found to be significantly larger than the measurement at the same phase of shedding. After adaptation, the magnitude of C_P is very close to the measured one.

(a)

(b)
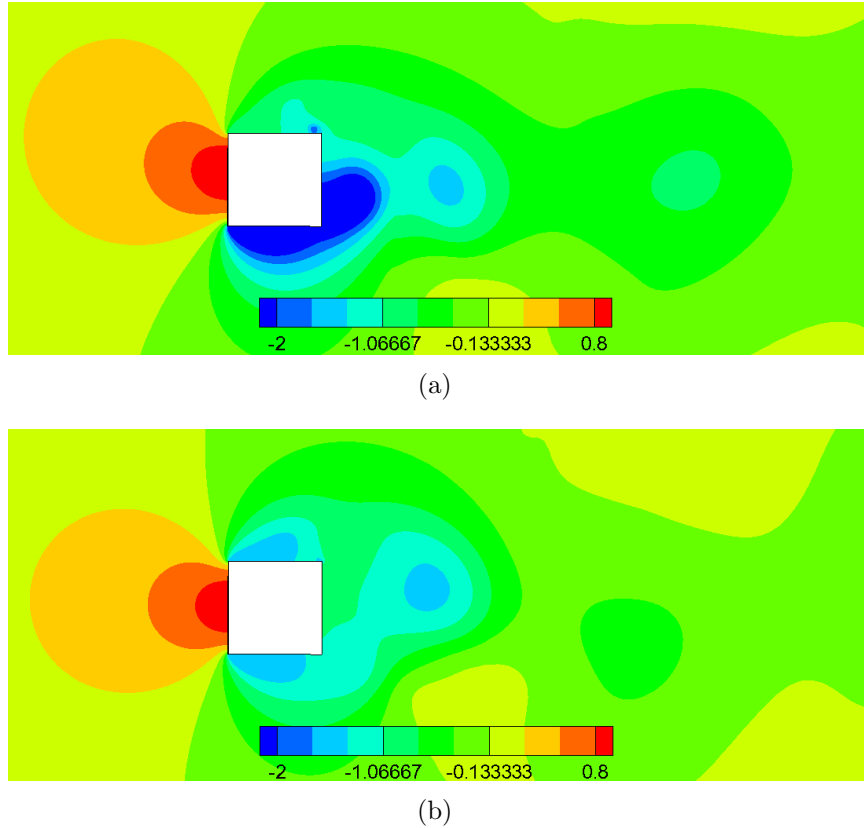
Figure 5.18: Isocontours of pressure coefficients C_P of the square-cylinder case, shown at the $45,000$th time steps for the (a) initial case, and (b) adapted case.

The power spectra determined through Fourier transform of the time series of C_P extracted from measurement point 1 are compared in Figure 5.19. The spectra confirm that although the initial simulation captured the frequency of the pressure fluctuations correctly at 4.08 Hz, it over-predicted the magnitude of these fluctuations. In addition, the initial simulation contained peaks at higher harmonic frequencies that are not present in the measurement. Following adaptation, the power spectrum of the simulated C_P almost exactly matched that of the measured C_P.

5.5 Conclusions

The RCA-RANS k-ω model is a new data-driven adaptive technique for steady and unsteady simulation of turbulence, where partial-but-incomplete measurement data
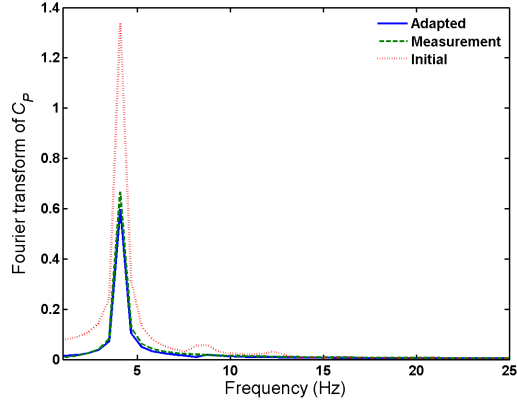
Figure 5.19: Fourier transform of C_p velocity at point 1 in square cylinder case.

is available. It can automatically adapt the closure coefficients of the k-ω model to improve the accuracy of the CFD solution in comparison to the measurement data. This model is verified and validated both on steady turbulence case and phase-averaged periodical turbulence flow in this chapter; the RCA-RANS k-ω model can decrease the error of experimental data in comparison to the results from a RANS k-ω model with standard closure coefficients. Results from these verification and validation cases suggest that the RCA-RANS k-ω model is most sensitive to two of the k-ω closure coefficients, namely, β and β^*. It proves that the periodicity of the turbulence can be controlled by the closure coefficients of the k-ω model.

The RCA-RANS k-ω model is an alternative to high-resolution numerical simulations such as DNS, which require significant computing resources. The RCA-RANS k-ω model has potential application to airborne pollution-dispersion prediction and the operation of wind-turbine fields, where the boundary conditions will be difficult to replicate exactly within the simulation, but overall results can still be improved by model adaptation. The RCA-RANS k-ω model can be implemented in unsteady simulations, thus broadening its range of application.

Chapter 6 Final Summary and Conclusions

6.1 Summary

In this dissertation, a research work on prediction of fluid field using simulation and sparse measurements is carried out. Two kinds of data-driven adaptive approaches are implemented combining with k-ω turbulence model; One is numerical gradient adaptive data-driven approach, another one is retrospective cost adaptive data-driven approach. The following work has been done,

- The derivation of RANS equation from the compressible governing equation and the incompressible governing equation is described. The process of getting the conservation equation of turbulent kinetic energy and specific dissipation rate is also given out.

- The compressible Reynolds-averaged Navier-Stokes equation and standard k-ω turbulence model has been discretized and solved in KATS solver.

- The incompressible Reynolds-averaged Navier-Stokes equation and pressure Poisson equation has been discretized and solved in KATS solver.

- Trivial but important parts of KATS solver are also detailed, which includes parallelization using MPI and domain decomposition.

- Code to code verification and experiments validation is carried out both for the compressible solver and incompressible solver. Pipe-flow case under compressible KATS solver is run and compared with fluent. A backward-facing step benchmark case is also run with compressible KATS solver. Another pipe-flow case under incompressible KATS solver is run and compared with measure-

ments. These prove that both the compressible solver and incompressible solver works correctly.

- D-DARK model which is based on numerical gradient adaptive RANS k-ω model has been applied, and code to code verification and experiment validation is carried out for pipe flow, a backward facing step flow and NACA 0012 airfoil.

- To give the governing equation more flexibility, the flow region can be divided into difference regions by some threshold, such as distance to the wall, velocity gradient. Every region has different parameter value. According to our test, non-dimensional velocity gradient is a nice variable to distinguish turbulent phenomena. A threshold value is found which could be more appropriate to divide the regions.

- An RCA data-driven k-ω model which could adjust its closure coefficients every time step. It can be applied to unsteady simulation. The retrospective cost adaptation (RCA), which was developed for real-time adaptive control technology but is used in this work for data-driven model adaptation. RCA has been successfully validated on numerous control applications that have significant transient behavior, which suggests that RCA is well suited for adaptation with the unsteady flow. The RCA-RANS k-ω model is verified with a statistically steady test case (pipe flow) as well as two unsteady test cases: vortex shedding from a surface-mounted cube and flow around a square cylinder.

6.2 Conclusions

Both the D-DARK model and RCA-RANS k-ω model are using an adaptive algorithm to improve the simulation result based on the sparsely measured result. They both can automatically adjust the closure coefficients of k-ω turbulent model.

125

The D-DARK model is validated with three canonical flow geometries: pipe flow, the backward-facing step, and flow around an airfoil. The adaptive model parameters are found to improve agreement with the measurement points about the simulation using non-adapted closure coefficients.

The RCA-RANS k-ω model is suitable for steady simulation as well as for simulating unsteady simulation. The model can automatically adjust the closure coefficients at every time step. The RCA-RANS k-ω model is verified on a statistically steady test case (pipe flow) as well as two unsteady test cases: vortex shedding from a surface-mounted cube and flow around a square cylinder. All cases demonstrate that the k-ω closure coefficients can be updated to match the measurement data.

The D-DARK model can only deal with the steady simulation, while RCA-RANS k-ω model can deal with both steady and unsteady simulation. D-DARK model needs longer time to response after numerical perturbation, while RCA-RANS k-ω model theoretically can adjust the parameter value every time step. Thus, RCA-RANS k-ω model should be faster than D-DARK model. However, the RCA-RANS k-ω model need to calculate the impulse response data at every measured point, which also cost extra time and calculations. Thus, both methods have their advantages and disadvantages.

Appendix A: Proof of Theorem 1

Proof. It follows from (4.12) and (A3) that

$$J(\boldsymbol{\theta}) = \sum_{i=1}^{N} \left(\boldsymbol{\Phi}_i \boldsymbol{\theta} + \boldsymbol{\psi}_i - \boldsymbol{\phi}_{\mathrm{m},i}\right)^{\mathrm{T}} \mathcal{W}_i \left(\boldsymbol{\Phi}_i \boldsymbol{\theta} + \boldsymbol{\psi}_i - \boldsymbol{\phi}_{\mathrm{m},i}\right), \tag{6.1}$$

which implies that

$$\frac{\partial J(\boldsymbol{\theta})}{\partial \boldsymbol{\theta}} = 2 \sum_{i=1}^{N} \left(\boldsymbol{\Phi}_i \boldsymbol{\theta} + \boldsymbol{\psi}_i - \boldsymbol{\phi}_{\mathrm{m},i}\right)^{\mathrm{T}} \mathcal{W}_i \boldsymbol{\Phi}_i. \tag{6.2}$$

Since $\boldsymbol{\theta}_*$ is a minimizer of J, it follows that

$$\left.\frac{\partial J(\boldsymbol{\theta})}{\partial \boldsymbol{\theta}}\right|_{\boldsymbol{\theta}=\boldsymbol{\theta}_*} = 2 \sum_{i=1}^{N} \left(\boldsymbol{\Phi}_i \boldsymbol{\theta}_* + \boldsymbol{\psi}_i - \boldsymbol{\phi}_{\mathrm{m},i}\right)^{\mathrm{T}} \mathcal{W}_i \boldsymbol{\Phi}_i = 0. \tag{6.3}$$

Next, define $\tilde{\boldsymbol{\theta}}_n \triangleq \boldsymbol{\theta}_n - \boldsymbol{\theta}_*$, and it follows from (6.1)–(6.3) that

$$J(\boldsymbol{\theta}_n) - J(\boldsymbol{\theta}_*) = \sum_{i=1}^{N} \left(\boldsymbol{\Phi}_i \tilde{\boldsymbol{\theta}}_n + \boldsymbol{\Phi}_i \boldsymbol{\theta}_* + \boldsymbol{\psi}_i - \boldsymbol{\phi}_{\mathrm{m},i}\right)^{\mathrm{T}} \mathcal{W}_i$$

$$\times \left(\boldsymbol{\Phi}_i \boldsymbol{\theta}_n + \boldsymbol{\psi}_i - \boldsymbol{\phi}_{\mathrm{m},i}\right)$$

$$- \sum_{i=1}^{N} \left(\boldsymbol{\Phi}_i \boldsymbol{\theta}_* + \boldsymbol{\psi}_i - \boldsymbol{\phi}_{\mathrm{m},i}\right)^{\mathrm{T}} \mathcal{W}_i$$

$$\times \left(\boldsymbol{\Phi}_i \boldsymbol{\theta}_* + \boldsymbol{\psi}_i - \boldsymbol{\phi}_{\mathrm{m},i}\right)$$

$$= \sum_{i=1}^{N} \tilde{\boldsymbol{\theta}}_n^{\mathrm{T}} \boldsymbol{\Phi}_i^{\mathrm{T}} \mathcal{W}_i \left(\boldsymbol{\Phi}_i \boldsymbol{\theta}_n + \boldsymbol{\psi}_i - \boldsymbol{\phi}_{\mathrm{m},i}\right)$$

$$+ \sum_{i=1}^{N} \left(\boldsymbol{\Phi}_i \boldsymbol{\theta}_* + \boldsymbol{\psi}_i - \boldsymbol{\phi}_{\mathrm{m},i}\right)^{\mathrm{T}} \mathcal{W}_i \boldsymbol{\Phi}_i \tilde{\boldsymbol{\theta}}_n$$

$$= \frac{1}{2} \left(\left.\frac{\partial J(\boldsymbol{\theta})}{\partial \boldsymbol{\theta}}\right|_{\boldsymbol{\theta}=\boldsymbol{\theta}_n} + \left.\frac{\partial J(\boldsymbol{\theta})}{\partial \boldsymbol{\theta}}\right|_{\boldsymbol{\theta}=\boldsymbol{\theta}_*}\right) \tilde{\boldsymbol{\theta}}_n$$

$$= \frac{1}{2} \left(\left.\frac{\partial J(\boldsymbol{\theta})}{\partial \boldsymbol{\theta}}\right|_{\boldsymbol{\theta}=\boldsymbol{\theta}_n}\right) \tilde{\boldsymbol{\theta}}_n,$$

which combined with (4.17) implies that

$$\xi_{\mathrm{opt},n} = \frac{\left(\partial J(\boldsymbol{\theta})/\partial \boldsymbol{\theta}|_{\boldsymbol{\theta}=\boldsymbol{\theta}_n}\right) \tilde{\boldsymbol{\theta}}_n}{\|\boldsymbol{\Gamma}(\boldsymbol{\theta}_n)\|^2}. \tag{6.4}$$

Therefore, assumption (A2) implies that

$$\xi_{\text{opt},n} = \frac{\tilde{\boldsymbol{\theta}}_n^{\text{T}} \boldsymbol{\Gamma}(\boldsymbol{\theta}_n)}{\|\boldsymbol{\Gamma}(\boldsymbol{\theta}_n)\|^2}. \tag{6.5}$$

Next, it follows from (4.16) and (4.17) that

$$\mathcal{J}_n(\xi_n) = -2\xi_n \tilde{\boldsymbol{\theta}}_n^{\text{T}} \boldsymbol{\Gamma}(\boldsymbol{\theta}_n) + \xi_n^2 \|\boldsymbol{\Gamma}(\boldsymbol{\theta}_n)\|^2. \tag{6.6}$$

Since (A1) implies that $\boldsymbol{\Gamma}(\boldsymbol{\theta}_n) \neq 0$, it follows from (6.6) that $\mathcal{J}_n(\xi_n) < 0$ if and only if

$$0 < \xi_n < \frac{2\tilde{\boldsymbol{\theta}}_n^{\text{T}} \boldsymbol{\Gamma}(\boldsymbol{\theta}_n)}{\|\boldsymbol{\Gamma}(\boldsymbol{\theta}_n)\|^2} = 2\xi_{\text{opt},n}, \tag{6.7}$$

which confirms the first statement of the theorem.

To show the last statement of the theorem, note that (6.6) is quadratic in ξ_n. Since, in addition, $\boldsymbol{\Gamma}(\boldsymbol{\theta}_n) \neq 0$, it follows that $\mathcal{J}_n(\xi_n)$ is minimized by ξ_n such that $\mathrm{d}\,\mathcal{J}_n(\xi)/\,\mathrm{d}\xi|_{\xi=\xi_n} = 0$. Thus, (6.5) implies that $\mathcal{J}_n(\xi_n)$ is minimized by $\xi_n = \xi_{\text{opt},n}$. $\quad\square$

Bibliography

[1]   M. Hultmark, S. C. C. Bailey, A. J. Smits, Scaling of near-wall turbulence in pipe flow, Journal of Fluid Mechanics 649 (2010) 103–113. `doi:10.1017/S0022112009994071`.

[2]   D. M. Driver, H. L. Seegmiller, Features of a reattaching turbulent shear layer in divergent channel flow, AIAA Journal 23 (2) (1985) 163–171. `doi:10.2514/3.8890`.

[3]   S.-W. Kim, Calculation of reattaching shear layers in divergent channel with a multiple-time-scale turbulence model, in: 28th Aerospace Sciences Meeting, AIAA Paper 90-0047, Reno, NV, 1990. `doi:10.2514/6.1990-47`.

[4]   N. Gregory, C. L. O'reilly, Low-speed aerodynamic characteristics of NACA 0012 aerofoil section, including the effects of upper-surface roughness simulating hoar frost, Reports and Memoranda 3726, Aeronautical Research Council (January 1970).
        URL `http://naca.central.cranfield.ac.uk/reports/arc/rm/3726.pdf`

[5]   D. Lakehal, W. Rodi, Calculation of the flow past a surface-mounted cube with two-layer turbulence models, Journal of Wind Engineering and Industrial Aerodynamics 67 (1997) 65–78. `doi:10.1016/S0167-6105(97)00063-9`.

[6]   H. Grant, R. Stewart, A. Moilliet, Turbulence spectra from a tidal channel, Journal of Fluid Mechanics 12 (02) (1962) 241–268.

[7]   F. Payne, J. Lumley, One dimensional spectra derived from an airborne hot-wire anemometer, Quarterly Journal of the Royal Meteorological Society 92 (393) (1966) 397–401.

[8]   C. M. Sheih, H. Tennekes, J. Lumley, Airborne hot wire measurements of the small scale structure of atmospheric turbulence, Physics of Fluids 14 (2) (1971) 201–215. `doi:10.1063/1.1693416`.

[9]   S. Thorpe, T. Osborn, J. Jackson, A. Hall, R. Lueck, Measurements of turbulence in the upper ocean mixing layer using autosub, Journal of Physical Oceanography 33 (1) (2003) 122–145.

[10]   D. C. Wilcox, A complete model of turbulence revisited, in: 22nd Aerospace Sciences Meeting, AIAA Paper 84-0176, Reno, NV, 1984. `doi:10.2514/6.1984-176`.

[11]   J. McDonough, Introductory lectures on turbulence physics, mathematics and modeling.

[12] P. Sagaut, S. Deck, M. Terracol, Multiscale and multiresolution approaches in turbulence: LES, DES and hybrid RANS/LES methods: applications and guidelines, World Scientific, 2013.

[13] C. Winkler, S. L. Rani, Relative importance of the lift force on heavy particles due to turbulence driven secondary flows, Powder Technology 190 (3) (2009) 310–318.

[14] S.-E. Kim, Large eddy simulation using unstructured meshes and dynamic subgrid-scale turbulence models, in: 34th AIAA Fluid Dynamics Conference and Exhibit, AIAA Paper 2004-2548, Portland, OR, 2004. `doi:10.2514/6.2004-2548`.

[15] C. Pantano, D. I. Pullin, P. E. Dimotakis, G. Matheou, LES approach for high reynolds number wall-bounded flows with application to turbulent channel flow, Journal of Computational Physics 227 (21) (2008) 9271–9291.

[16] M. Germano, U. Piomelli, P. Moin, W. H. Cabot, A dynamic subgrid scale eddy viscosity model, Physics of Fluids 3 (7) (1991) 1760–1765. `doi:10.1063/1.857955`.

[17] C. Meneveau, P. Sagaut, Large eddy simulation for incompressible flows: an introduction, Springer Science and Business Media, 2006.

[18] J. Bardino, J. H. Ferziger, W. C. Reynolds, Improved turbulence models based on large eddy simulation of homogeneous, incompressible turbulent flows, Stanford Univ. Report 1.

[19] J. W. Deardorff, Numerical investigation of neutral and unstable planetary boundary layers, Journal of the Atmospheric Sciences 29 (1) (1972) 91–115.

[20] A. Vreman, An eddy-viscosity subgrid-scale model for turbulent shear flow: Algebraic theory and applications, Physics of Fluids 16 (10) (2004) 3670–3681. `doi:10.1063/1.1785131`.

[21] J. Smagorinsky, General circulation experiments with the primitive equations: I. the basic experiment*, Monthly Weather Review 91 (3) (1963) 99–164.

[22] J. W. Deardorff, A numerical study of three-dimensional turbulent channel flow at large reynolds numbers, Journal of Fluid Mechanics 41 (02) (1970) 453–480.

[23] W. Deconinck, Design and application of discrete explicit filters for large eddy simulation of compressible turbulent flows, Ph.D. thesis (2008).

[24] J. A. Domaradzki, E. M. Saiki, A subgrid-scale model based on the estimation of unresolved scales of turbulence, Physics of Fluids (1994-present) 9 (7) (1997) 2148–2164.

[25] S. Basu, F. Porté-Agel, Large-eddy simulation of stably stratified atmospheric boundary layer turbulence: a scale-dependent dynamic modeling approach, Journal of the Atmospheric Sciences 63 (2005) 2074–2091.

[26] M. Germano, Turbulence: the filtering approach, Journal of Fluid Mechanics 238 (1992) 325–336.

[27] W. Thurston, K. J. Tory, R. J. Fawcett, J. D. Kepert, Large-eddy simulations of bushfire plumes in the turbulent atmospheric boundary layer, in: J. Piantadosi, R. Anderssen, B. J. (Eds.), 20th International Congress on Modelling and Simulation, 2013.

[28] J. Bardina, J. H. Ferziger, W. C. Reynolds, Improved turbulence models based on large eddy simulation of homogeneous, incompressible, turbulent flows, AIAA Paper 80-1357 (1983).

[29] S. Liu, C. Meneveau, J. Katz, On the properties of similarity subgrid-scale models as deduced from measurements in a turbulent jet, Journal of Fluid Mechanics 275 (1994) 83–119.

[30] U. Piomelli, J. H. Ferziger, P. Moin, Model consistency in large eddy simulation of turbulent channel flows, Physics of Fluids 31 (7) (1988) 1884.

[31] C. Fureby, F. F. Grinstein, Large eddy simulation of high-reynolds-number free and wall-bounded flows, Journal of Computational Physics 181 (1) (2002) 68–97.

[32] S. Stolz, N. A. Adams, An approximate deconvolution procedure for large-eddy simulation, Physics of Fluids (1994-present) 11 (7) (1999) 1699–1701.

[33] P. Sagaut, Large Eddy Simulation for Incompressible Flows, Springer, 2002.

[34] J. A. Domaradzki, N. A. Adams, Direct modelling of subgrid scales of turbulence in large eddy simulations, Journal of Turbulence 3 (024) (2002) 1.

[35] A. R. Kerstein, Linear-eddy modelling of turbulent transport. part 3. mixing and differential molecular diffusion in round jets, Journal of Fluid Mechanics 216 (1990) 411–435.

[36] T. Echekki, A. R. Kerstein, T. D. Dreeben, J.-Y. Chen, 'One-dimensional turbulence' simulation of turbulent jet diffusion flames: model formulation and illustrative applications, Combustion and Flame 125 (3) (2001) 1083–1105.

[37] J. M. McDonough, Y. Yang, E. C. Hylin, Modeling time-dependent turbulent flow over a backward-facing step via additive turbulent decomposition and chaotic algebraic maps, in: Proc. First Asian Computational Fluid Dynamics Conference, Hong Kong, 1995, pp. 747–752.

[38] E. C. Hylin, A stochastic model for small-scale turbulence, Ph.D. thesis, University of Kentucky (1997).

[39] S. Bible, J. McDonough, T. Yang, A priori testing of a synthetic velocity subgrid-scale velocity model for large-eddy simulation, in: 55th Annual Meeting of the APS Division of Fluid Dynamics, Vol. 47, Bulletin of the American Physical Society, 2002, abstract ID: BAPS.2012.DFD.AK.005.

[40] T. Tang, Z. Li, J. McDonough, P. Hislop, Numerical investigation of the "poor man's navier–stokes equations" with darcy and forchheimer terms, International Journal of Bifurcation and Chaos 26 (05) (2016) 1650086.

[41] T. Tang, J. McDonough, A theoretical model for the porosity–permeability relationship, International Journal of Heat and Mass Transfer 103 (2016) 984–996.

[42] W. Zeng, R. Fu, J. McDonough, Low-order discrete dynamical system for h2-air finite-rate chemistry in 3d, International Conference on Heat Transfer, Fluid Mechanics and Thermodynamics, 2014.

[43] W. Zeng, J. M. McDonough, Low-order discrete dynamical system for jet diffusion flame.

[44] O. Reynolds, On the dynamical theory of incompressible viscous fluids and the determination of the criterion, Philosophical Transactions of the Royal Society of London A: Mathematical, Physical and Engineering Sciences 186 (1895) 123–164. `doi:10.1098/rsta.1895.0004`.

[45] L. Prandtl, Bericht über untersuchungen zur ausgebildeten turbulenz. z. ang. math. mech. 5 (1925) 136–139. nachdruck: Ges. abh. s. 714–718 (1961).

[46] J. V. Boussinesq, Essai sur la théorie des eaux courantes, Vol. XXII, Imprimerie nationale, 1877.
URL `http://catalogue.bnf.fr/ark:/12148/cb301489808`

[47] D. C. Wilcox, Turbulence modeling for CFD, 2nd Edition, DCW industries Inc., La Canada, CA, 1998.

[48] T. B. Gatski, J.-P. Bonnet, Compressibility, turbulence and high speed flow, Academic Press, 2013.

[49] F. G. Schmitt, About Boussinesq's turbulent viscosity hypothesis: historical remarks and a direct evaluation of its validity, Comptes Rendus Mécanique 335 (9) (2007) 617–627.

[50] J. Kim, P. Moin, R. Moser, Turbulence statistics in fully developed channel flow at low reynolds number, Journal of Fluid Mechanics 177 (1987) 133–166.

[51] D. C. Wilcox, Turbulence modeling for CFD, Vol. 2, DCW industries La Canada, CA, 1998.

[52] A. N. Kolmogorov, Equations of turbulent motion in an incompressible fluid, in: Doklady Akademii Nauk SSSR, Vol. 30, 1941, pp. 299–303.

[53] M. J. Berger, P. Colella, Local adaptive mesh refinement for shock hydrodynamics, J. Comput. Phys. 82 (1) (1989) 64–84. `doi:10.1016/0021-9991(89)90035-1`.

[54] K. J. Fidkowski, D. L. Darmofal, Review of output-based error estimation and mesh adaptation in computational fluid dynamics, AIAA Journal 49 (4) (2011) 673–694. `doi:10.2514/1.J050073`.

[55] J. Larsson, F. Lien, E. Yee, Feedback-controlled forcing in hybrid LES/RANS, International Journal of Computational Fluid Dynamics 20 (10) (2006) 687–699.

[56] T. Knopp, T. Alrutz, D. Schwamborn, A grid and flow adaptive wall-function method for RANS turbulence modelling, Journal of Computational Physics 220 (1) (2006) 19–40.

[57] C. Florian Menter, C. Martin Kuntz, C. Roland Bender, A scale-adaptive simulation model for turbulent flow predictions, AIAA paper.

[58] F. Menter, Y. Egorov, The scale-adaptive simulation method for unsteady turbulent flow predictions. Part 1: Theory and model description, Flow, Turbulence and Combustion 85 (1) (2010) 113–138. `doi:10.1007/s10494-010-9264-5`.

[59] F. Menter, Y. Egorov, A scale-adaptive simulation model using two-equation models, AIAA paper 1095 (2005) 2005.

[60] Y. Egorov, F. Menter, R. Lechner, D. Cokljat, The scale-adaptive simulation method for unsteady turbulent flow predictions. Part 2: application to complex flows, Flow, Turbulence and Combustion 85 (1) (2010) 139–165.

[61] F. Magagnato, M. Gabi, A new adaptive turbulence model for unsteady flow fields in rotating machinery, International Journal of Rotating Machinery 8 (3) (2002) 175–183. `doi:10.1155/S1023621X02000167`.

[62] G. Medic, G. Kalitzin, G. Iaccarino, E. van der Weide, Adaptive wall functions with applications, AIAA paper 3744 (2006) 2005.

[63] J. Wackers, K. Ait Said, G. Deng, P. Queutey, M. Visonneau, I. Mizine, Adaptive grid refinement applied to RANS ship flow computation, in: 28th Symposium on Naval Hydrodynamics,, Pasadena, CA, 2010.
URL `http://www.numeca.com/en/resources/case-studies/adaptive-grid-refinement-applied-rans-ship-flow-computation`

[64] R. Hartmann, J. Held, T. Leicht, Adjoint-based error estimation and adaptive mesh refinement for the rans and $k - \omega$ turbulence model equations, Journal of Computational Physics 230 (11) (2011) 4268–4284.

[65] C. M. Winkler, A. J. Dorgan, M. Mani, Scale adaptive simulations of turbulent flows on unstructured grids, in: 29th AIAA Applied Aerodynamics Conference, pp. 27–30.

[66] O. Temel, J. van Beeck, Two-equation eddy viscosity models based on the monin–obukhov similarity theory, Applied Mathematical Modelling 42 (2017) 1–16.

[67] O. Temel, J. van Beeck, Adaptation of mesoscale turbulence parameterisation schemes as rans closures for abl simulations, Journal of Turbulence 17 (10) (2016) 966–997.

[68] E. Gauthier, T. Kinsey, G. Dumas, Rans versus scale-adaptive turbulence modeling for engineering prediction of oscillating-foils turbines, 21th Annual Conference of the CFD Society of Canada.

[69] J. Lundvall, V. Kozlov, P. Weinerfelt, Iterative methods for data assimilation for burgers' equation, Journal of Inverse and Ill-posed Problems 14 (5) (2006) 505–535. `doi:10.1515/156939406778247589`.

[70] O. Pironneau, Discontinuous data assimilation, Proceedings of the indian National Science Academy 69 (5A) (2003) 473–478.
URL `http://insa.nic.in/writereaddata/UpLoadedFiles/PINSA/Vol69A_2003_5_Art02.pdf`

[71] T. Tachim Medjo, L. R. Tcheugoue Tebou, Adjoint-based iterative method for robust control problems in fluid mechanics, SIAM Journal on Numerical Analysis 42 (1) (2004) 302–325. `doi:10.1137/S0036142902416231`.

[72] L. Ladický, S. Jeong, B. Solenthaler, M. Pollefeys, M. Gross, Data-driven fluid simulations using regression forests, ACM Trans. Graph. 34 (6) (2015) 199:1–199:9. `doi:10.1145/2816795.2818129`.

[73] M. Ghil, P. Malanotte-Rizzoli, Data assimilation in meteorology and oceanography, Advances in Geophysics 33 (1990) 141–266. `doi:10.1016/S0065-2687(08)60442-2`.

[74] V. Pérez-Muññuzuri, I. Gelpi, Application of nonlinear forecasting techniques for meteorological modeling, Annales Geophysicae 18 (10) (2000) 1349–1359. `doi:10.1007/s00585-000-1349-3`.

[75] Y. Lee, A. J. Majda, Multiscale methods for data assimilation in turbulent systems, Multiscale Modeling & Simulation 13 (2) (2015) 691–713. `doi:10.1137/140978326`.

[76] E. J. Nielsen, B. Diskin, Discrete adjoint-based design for unsteady turbulent flows on dynamic overset unstructured grids, AIAA journal 51 (6) (2013) 1355–1373.

[77] M. Nemec, M. J. Aftosmis, Adjoint sensitivity computations for an embedded-boundary cartesian mesh method, Journal of Computational Physics 227 (4) (2008) 2724–2742.

[78] A. Jameson, Aerodynamic design via control theory, Journal of scientific computing 3 (3) (1988) 233–260.

[79] M. Giles, N. Pierce, M. Giles, Adjoint equations in cfd-duality, boundary conditions and solution behaviour, in: 13th Computational Fluid Dynamics Conference, p. 1850.

[80] A. C. Marta, S. Shankaran, On the handling of turbulence equations in rans adjoint solvers, Computers & Fluids 74 (2013) 102–113.

[81] J. R. Martins, P. Sturdza, J. J. Alonso, The complex-step derivative approximation, ACM Transactions on Mathematical Software (TOMS) 29 (3) (2003) 245–262.

[82] Z. Lyu, G. K. Kenway, C. Paige, J. Martins, Automatic differentiation adjoint of the reynolds-averaged navier–stokes equations with a turbulence model, in: 21st AIAA Computational Fluid Dynamics Conference, San Diego, CA.

[83] R. E. Perez, J. Martins, pyacdt: An object-oriented framework for aircraft design modelling and multidisciplinary optimization, in: Proceedings of the 12th AIAA/ISSMO Multidisciplinary Analysis and Optimization Conference, Victoria, BC.

[84] C. A. Mader, J. RA Martins, J. J. Alonso, E. V. Der Weide, Adjoint: An approach for the rapid development of discrete adjoint solvers, AIAA journal 46 (4) (2008) 863–873.

[85] K. Duraisamy, P. A. Durbin, Transition modeling using data driven approaches, in: Center for Turbulence Research: Proceedings of the Summer Program, 2014, p. 427.
URL https://web.stanford.edu/group/ctr/Summer/SP14/09_Large-eddy_simulation/07_duraisamy.pdf

[86] Z. J. Zhang, K. Duraisamy, Machine learning methods for data-driven turbulence modeling, in: 22nd AIAA Computational Fluid Dynamics Conference, AIAA Paper 2015-2460, Dallas, TX, 2015. doi:10.2514/6.2015-2460.

[87] K. Duraisamy, Z. J. Zhang, A. P. Singh, New approaches in turbulence and transition modeling using data-driven techniques, in: 53rd AIAA Aerospace

Sciences Meeting, AIAA Paper 2015-1284, Kissimmee, FL, 2015. `doi:10.2514/6.2015-1284`.

[88] D. P. G. Foures, N. Dovetta, D. Sipp, P. J. Schmid, A data-assimilation method for reynolds-averaged navier–stokes-driven mean flow reconstruction, Journal of Fluid Mechanics 759 (2014) 404–431. `doi:10.1017/jfm.2014.566`.

[89] G. Iungo, F. Viola, U. Ciri, M. Rotea, S. Leonardi, Data-driven rans for simulations of large wind farms, Journal of Physics: Conference Series 625 (1) (2015) 012025. `doi:10.1088/1742-6596/625/1/012025`.

[90] H. Zhang, H. Weng, A. Martin, Simulation of flow-tube oxidation on the carbon preform of PICA, in: 52nd Aerospace Sciences Meeting, AIAA Paper 2014-1209, National Harbor, MD, 2014. `doi:10.2514/6.2014-1209`.

[91] R. S. C. Davuluri, H. Zhang, A. Martin, Numerical study of spallation phenomenon in an arc-jet environment, Journal of Thermophysics and Heat Transfer 30 (1). `doi:10.2514/1.T4586`.

[92] H. Weng, A. Martin, Numerical investigation of thermal response using orthotropic charring ablative material, Journal of Thermophysics and Heat Transfer 29 (3) (2015) 429–438. `doi:10.2514/1.T4576`.

[93] H. Weng, S. C. C. Bailey, A. Martin, Numerical study of iso-q sample geometric effects on charring ablative materials, International Journal of Heat and Mass Transfer 80 (2015) 570–596. `doi:10.1016/j.ijheatmasstransfer.2014.09.040`.

[94] H. Weng, A. Martin, Multidimensional modeling of pyrolysis gas transport inside charring ablative materials, Journal of Thermophysics and Heat Transfer 28 (4) (2014) 583–597. `doi:10.2514/1.T4434`.

[95] G. Karypis, V. Kumar, METIS: A Software Package for Partitioning Unstructured Graphs, Partitioning Meshes, and Computing Fill-Reducing Orderings of Sparse Matrices, Univeristy of Minnesota, Minneapolis, MN (1998).

[96] E. Gabriel, G. E. Fagg, G. Bosilca, T. Angskun, J. J. Dongarra, J. M. Squyres, V. Sahay, P. Kambadur, B. Barrett, A. Lumsdaine, R. H. Castain, D. J. Daniel, R. L. Graham, T. S. Woodall, Open MPI: Goals, concept, and design of a next generation MPI implementation, in: Proceedings, 11th European PVM/MPI Users' Group Meeting, Budapest, Hungary, 2004, pp. 97–104. `doi:10.1007/978-3-540-30218-6_19`.

[97] S. Balay, W. D. Gropp, L. C. McInnes, B. F. Smith, Efficient management of parallelism in object oriented numerical software libraries, in: E. Arge, A. M. Bruaset, H. P. Langtangen (Eds.), Modern Software Tools in Scientific Computing, Vol. 1, Birkhäuser Press, 1997, pp. 163–202. `doi:10.1007/978-1-4612-1986-6_8`.

[98]   S. Balay, J. Brown, K. Buschelman, V. Eijkhout, W. D. Gropp, D. Kaushik, M. G. Knepley, L. C. McInnes, B. F. Smith, H. Zhang, PETSc users manual, Tech. Rep. ANL-95/11 - Revision 3.3, Argonne National Laboratory (2012). URL `http://www.mcs.anl.gov/petsc/petsc-current/docs/manual.pdf`

[99]   S. Balay, S. Abhyankar, M. F. Adams, J. Brown, P. Brune, K. Buschelman, V. Eijkhout, W. D. Gropp, D. Kaushik, M. G. Knepley, L. C. McInnes, K. Rupp, B. F. Smith, H. Zhang, PETSc Web page, http://www.mcs.anl.gov/petsc (2014). URL `http://www.mcs.anl.gov/petsc`

[100] M.-S. Liou, A sequel to ausm, part ii: Ausm+-up for all speeds, Journal of Computational Physics 214 (1) (2006) 137–170.

[101] J. Guermond, P. Minev, J. Shen, An overview of projection methods for incompressible flows, Computer methods in applied mechanics and engineering 195 (44) (2006) 6011–6045.

[102] J. McDonough, T. Yang, M. Sheetz, Parallelization of a modern cfd incompressible turbulent flow code, in: at Parallel CFD, pp. 13–15.

[103] J. Leray, Etude de diverses équations intégrales non linéaires et de quelques problèmes que pose l'hydrodynamique, Thèses françaises de l'entre-deux-guerres 142 (1933) 1–82.

[104] G. Wei, Y.-l. Duan, R.-x. Liu, The finite volume projection method with hybrid unstructured triangular collocated grids for incompressible flows, Journal of Hydrodynamics, Ser. B 21 (2) (2009) 201–211.

[105] P. M. Gresho, S. T. Chan, On the theory of semi-implicit projection methods for viscous incompressible flow and its implementation via a finite element method that also introduces a nearly consistent mass matrix. Part 2: Implementation, International journal for numerical methods in fluids 11 (5) (1990) 621–659. `doi:10.1002/fld.1650110510`.

[106] J. B. Bell, P. Colella, H. M. Glaz, A second-order projection method for the incompressible navier-stokes equations, Journal of Computational Physics 85 (2) (1989) 257–283.

[107] A. J. Chorin, On the convergence of discrete approximations to the navier-stokes equations, Mathematics of computation 23 (106) (1969) 341–353.

[108] Ş.-M. SIMIONESCU, Ü. DÜZEL, C. ESPOSITO, Z. ILICH, D. BROBOANĂ, Particle image velocimetry measurements on a turbulent air jet over a flat plate.

[109] F. Hamba, Exact transport equation for local eddy viscosity in turbulent shear flow, Physics of Fluids 25 (8) (2013) 085102. `doi:10.1063/1.4816702`.

[110] NASA, Nasa langley research center turbulence modeling resource (2017). URL https://turbmodels.larc.nasa.gov/

[111] Z. Li, H. Zhang, S. C. Bailey, J. B. Hoagg, A. Martin, A data-driven RANS k-ω approach for modeling turbulent flows, Journal of Computational Physics In press (Control ID JCOMP-S-17-00137). doi:10.1016/j.jcp.2017.05.009.

[112] F. Menter, Y. Egorov, A scale-adaptive simulation model using two-equation models, in: 43rd AIAA Aerospace Sciences Meeting and Exhibit, AIAA Paper 2005-1095, Reno, NV, 2005. doi:10.2514/6.2005-1095.

[113] Y. Ederov, F. Menter, DESider – A European Effort on Hybrid RANS–LES Modelling, Springer-Verlag Berlin Heidelberg, 2009, Ch. Formulation of the scale-adaptive simulation (SAS) model during the DESider project., pp. 51–62. doi:10.1007/978-3-540-92773-0.

[114] C. M. Winkler, A. J. Dorgan, M. Mani, Scale adaptive simulations of turbulent flows on unstructured grids, in: 20th AIAA Computational Fluid Dynamics Conference, AIAA Paper 2011-3559, 2011. doi:10.2514/6.2011-3559.

[115] T. Knopp, T. Alrutz, D. Schwamborn, A grid and flow adaptive wall-function method for RANS turbulence modelling, Journal of Computational Physics 220 (1) (2006) 19–40. doi:10.1016/j.jcp.2006.05.003.

[116] G. Kalitzin, G. Medic, G. Iaccarino, P. Durbin, Near-wall behavior of rans turbulence models and implications for wall functions, Journal of Computational Physics 204 (1) (2005) 265–291. doi:10.1016/j.jcp.2004.10.018.

[117] G. Kalitzin, G. Medic, Adaptive wall functions for the v^2–f turbulence model, International Journal for Numerical Methods in Fluids 53 (4) (2007) 651–667. doi:10.1002/fld.1302.

[118] A. P. Singh, K. Duraisamy, Using field inversion to quantify functional errors in turbulence closures, Physics of Fluids 28 (4) (2016) 045110. doi:10.1063/1.4947045.

[119] D. C. Wilcox, Reassessment of the scale-determining equation for advanced turbulence models, AIAA Journal 26 (11) (1988) 1299–1310. doi:10.2514/3.10041.

[120] A. Ferrante, S. Elghobashi, On the physical mechanisms of two-way coupling in particle-laden isotropic turbulence, Physics of Fluids 15 (2) (2003) 315–329. doi:10.1063/1.1532731.

[121] P. Burattini, P. Lavoie, A. Agrawal, L. Djenidi, R. Antonia, Power law of decaying homogeneous isotropic turbulence at low reynolds number, Physical Review E 73 (6) (2006) 066304. doi:10.1103/PhysRevE.73.066304.

[122] S. B. Pope, Turbulent flows, Cambridge University Press, Cambridge, UK, 2000.

[123] S. C. C. Bailey, M. Vallikivi, M. Hultmark, A. J. Smits, Estimating the value of von Kármán's constant in turbulent pipe flow, Journal of Fluid Mechanics 749 (2014) 79–98. `doi:10.1017/jfm.2014.208`.

[124] A. A. Townsend, The structure of turbulent shear flow, 2nd Edition, Cambridge Monographs on Mechanics, Cambridge University Press, Cambridge, 1980.

[125] C. L. Rumsey, Recent developments on the turbulence modeling resource website, in: 22nd AIAA Computational Fluid Dynamics Conference, AIAA Paper 2015-2927, Dallas, TX, 2015. `doi:10.2514/6.2015-2927`.

[126] A. Viladegut, Ü. Düzel, O. Chazot, Diffusion effects on the determination of surface catalysis in inductively coupled plasma facility, Chemical Physics 485 (2017) 88–97.

[127] G. Medic, G. Kalitzin, G. Iaccarino, E. van der Weide, Adaptive wall functions with applications, Tech. rep., Stanford University (2006).
URL `http://aero-comlab.stanford.edu/vdweide/aiaa_submitted_revised.pdf`

[128] J. B. Hoagg, M. A. Santillo, D. S. Bernstein, Discrete-time adaptive command following and disturbance rejection with unknown exogenous dynamics, Automatic Control, IEEE Transactions on 53 (4) (2008) 912–928. `doi:10.1109/TAC.2008.920234`.

[129] J. B. Hoagg, D. S. Bernstein, Retrospective cost model reference adaptive control for nonminimum-phase systems, J. Guid. Contr. Dyn. 35 (6) (2012) 1767–1786.

[130] Y. Rahman, A. Xie, J. B. Hoagg, D. S. Bernstein, A tutorial and overview of retrospective cost adaptive control, in: Proc. Amer. Contr. Conf., Boston, MA, 2016, pp. 3386—-3409.

[131] J. B. Hoagg, D. S. Bernstein, Cumulative retrospective cost adaptive control with RLS-based optimization, in: Proc. Amer. Contr. Conf., Baltimore, MD, 2010, pp. 4016–4021.

[132] B. Coffer, J. B. Hoagg, D. S. Bernstein, Cumulative retrospective cost adaptive control of systems with amplitude and rate saturation, in: Proc. Amer. Contr. Conf., San Francisco, CA, 2011, pp. 2344–2349.

[133] P. Ioannou, B. Fidan, Adaptive Control Tutorial, SIAM, 2006.

[134] R. J. Martinuzzi, S. C. C. Bailey, G. A. Kopp, Influence of wall proximity on vortex shedding from a square cylinder, Experiments in Fluids 34 (5) (2003) 585–596. `doi:10.1007/s00348-003-0594-0`.

[135] S. C. C. Bailey, R. J. Martinuzzi, G. Kopp, The effects of wall proximity on vortex shedding from a square cylinder: three-dimensional effects, Physics of Fluids 14 (12) (2002) 4160–4177. `doi:10.1063/1.1514972`.

Vita

NAME: Li, Zhiyong

EDUCATION:

University of Kentucky, U.S., Mechanical Engineering, Ph.D., 9/2012 – 5/2017
Central South University, China, Energy and Power Engineering, M.S., 9/2009-6/2012
Central South University, China, Energy and Power Engineering, B.S., 9/2005-6/2009

RESEARCH AREA:

Computational flow solver developing (compressible and incompressible), data-driven turbulence prediction with RANS k−ω method, Real-time data-driven turbulence prediction with Retrospective Cost Adaptive Control (RCAC) method

RESEARCH EXPERIENCE:

1. **Unstructured finite volume incompressible flow solver with RCAC data-driven turbulence model.** (7/2015-5/2017)

➢ Using projection method, unstructured finite volume 3D incompressible implicit flow solver is built.

➢ Using second order upwind scheme, domain decomposition and MPI parallelization.

➢ RANS turbulence model (k−ω, SST), LES turbulence model (high-pass Smagorinsky, Vreman, Deardorff).

➢ Based on this platform, a data-driven unsteady turbulence model with RCAC method is developed.

2. **Unstructured finite volume compressible flow solver Research.** (10/2013-6/2015)

➢ Based on fully understand the compressible implicit flow solver of current lab, RANS turbulence model (k−ω, SST, Baldwin-Lomax), LES turbulence model (high pass Smagorinsky, Vreman, Deardorff) is built.

➢ A new data-driven method is added with k−ω turbulence model to get more accurate simulation results.

3. **Numerical simulation of flapping wing model** (9/2012-8/2013)

   Immersed boundary method, overset mesh treatment, moving mesh, coupling of solid and fluid

4. **Vortex mass flowmeter design**. (5/2011-5/2012)

   Base on the pressure difference of bluff-body wake, a vortex mass flowmeter is designed from software to hardware.

5. **Pattern recognition of inhomogeneous bluff-body wake flow in pipeline,** funded by Natural Science Foundation of China. (8/2010-5/2011)

6. **Physical property tester for Metal Phase Changing**, funded by National University Student Innovation Project. (10/2007-12/2008)

PUBLICATIONS:

1. Zhiyong Li, Sean Bailey, Jesse Hoagg, Alexandre Martin, "Retrospective Cost Adaptive Control RANS turbulence prediction method". (submitted)

2. Z. Li, H. Zhang, J. Hoagg, S. C. Bailey, and A. Martin, ``A data-driven adaptive Reynolds-averaged Navier-Stokes k− ω model for turbulent flow,'' Journal of Computational Physics In press (Control ID JCOMP-S-17-00137). DOI:10.1016/j.jcp.2017.05.009.

3. Li, Zhiyong and Zhang, Huaibao and Hoagg, Jesse B and Bailey, Sean CC and Martin, Alexandre, "Turbulence Simulation Using a Numerical Gradient Adaptive k− ω Model", 54th AIAA Aerospace Sciences Meeting, SciTech2016 San Diego, 2016. DOI:10.2514/6.2016-0587

4. Tingting Tang, Zhiyong Li, J. M. McDonough, Peter Hislop, "Numerical investigation of the `poor man's Navier--Stokes equations' with Darcy and Forchheimer terms," International Journal of Bifurcation and Chaos, vol. 26, No.5, 2016. DOI:10.1142/S0218127416500863

5. Zhiyong Li, Zhiqiang Sun, "Development of the vortex mass flowmeter with wall pressure measurement". Measurement Science Review, vol. 13:20-24, 2013. DOI:10.2478/msr-2013-0002

6. Zhiqiang Sun, Zhiyong Li, Yun Jiang, Hongliang Zhou, "Influence of bluff body shape on wall pressure distribution in vortex flowmeter". J. Central South University, vol. 20:724-729, 2013. DOI:10.1007/s11771-013-1540-9

7. Zhiqiang Sun, Zhiyong LI, "A New Method for Linear Compression and Decompression of Sequential Sensor Signals". Sensors & Transducers (1726-5479), 2012, vol. 143: 8

8. Zhiqiang Sun, Zhiyong Li, Jianwu Zheng. "Influence of improper installation on the measurement performance of Pitot tubes". Proceedings of 2009 International Conference on Industrial Mechatronics and Automation, May 15-16, Chengdu, China, vol. 1: 53-56, 2009. DOI:10.1109/ICIMA.2009.5156558

CONFERENCE PRESENTATION

1. Li, Zhiyong and Zhang, Huaibao and Hoagg, Jesse B and Bailey, Sean CC and Martin, Alexandre. "Turbulent Flow Field Prediction Using Numerical Gradient Data-driven Adaptive k − ω Model". AIAA 41th Dayton-Cincinnati Aerospace Sciences Symposium, Dayton, Ohio, USA, 2016.

2. Li, Zhiyong and Zhang, Huaibao and Hoagg, Jesse B and Bailey, Sean CC and Martin, Alexandre. "Turbulence Simulation Using a Numerical Gradient Adaptive k-ω Model". 54th AIAA Aerospace Sciences Meeting SciTech2016, San Diego, California, USA, 2016.

3. Li, Zhiyong and McDonough, James M., "Numerical simulation of flapping wing models and exploration of near wall effects". AIAA 38th Dayton-Cincinnati Aerospace Sciences Symposium, Dayton, Ohio, USA, 2013.

AWARDS:

Outstanding master's dissertation of Hunan, 2014;

Chen Xinmin Excellent postgraduate scholarship, 2011;

Excellent Graduates of CSU, 2009;

Third Prize for the 1st National(China) University Student Social Practice and Science contest on Energy-saving and Emission-reduction, 2009.